Energy dissipation and failure in articular cartilage

By

Guebum Han

A dissertation submitted in partial fulfillment of

the requirements for the degree of

Doctor of Philosophy

(Mechanical Engineering)

at the

UNIVERSITY OF WISCONSIN - MADISON

2019

Date of final oral examination: August 7, 2019

The dissertation is approved by the following members of the Final Oral Committee:

Melih Eriten, Associate Professor, Mechanical Engineering
Corinne R. Henak, Assistant Professor, Mechanical Engineering
Darryl G. Thelen, Professor, Mechanical Engineering
Lih-Sheng Turng, Professor, Mechanical Engineering
Jacob Notbohm, Assistant Professor, Engineering Physics

ACKNOWLEDGEMENTS

I would like to start my acknowledgements by saying that my PhD was full of joy. I am eternally grateful for the constant support and encouragement I have received throughout my graduate school career, and I know I would not have been able to complete this dissertation without everyone who helped me along the way.

First, I want to thank my advisor, Dr. Melih Eriten. I am so appreciative of the opportunity to work with you. Your guidance has been instrumental in my professional and personal development. Our conversations about both school and life helped me to enhance my critical thinking abilities, inspired me, and triggered my curiosity. All of these skills have made me a better researcher and enhanced my academic journey. I appreciate your strong belief in me, endless trust, and constant support as I pursue my dream. The opportunities you gave me to attend conferences, take on leadership roles, and try new things have enhanced my graduate school experience. You have been an incredible mentor and friend. I will always remember you saying that unexpected data is not a bad thing. It sparks good discussion.

I also want to thank my advisor Dr. Corinne Henak. I have learned so much from you, and your passion for educating future engineers has inspired me. I would not be here today without your thoughtful feedback, guidance, and ability to push me beyond my comfort zone. You opened my eyes to all of the ways that engineering can be used to impact and enhance people’s lives and gave my research new meaning. You made me a better writer, presenter, and networker, and those skills have been instrumental throughout my PhD and given me more confidence as I head into the next chapter of my academic career. Because of you, I will never forget to use a topic sentence.

Thank you to my committee members Dr. Darryl Thelen, Dr. Lih-sheng Turng, and Dr. Jacob Notbohm. I appreciate your advice and support throughout my dissertation process. Dr. Thelen, I am grateful for your dedication to bringing together members of the UW Biomechanics group and creating a sense of community and comradery. Your leadership is inspiring, and I hope to follow in your footsteps. Dr. Turng, thank you for the career advice and opportunity to collaborate with Allen Yang. The project we worked on together allowed me to broaden my horizons and explore a new area of research. Dr. Notbohm, your mentorship was extremely valuable during my search for a postdoctoral position, and I am thankful for the time you took to invest in me and my future.

I am grateful to the members of The Henak Lab. Shannon Walsh, I am happy we were able to build both our knowledge and friendship together during our PhD. I appreciate you always looking out for new opportunities for me and helping me to believe in myself. I am also extremely thankful for your amazing statistical analysis skills. Jin Wook Hwang, thank you for helping me to take breaks and have fun. I learned a lot working with you, and I am happy I could be a part of your successful transition to Northwestern. Kelly Vazquez, I was able to enjoy my coursework because we did it together. I am glad we were able to grow and develop our careers side by side. Matthew Grondin, thank you for encouraging me to take coffee breaks to boost my research productivity and for all of your help with the DMMB assay. I also want to thank the rest of The Henak Lab for creating such a fun and supportive work environment.

I am also thankful for everyone in Eriten Research Group. Ahmet Usta, from my first day in the lab you have always been willing to take the time to provide guidance on using new instruments. I could not have made the progress I did on my research without your help. Shixuan Chen, thank you for encouraging me throughout the PhD defense process. Going through it

together made it easier and more fun. Lejie Lui, I am grateful that we were able to take courses together, and your positive and relaxed demeanor was uplifting and inspiring to be around. Uraching Chowdhury, thank you for your hard work and help with computational modeling. I also appreciate you being such a wonderful photographer and helping us to commemorate our graduation ceremony. Utku Boz, thank you for designing the instrument that made my research possible. Working with you broadened my knowledge about vibration. Ilke Ozsut, thank you for always staying with me late in the office. I was happy to be a part of your academic journey. Cole Hess, the trip we took to Minneapolis opened the door for this dissertation, and I was grateful to share that experience with you. I am also excited to be your neighbor soon.

I am appreciative of the help provided by Benjamin Stadnick and Richard Nay at Bruker to develop my experimental set-up. This inspired me to create new experimental methods to address my research questions.

A special thank you goes to my parents, parents-in-law, and sister. I would not be here without all of your support and trust. You always take an interest in my academic pursuits and provide constant encouragement. I also want to thank my wife. Since we met 10 years ago, you have always been by my side through both successes and challenges, and without you I could not have made it this far.

Finally, I gratefully acknowledge the funding for my dissertation that was provided by the Wisconsin Alumni Research Foundation, the University of Wisconsin-Madison Graduate School Student Research Travel Grant, and the National Science Foundation (CMMI-DCSD-1662456).

ABSTRACT

Articular cartilage is a soft biological tissue with impressive dissipation capacity and failure resistance. However, the dissipation mechanisms in the sub-failure mechanics and the failure mechanics of the tissue are incompletely understood. This dissertation attempts to address these gaps in knowledge through: (1) revealing fundamental mechanisms leading to broadband dissipation in cartilage (≥ about 5 degree phase shift), and (2) relating rate-dependent cartilage failure to dissipation mechanisms. The overall aim was accomplished via four sub-objectives. The first sub-objective was to examine the relative contribution of poroelasticity and viscoelasticity to cartilage dissipation across physiological loading rates (5-100 Hz). Poroelastic and viscoelastic dissipation mechanisms were uncoupled through dynamic testing at multiple length scales. The uncoupled mechanisms indicated that viscoelastic dissipation provided base broadband dissipation and poroelastic dissipation provided additional dissipation at relatively small length scales. The second sub-objective was to examine macroscopic cartilage dissipation as a function of matrix depletion under frequencies representative of traumatic loading (≥200 Hz). Microscopic intact and glycosaminoglycan (GAG) -depleted cartilage dissipation was measured up to 300 Hz. GAG depletion significantly increased cartilage dissipation due to altered poroelastic dissipation. The results provided the basis for understanding cartilage dissipation capacity at *in vivo* contact lengths under traumatic injury and high-rate physiological loading. The third sub-objective was to identify underlying mechanisms of rate-dependent cartilage failure. Localized cracks were induced by microindentation at two polarized loading rates. These results were analyzed via finite element modeling and nano/microscopic crack images. The results provided evidence of the link between rate-dependent cartilage failure and physical mechanisms, showing that large relaxation (collagen fibril realignment) around the tip delayed cartilage failure at the relatively slow loading rate. The fourth sub-objective was to establish the link between rate-dependent cartilage failure and poroviscoelastic relaxation as a function of matrix integrity. Rate-dependent crack nucleation in intact and GAG-depleted cartilage was generated from pre- to post-relaxation timescales. The correlation between rate-dependent crack nucleation and poroviscoelastic relaxation times was confirmed. These results indicated that rate-dependent cartilage failure was governed by the degree of relaxation prior to rupture at given matrix integrity and loading rates. These outcomes further our understanding of cartilage failure at different stages of degeneration. In conclusion, these findings in this dissertation widen our knowledge about the cartilage dissipation and failure.

TABLE OF CONTENTS

LIST OF FIGURES

Page

Chapter 1 Introduction

1.1. Motivation and objectives

Articular cartilage is a load-bearing and dissipative material located on the articulating joints. Cartilage is a thin, translucent, and hydrated layer (0.5 – 5.0 mm thickness [1]) composed of fluid and solid phases (Figure 1-1a). Interstitial fluid is the largest constituent (about 60 – 85 % of wet weight), and it swells the solid matrix (about 30 % of total water) and pore space [1–3]. The solid phase is comprised of extracellular matrix and chondrocytes. Extracellular matrix is primarily made of collagen fibrils and proteoglycans (PGs). Collagen fibrils are the largest portion of macromolecules in the solid phase (about 15 – 22 % of wet weight [1]). About 90 – 95 % of collagen fibrils are type II collagen and the rest includes other collagen types such types V, VI, IX, X, XI, XII, and XIV [1,4]. Collagen fibrils are organized parallel to the articular surface in the superficial zone and perpendicular to the articular surface in the deep zone (Figure 1-1b) [1], and their diameter increase from 20 to 120 nm toward the deep zone [5]. The pore size of the collagen fibril network is approximately 60 - 200 nm [6,7]. PGs are the second largest portion of macromolecules in the solid phase (about 4 – 7 % of wet weight [1]). PGs are composed of core proteins combined with glycosaminoglycan (GAG) side chains that are highly negatively charged [1]. They are divided according to their relative size (e.g., aggrecans are large PGs while decorin, biglycan, and fibromodulin are small PGs) [8,9]. PG concentration increases toward the deep zone [10,11]. The pore space formed with PGs and collagen fibrils is approximately 2 – 12 nm [1,12]. Chondrocytes are the only cells embedded in cartilage and are sparsely distributed [1,10]. They only comprise about 2 % of total volume of adult articular cartilage and are relatively flatter and smaller in the superficial zone compared to the deep zone [4,10]. In summary, articular cartilage is a highly heterogeneous and composite material that distributes loads in mammalian joints during *in vivo* activities.

The solid matrix is responsible for mechanical and dissipative responses of articular cartilage (Figure 1-1). PGs/GAGs provide swelling force through osmotic pressure and electrostatic repulsion between charges and therefore are responsible for compressive strength of cartilage [1,13]. The dense collagen matrix resists the swelling force under tension [14–16]. Cartilage dissipation mechanisms are characterized as poroelastic (PE) and intrinsic viscoelastic (VE) dissipation. PE dissipation results from solid-fluid frictional interaction, which occurs when pressurized fluid flows through a dense solid matrix and therefore is fluid-dependent dissipation [17–19]. Intrinsic VE dissipation results from stress-induced molecular rearrangement and friction between and within the solid matrix macromolecules and thus is flow-independent dissipation [19–21]. PE and VE relaxation mechanisms explain rate-dependent mechanical behavior of cartilage [16,20–24].

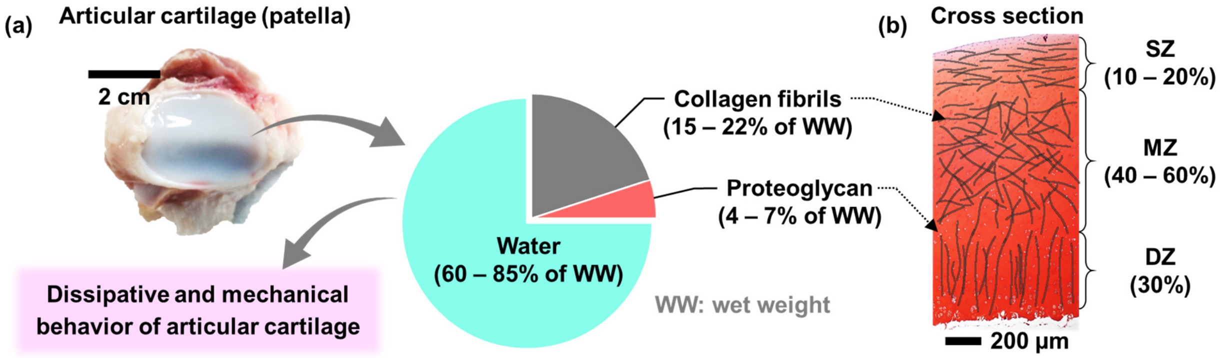

Figure 1-1: (a) Components of articular cartilage governing dissipative and mechanical responses of cartilage and (b) its cross section. (b) is the combination of a histological image of cartilage (Safranin-O and fast green staining) with sketches for zonal organization (SZ: superficial zone, MZ: middle zone, and DZ: deep zone).

Excellent broadband dissipation capacity of cartilage has been observed in the sub-failure regime, but underlying mechanisms are incompletely understood. Previous work investigated PE dissipation over a wide range of frequency (0.2 – 10 kHz) and showed that PE dissipation is dominant at small contact length scales (about 5-6 μm) [17,22]. Other studies examined VE dissipation up to relatively lower frequencies (≤ about 95 Hz) and showed that VE dissipation is dominant at large contact length scales (≥ about 2 mm) and under shear loading [25–29]. Although these previous studies suggested that cartilage dissipation was length- and rate-dependent, they studied PE and VE dissipation mechanisms separately at polarized contact length scales. These extremely different length scales combined with the different test configurations made it difficult to understand the relative contribution of PE and VE mechanisms to cartilage dissipation. A range of contact scales inducing a transition from PE to VE dissipation in physiological loading frequencies has not been identified.

In addition, while cartilage dissipation at microscale lengths have been investigated up to high-frequency loading as a function of cartilage integrity, it was only partially explored at macroscopic length scales. For example, the effect of cartilage degeneration on dissipation was studied at microscale contact lengths (about 5-6 μm) from 1 Hz to 10 kHz, and it was revealed that increased permeability due to GAG depletion shifted maximum dissipation with a phase angle of about 45 degrees from a relatively low frequency (about 45 Hz) to a relatively high frequency (about 800 Hz) [17,22]. This result provides microscopic cartilage dissipation over the frequency contents involved while walking (1-8 Hz), running (4-100 Hz) and jumping (2-100 Hz), accompanying heel strike, and during traumatic impact (≥200 Hz) [22,30–34]; the frequency estimations on walking, running, and jumping were not verified by independent measurements of actual loading on cartilage and therefore might be exaggerated because loading on cartilage is transmitted from soft dissipative tissues such as tendon. However, macroscopic cartilage dissipation as a function of matrix integrity was only investigated up to 40-95 Hz [25–28]. Therefore, macroscopic cartilage under high-frequency loading (≥ 100 Hz) remains unexplored in the sub-failure regime and is of interest to understand dissipative behavior of cartilage in response to traumatic impact at *in vivo* contact length scales [35,36].

Compared to roles of poroviscoelastic (PVE) mechanism in cartilage sub-failure behavior, not much is known about the links between rate-dependent cartilage failure and PVE mechanism. Cartilage shows impressive resistance to failure under *in vivo* loading scenarios for decades in healthy joints. Nevertheless, it can break down due to load-induced damage. As cartilage exhibits very limited capacity of self-repair [37], understanding failure mechanisms is critical to prevent damage. These clinical problems, combined with interest in origins of excellent resistance, have motivated a few studies. For example, tension and compression testing showed that cartilage failure is delayed under low-frequency loading compared to fast-frequency loading [38–40]. Extraction of PGs increased the rate of creep while not affecting failure stress under slow constant-rate tensile testing [41]. Localized loading induced by a sharp blade showed that crack nucleation in cartilage was rate-dependent and removal of 500 μm thickness from articular surface caused relatively localized strain in the vicinity of a blade compared to intact surface [42]. These previous studies suggested that cartilage failure is rate-dependent, but the links between rate-dependent cartilage and PVE relaxation are not established. In particular, rate-dependent cartilage failure was incompletely linked to nano/microscopic length scales; this link was relatively well established in other collagen-rich tissues, such as skin, through nano/microscopic observation of solid matrices under tensile loading and after failure [43–46]. In addition, the effects of cartilage integrity on rate-dependent cartilage failure have not been examined. This is of interest because mechanically induced cartilage injuries can be caused at various stages of cartilage integrity and loading rates.

To fill these gaps, the overall aim of this dissertation was twofold: (1) revealing underlying mechanisms leading to broadband cartilage dissipation (≥ about 5 degree phase shift) and (2) relating rate-dependent cartilage failure to dissipation mechanisms. The overall objective was achieved through four specific objectives (Figure 1-2):

Objective 1: Investigate the relative contribution of poroelasticity and viscoelasticity to cartilage dissipation over physiological loading frequencies (5-100 Hz). Dynamic mechanical analysis of intact cartilage is conducted across multiple length scales over physiological loading frequencies. The main outcome is phase shift curves across multiple length scales. They are used to uncouple PE and VE dissipation in the frequency of interest, ultimately providing the relative contribution of two mechanisms to broadband cartilage dissipation.

Objective 2: Investigate macroscopic cartilage dissipation as a function of solid matrix integrity under high-frequency loading in order to explore formerly unexamined trauma loading rates (≥200 Hz). Dynamic mechanical analysis of intact and GAG-depleted cartilage is performed at a macroscopic contact length up to 300 Hz. The main consequence is phase shift curves as a function of cartilage integrity and strain, providing the effects of GAG depletion on macroscopic cartilage dissipation under high-frequency loading.

Objective 3: Identify underlying mechanisms of rate-dependent crack nucleation in intact cartilage under microindentation using a PVE framework and nano/microscopic images. Microindentation-based crack nucleation tests are conducted on intact cartilage at two polarized loading rates. The results are further analyzed via finite element (FE) modeling and images of crack surfaces. The main outcome is the link between rate-dependent crack nucleation and rate-dependent morphological features of crack surfaces, suggesting possible physical origins of rate-dependent cartilage failure.

Objective 4: Establish the link between rate-dependent crack nucleation and PVE relaxation as a function of cartilage integrity. Crack nucleation in intact and GAG-depleted cartilage is induced under microindentation at multiple loading rates, and their PVE relaxation responses are measured. The main outcomes are the effect of GAG depletion on rate-dependent crack nucleation and the experimental link between rate-dependent crack nucleation and relaxation. They provide possible mechanisms underlying rate-dependent cartilage failure at different stages of degeneration.

Chapters 2 and 3 provide the detailed description and findings regarding *Objective 1* and *2*, respectively. Learning outcomes of *Objective 1* and *2* about cartilage dissipation mechanisms in sub-failure regime lays the foundation for *Objectives 3* and *4* about the link between rate-dependent cartilage failure and dissipation mechanisms. *Chapters 4* and *5* provide the details of *Objective 3* and *4*, respectively. *Chapter 6* presents conclusions and future work.

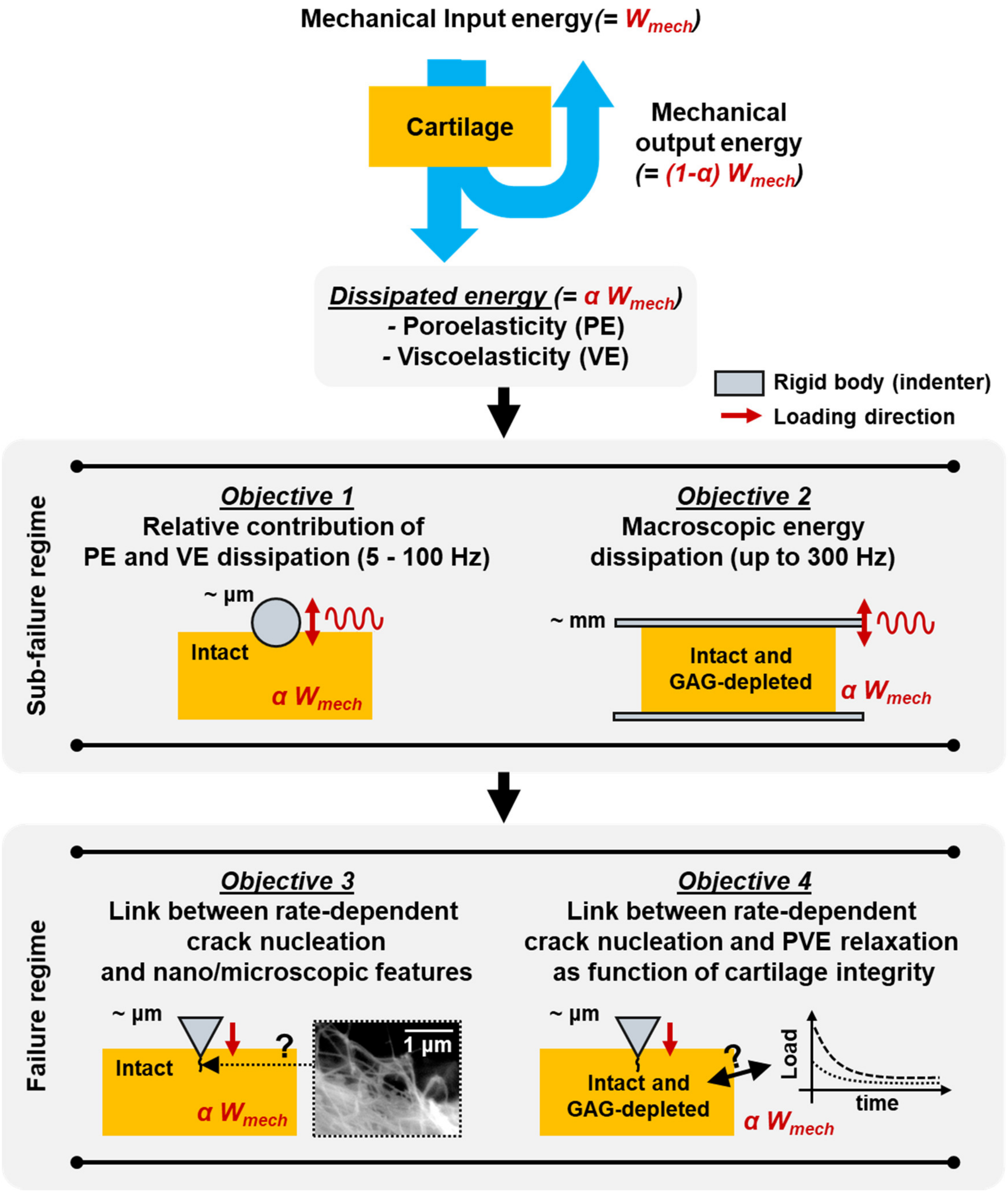

Figure 1-2: Schematic overview of research. Cartilage dissipates a part of mechanical input energy, αW_{mech}. Learning outcomes from *Objectives 1* and *2* form the foundation for *Objectives 3* and *4*. These objectives were achieved by conducting mechanical tests across multiple length- (µm to mm) and time- (quasi-static to traumatic impact) scales, FE analysis, and nano/microscopic imaging.

1.2. References

[1] Mow, V. C., Ratcliffe, A., and Robin Poole, A., 1992, "Cartilage and Diarthrodial Joints as Paradigms for Hierarchical Materials and Structures," Biomaterials, 13(2), pp. 67–97.

[2] Maroudas, A., Wachtel, E., Grushko, G., Katz, E. P., and Weinberg, P., 1991, "The Effect of Osmotic and Mechanical Pressures on Water Partitioning in Articular Cartilage," Biochim. Biophys. Acta BBA - Gen. Subj., 1073(2), pp. 285–294.

[3] Torzilli, P. A., 1985, "Influence of Cartilage Conformation on Its Equilibrium Water Partition," J. Orthop. Res., 3(4), pp. 473–483.

[4] Alford, J. W., and Cole, B. J., 2005, "Cartilage Restoration, Part 1: Basic Science, Historical Perspective, Patient Evaluation, and Treatment Options," Am. J. Sports Med., 33(2), pp. 295–306.

[5] Poole, A. R., Kojima, T., Yasuda, T., Mwale, F., Kobayashi, M., and Laverty, S., 2001, "Composition and Structure of Articular Cartilage: A Template for Tissue Repair," Clin. Orthop., (391 Suppl), pp. S26-33.

[6] Bajpayee, A. G., and Grodzinsky, A. J., 2017, "Cartilage-Targeting Drug Delivery: Can Electrostatic Interactions Help?," Nat. Rev. Rheumatol., 13(3), pp. 183–193.

[7] Hall, B. K., and Newman, S. A., 1991, *Cartilage Molecular Aspects*, CRC Press.

[8] Bhosale, A. M., and Richardson, J. B., 2008, "Articular Cartilage: Structure, Injuries and Review of Management," Br. Med. Bull., 87, pp. 77–95.

[9] Iozzo, R. V., and Schaefer, L., 2015, "Proteoglycan Form and Function: A Comprehensive Nomenclature of Proteoglycans," Matrix Biol., 42, pp. 11–55.

[10] Sophia Fox, A. J., Bedi, A., and Rodeo, S. A., 2009, "The Basic Science of Articular Cartilage: Structure, Composition, and Function," Sports Health, 1(6), pp. 461–468.

[11] Yin, J., Xia, Y., and Lu, M., 2012, "Concentration Profiles of Collagen and Proteoglycan in Articular Cartilage by Fourier Transform Infrared Imaging and Principal Component Regression," Spectrochim. Acta. A. Mol. Biomol. Spectrosc., 88, pp. 90–96.

[12] Majda, D., Bhattarai, A., Riikonen, J., Napruszewska, B. D., Zimowska, M., Michalik-Zym, A., Töyräs, J., and Lehto, V.-P., 2017, "New Approach for Determining Cartilage Pore Size Distribution: NaCl-Thermoporometry," Microporous Mesoporous Mater., 241, pp. 238–245.

[13] Han, E., Chen, S. S., Klisch, S. M., and Sah, R. L., 2011, "Contribution of Proteoglycan Osmotic Swelling Pressure to the Compressive Properties of Articular Cartilage," Biophys. J., 101(4), pp. 916–924.

[14] Andriotis, O. G., Desissaire, S., and Thurner, P. J., 2018, "Collagen Fibrils: Nature's Highly Tunable Nonlinear Springs," ACS Nano, 12(4), pp. 3671–3680.

[15] Kempson, G. E., Freeman, M. a. R., and Swanson, S. a. V., 1968, “Tensile Properties of Articular Cartilage,” Nature, 220(5172), pp. 1127–1128.

[16] Soulhat, J., Buschmann, M. D., and Shirazi-Adl, A., 1999, “A Fibril-Network-Reinforced Biphasic Model of Cartilage in Unconfined Compression,” J. Biomech. Eng., 121(3), pp. 340–347.

[17] Nia, H., Han, L., Li, Y., Ortiz, C., and Grodzinsky, A., 2011, “Poroelasticity of Cartilage at the Nanoscale,” Biophys. J., 101(9), pp. 2304–2313.

[18] Nia, H., Han, L., Soltani Bozchalooi, I., Roughley, P., Youcef-Toumi, K., Grodzinsky, A. J., and Ortiz, C., 2015, “Aggrecan Nanoscale Solid–Fluid Interactions Are a Primary Determinant of Cartilage Dynamic Mechanical Properties,” ACS Nano, 9(3), pp. 2614–2625.

[19] Lakes, P. R., 2009, *Viscoelastic Materials*, Cambridge University Press, Cambridge ; New York.

[20] Mak, A. F., 1986, “The Apparent Viscoelastic Behavior of Articular Cartilage—The Contributions from the Intrinsic Matrix Viscoelasticity and Interstitial Fluid Flows,” J. Biomech. Eng., 108(2), pp. 123–130.

[21] Huang, C.-Y., Soltz, M. A., Kopacz, M., Mow, V. C., and Ateshian, G. A., 2003, “Experimental Verification of the Roles of Intrinsic Matrix Viscoelasticity and Tension-Compression Nonlinearity in the Biphasic Response of Cartilage,” J. Biomech. Eng., 125(1), pp. 84–93.

[22] Nia, H., Bozchalooi, I. S., Li, Y., Han, L., Hung, H.-H., Frank, E., Youcef-Toumi, K., Ortiz, C., and Grodzinsky, A., 2013, “High-Bandwidth AFM-Based Rheology Reveals That Cartilage Is Most Sensitive to High Loading Rates at Early Stages of Impairment,” Biophys. J., 104(7), pp. 1529–1537.

[23] Chiravarambath, S., Simha, N. K., Namani, R., and Lewis, J. L., 2008, “Poroviscoelastic Cartilage Properties in the Mouse from Indentation,” J. Biomech. Eng., 131(1), pp. 011004-011004–9.

[24] Huang, C. Y., Mow, V. C., and Ateshian, G. A., 2001, “The Role of Flow-Independent Viscoelasticity in the Biphasic Tensile and Compressive Responses of Articular Cartilage,” J. Biomech. Eng., 123(5), pp. 410–417.

[25] Fulcher, G. R., Hukins, D. W. L., and Shepherd, D. E. T., 2009, “Viscoelastic Properties of Bovine Articular Cartilage Attached to Subchondral Bone at High Frequencies,” BMC Musculoskelet. Disord., 10, p. 61.

[26] Lawless, B. M., Sadeghi, H., Temple, D. K., Dhaliwal, H., Espino, D. M., and Hukins, D. W. L., 2017, “Viscoelasticity of Articular Cartilage: Analysing the Effect of Induced Stress and the Restraint of Bone in a Dynamic Environment,” J. Mech. Behav. Biomed. Mater., 75, pp. 293–301.

[27] Griffin, D. J., Vicari, J., Buckley, M. R., Silverberg, J. L., Cohen, I., and Bonassar, L. J., 2014, “Effects of Enzymatic Treatments on the Depth-Dependent Viscoelastic Shear Properties of Articular Cartilage,” J. Orthop. Res., 32(12), pp. 1652–1657.

[28] Park, S., Nicoll, S. B., Mauck, R. L., and Ateshian, G. A., 2008, “Cartilage Mechanical Response under Dynamic Compression at Physiological Stress Levels Following Collagenase Digestion,” Ann. Biomed. Eng., 36(3), pp. 425–434.

[29] Buckley, M. R., Bonassar, L. J., and Cohen, I., 2013, “Localization of Viscous Behavior and Shear Energy Dissipation in Articular Cartilage Under Dynamic Shear Loading,” J. Biomech. Eng., 135(3), pp. 031002-031002–9.

[30] Cross, R., 1999, “Standing, Walking, Running, and Jumping on a Force Plate,” Am. J. Phys., 67(4), pp. 304–309.

[31] Tanaka, Y., Shiokawa, M., Yamashita, H., and Tsuji, T., 2006, “Manipulability Analysis of Kicking Motion in Soccer Based on Human Physical Properties,” pp. 68–73.

[32] Dickinson, J. A., Cook, S. D., and Leinhardt, T. M., 1985, “The Measurement of Shock Waves Following Heel Strike While Running,” J. Biomech., 18(6), pp. 415–422.

[33] Richards, D. P., Ajemian, S. V., Wiley, J. P., and Zernicke, R. F., 1996, “Knee Joint Dynamics Predict Patellar Tendinitis in Elite Volleyball Players,” Am. J. Sports Med., 24(5), pp. 676–683.

[34] Heiner, A. D., Martin, J. A., McKinley, T. O., Goetz, J. E., Thedens, D. R., and Brown, T. D., 2012, “Frequency Content of Cartilage Impact Force Signal Reflects Acute Histologic Structural Damage,” Cartilage, 3(4), pp. 314–322.

[35] Chan, D. D., Cai, L., Butz, K. D., Trippel, S. B., Nauman, E. A., and Neu, C. P., 2016, “*In Vivo* Articular Cartilage Deformation: Noninvasive Quantification of Intratissue Strain during Joint Contact in the Human Knee,” Sci. Rep., 6, p. 19220.

[36] Fukubayashi, T., and Kurosawa, H., 1980, “The Contact Area and Pressure Distribution Pattern of the Knee: A Study of Normal and Osteoarthrotic Knee Joints,” Acta Orthop. Scand., 51(1–6), pp. 871–879.

[37] Cheng, A., Hardingham, T. E., and Kimber, S. J., 2014, “Generating Cartilage Repair from Pluripotent Stem Cells.,” Tissue Eng. Part B Rev., 20(4), pp. 257–266.

[38] Sadeghi, H., Lawless, B. M., Espino, D. M., and Shepherd, D. E. T., 2018, “Effect of Frequency on Crack Growth in Articular Cartilage,” J. Mech. Behav. Biomed. Mater., 77(Supplement C), pp. 40–46.

[39] Sadeghi, H., Shepherd, D. E. T., and Espino, D. M., 2015, “Effect of the Variation of Loading Frequency on Surface Failure of Bovine Articular Cartilage,” Osteoarthritis Cartilage, 23(12), pp. 2252–2258.

[40] Kaplan, J. T., Neu, C. P., Drissi, H., Emery, N. C., and Pierce, D. M., 2017, "Cyclic Loading of Human Articular Cartilage: The Transition from Compaction to Fatigue," J. Mech. Behav. Biomed. Mater., 65, pp. 734–742.

[41] Schmidt, M. B., Mow, V. C., Chun, L. E., and Eyre, D. R., 1990, "Effects of Proteoglycan Extraction on the Tensile Behavior of Articular Cartilage," J. Orthop. Res. Off. Publ. Orthop. Res. Soc., 8(3), pp. 353–363.

[42] Bartell, L. R., Xu, M. C., Bonassar, L. J., and Cohen, I., 2018, "Local and Global Measurements Show That Damage Initiation in Articular Cartilage Is Inhibited by the Surface Layer and Has Significant Rate Dependence," J. Biomech.

[43] Arumugam, V., Naresh, M. D., and Sanjeevi, R., 1994, "Effect of Strain Rate on the Fracture Behaviour of Skin," J. Biosci., 19(3), pp. 307–313.

[44] Yang, W., Sherman, V. R., Gludovatz, B., Schaible, E., Stewart, P., Ritchie, R. O., and Meyers, M. A., 2015, "On the Tear Resistance of Skin," Nat. Commun., 6, p. 6649.

[45] Sherman, V. R., Yang, W., and Meyers, M. A., 2015, "The Materials Science of Collagen," J. Mech. Behav. Biomed. Mater., 52, pp. 22–50.

[46] Bircher, K., Zündel, M., Pensalfini, M., Ehret, A. E., and Mazza, E., 2019, "Tear Resistance of Soft Collagenous Tissues," Nat. Commun., 10(1), p. 792.

Chapter 2 Uncoupled poroelastic and intrinsic viscoelastic dissipation in cartilage*

Guebum Han, Cole Hess, Melih Eriten, and Corinne R. Henak

*(*Reprinted from Journal of the Mechanical Behavior of Biomedical Materials*
with permission from Elsevier)

2.1. Abstract

This paper studies uncoupled poroelastic (flow-dependent) and intrinsic viscoelastic (flow-independent) energy dissipation mechanisms via their dependence on characteristic lengths to understand the root of cartilage's broadband dissipation behavior. Phase shift and dynamic modulus were measured from dynamic microindentation tests conducted on hydrated cartilage at different contact radii, as well as on dehydrated cartilage. Cartilage weight and thickness were recorded during dehydration. Phase shifts revealed poroelastic- and viscoelastic-dominant dissipation regimes in hydrated cartilage. Specifically, phase shift at a relatively small radius was governed by poroviscoelasticity, while phase shift at a relatively large radius was dominantly governed by intrinsic viscoelasticity. The uncoupled dissipation mechanisms demonstrated that intrinsic viscoelastic dissipation provided sustained broadband dissipation for all length scales, and additional poroelastic dissipation increased total dissipation at small length scales. Dehydration decreased intrinsic viscoelastic dissipation of cartilage. The findings demonstrated a possibility to measure poroelastic and intrinsic viscoelastic properties of cartilage at similar microscale lengths. Also they encouraged development of broadband cartilage like-dampers and provided important design parameters to maximize their performance.

Keywords Cartilage; poroelasticity; viscoelasticity; energy dissipation; broad dissipation

2.2. Introduction

Articular cartilage is a connective tissue that functions as a load-bearing and dissipative material over a broadband spectrum of loading frequency. Cartilage has a heterogeneous structure composed of the dense solid matrix (e.g., collagen fibrils and proteoglycans) and fluid [1]. Fluid is the largest constituent (about 60 – 85 % of wet weight), and it plays an important role in swelling intrafibriliar space (about 30 % of total water) and extrafibriliar space [1–3]. Cartilage dehydrates and rehydrates due to pressure-induced exudation of fluid through the solid matrix under normal loading conditions *in vivo*. Time-dependent properties of cartilage are from coupled mechanisms of the solid matrix and fluid flow. The mechanisms have been characterized as poroelasticity and intrinsic viscoelasticity, resulting in efficient and sustained broadband dissipative properties [4–7].

Previous studies have provided evidence on poroelasticity and intrinsic viscoelasticity of cartilage, but the relative contributions of the two are unclear. Poroelasticity-driven dissipation and response originates from solid-fluid frictional (viscous drag) interaction, and therefore is flow-dependent [4,8]. Previous studies showed that poroelasticity-driven dissipation was dominant at relatively small length scales (about 5-6 um) under oscillatory loading [4,5]. Intrinsic viscoelasticity-driven dissipation is associated with delay due to molecular friction and rearrangement of a solid matrix [4,8], and therefore is flow-independent [9–11]. Previous work measured intrinsic viscoelasticity of cartilage by employing macroscale compression tests [6,7,9,10] and small magnitude shear loading [12]. Although a few studies have individually measured poroelasticity [4,5] and intrinsic viscoelasticity of cartilage [6,7] over a wide spectrum of frequency, their relative contributions have not been uncoupled from each other. Also, it is difficult to utilize previously reported results to uncouple the mechanisms because test length scales (about 5-6 μm for poroelasticity (local) versus about 5 mm for intrinsic viscoelasticity (full-thickness)) are polarized, and therefore depth-dependent heterogeneous structure (e.g., collagen direction and diameter) of cartilage cannot be compared precisely.

Poroelasticity-driven dissipation is length-dependent, while intrinsic viscoelasticity-driven dissipation is not. This difference provides a means to distinguish the contributions of the two. Poroelastic dissipation is flow-dependent, and therefore is associated with characteristic poroelastic diffusion time. The diffusion time is proportional to the squared of a characteristic length (e.g., contact radius) [4,11]. Consequently, a characteristic length can govern poroelasticity-driven dissipation. A poroelasticity-driven dissipation spectrum moves toward a low frequency range as a characteristic length increases, and its peak frequency, f_{poro}, can be estimated with poroelastic diffusion time (Figure 2-1) [4,11]. In contrast, intrinsic viscoelastic dissipation is flow-independent [9–11]. Accordingly, an intrinsic viscoelasticity-driven dissipation spectrum and its peak frequency, f_{visco}, are independent of a characteristic length (Figure 2-1). Consequently, the two dissipation mechanisms can be distinguished over a broad frequency range by carefully selecting characteristic lengths.

The main aim of this study is to understand the origin of cartilage's broadband dissipation behavior by uncoupling the poroelastic and intrinsic viscoelastic dissipation mechanisms through their dependence on characteristic lengths. Phase shifts, a measure of dissipation, were measured at three different contact radii (characteristic lengths). Results of phase shifts were compared to uncouple the dissipation mechanisms. Dynamic moduli were also measured to examine dynamic response of cartilage based on the uncoupled dissipation mechanisms. In addition, phase shift and dynamic modulus of dehydrated cartilage were measured to further investigate the effect of fluid loss on broadband dissipative and mechanical properties.

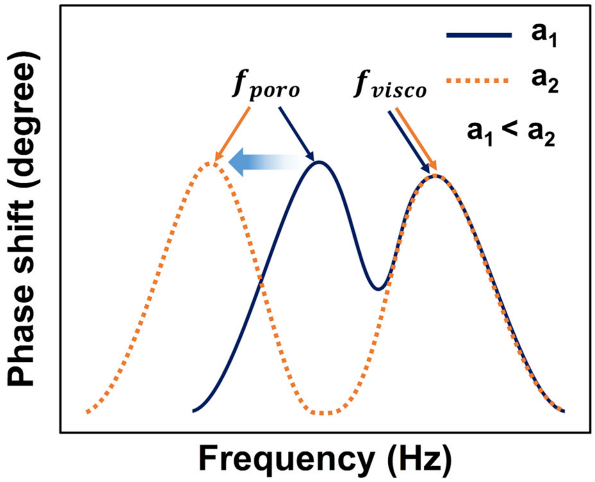

Figure 2-1: Schematic diagram of dependence of poroelastic and intrinsic viscoelastic energy dissipation on contact radii. The poroelastic peak frequency, f_{pore}, is inversely proportional to the square of the contact radius, *a* (Eq. 2-5). Therefore, the effects of the two mechanisms can be uncoupled by performing dynamic testing at different contact radii.

2.3. Method

2.3.1. Sample Preparation

Full-thickness cartilage samples were harvested from patellae of porcine joints (12 animals, 5-6 months old, gender unknown and assumed random). Cylindrical samples with a diameter of 6 mm were obtained using a biopsy punch and a scalpel. Subchondral bone was trimmed using a microtome to create a level articular surface for indentation testing. The deep zone of each sample was adhered to the center of a glass petri dish (Loctite 495, Henkel, Germany). Dulbecco's phosphate-buffered saline (DPBS) was used to keep samples hydrated during preparation.

2.3.2. Dehydration curve of cartilage

Dehydration of cartilage was evaluated to determine how long to dehydrate cartilage for testing. Samples were dehydrated at room temperature of 20.9 °C and relative humidity of 25 %. The weight of cartilage was measured every 10 minutes for 3 hours using an analytical electronic balance (MS104TS, Mettler Toledo, OH). After 3 hours, the weight of cartilage was measured every 20 minutes until 4 hours of dehydration, and then the weight was measured at 5 hours. The thickness of cartilage was also measured every 45 minutes using a digital calliper before 2 hours of dehydration. After 2 hours, the thickness was measured every hour until 5 hours of dehydration. The measured weight and thickness of cartilage during dehydration were normalized with the initial weight and thickness. A total of three samples were tested, they were from one patella.

2.3.3. Broadband dynamic indentation tests

Dynamic microindentation tests were conducted to measure phase shift and dynamic modulus, in order to uncouple poroelastic and viscoelastic effects. Tests were conducted on a Hysitron TI950 TriboIndenter (Bruker Inc, Minneapolis, MN) using a diamond sphero-conical indenter with a tip radius of 50 µm and cone semi-angle of 45°, and a sapphire spherical indenter with a tip radius of 1 mm. For each test, a static displacement was applied and held until equilibrium, then a small amplitude (0.5-2 nm) frequency sweep was applied. Open-loop control setting was used, resulting in curves similar to force-relaxation curves for hydrated cartilage (Figure 2-2b) and curves similar to creep curves for dehydrated cartilage. A slight drift in force measurement was observed, likely from thermal drift [11]. A reference frequency technique was employed to minimize the effect of the drift by correcting contact area based on measured stiffness at a reference frequency [13]. A 220 Hz reference frequency was imposed between test frequencies.

Contact radii were adjusted by changing the indenter or the static displacement (Figure 2-2). Equilibrium time and frequencies tested varied as a function of the contact radius. Hydrated cartilage was tested with three contact radii, and was kept hydrated with DPBS during tests. The smallest contact radius, $a_{small} = 13.21 \pm 0.59$ µm, was achieved with the 50 µm radius sphero-conical indenter, held at a static displacement of 3.50 ± 0.32 µm for 20 seconds, followed by a frequency sweep from 5 Hz to 100 Hz in 7 randomized segments (contact area: $549.20 \pm 49.52\ \mu\text{m}^2$). The middle contact radius, $a_{\text{medium}} = 32.77 \pm 0.77\ \mu\text{m}$, was achieved with the 1 mm radius tip, held at a static displacement of $1.07 \pm 0.05\ \mu\text{m}$ for 40 seconds, followed by a frequency sweep from 5 Hz to 100 Hz in 4 randomized segments (contact area: $3375.43 \pm 158.20\ \mu\text{m}^2$). The largest contact radius, $a_{\text{large}} = 43.13 \pm 0.85\ \mu\text{m}$, was achieved with the 1 mm radius tip, held at a static displacement of $1.86 \pm 0.07\ \mu\text{m}$ for 100 seconds, followed by a frequency sweep in 4 randomized segments from 25 Hz to 100 Hz (contact area: $5846.20 \pm 229.21\ \mu\text{m}^2$). A low frequency of 5 Hz had to be sacrificed due to limitations in the number of data acquisition points coupled with the long time for equilibrium. Dynamic indentation tests were performed on dehydrated cartilage with a single indenter (tip radius of 50 µm) because no flow-dependent effects were expected. Cartilage was dehydrated for 5 hours in the condition used for obtaining the dehydration curves; 5 hours were determined based on the curves. The tip was indented, held a static displacement of $0.68 \pm 0.14\ \mu\text{m}$ for 20 seconds, resulting in a contact radius of $5.79 \pm 0.60\ \mu\text{m}$ (contact area: $103.19 \pm 23.94\ \mu\text{m}^2$). Following the 20 second equilibrium, a frequency sweep from 5 Hz to 100 Hz (7 segments, randomized) was implemented. For all tests, displacements and contact radii were estimated at about 10 seconds before the end of tests. Contact radii, a, were estimated by using Hertzian contact theory [14]:

$$a = \sqrt{R\delta_{static}} \tag{2-1}$$

where R is the indenter radius and δ_{static} is the static displacement (Figure 2-2). Each testing configuration - hydrated at three radii and dehydrated - was tested at three locations on three samples. Each sample was from different patella, taken from two animals. Test locations were selected near the center of samples to avoid the effect of edge on measurement results.

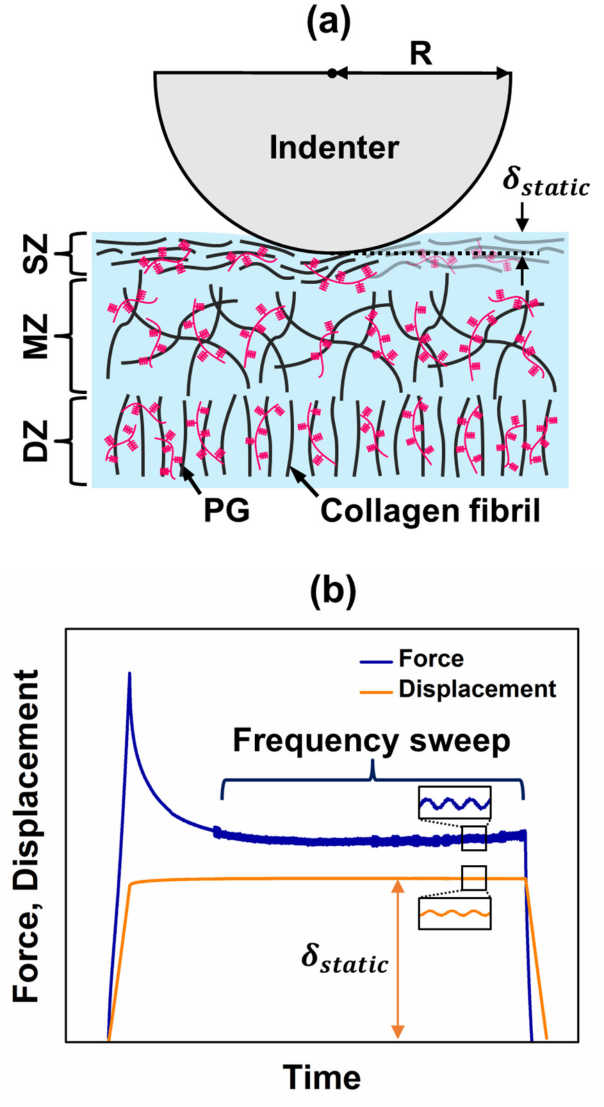

Figure 2-2: (a) Schematic diagram of contact between impermeable indenter and cartilage and (b) representatives of force-time and displacement-time curves from hydrated cartilage. R and δ_{static} are the tip radius and the static displacement, respectively. SZ, MZ, and DZ are superficial zone, middle zone, and deep zone, respectively. Since δ_{static} (about 1-3 μm) was shallow, the measured values were from SZ (10-20% of total thickness [1] = about 300 μm).

2.3.4. Estimation of poroelastic peak frequency from force relaxation curve

The poroelastic peak frequency, f_{poro}, was estimated to check if the experimentally-measured trend of phase shift versus frequency was consistent with the theoretical peak. This information was used as secondary confirmation of poroelastic dominant dissipation. To estimate f_{poro}, diffusivity, D, of hydrated cartilage was obtained by fitting an experimental force relaxation curve to a master curve for a half-space poroelastic material under a spherical indenter (rigid, frictionless, and impermeable) [15]. A portion of a force relaxation curve with a 50 µm radius tip (before the dynamic load application) was used as $F(t)$ because the displacement was constantly maintained even under an open-loop control setting. First, diffusion at time, t, was estimated as a length scale, l_{PE}, as follows [15]:

$$l_{PE} = \sqrt{Dt} \tag{2-2}$$

Next, an experimental force relaxation curve, $F(t)$, was normalized into a dimensionless curve, g, by using l_{PE} and a at δ_{static} as follows [15]:

$$\frac{F(t) - F(\infty)}{F(0) - F(\infty)} = g\left(\frac{l_{PE}^2}{a^2}\right) = g\left(\frac{Dt}{a^2}\right) = g(\tau) \tag{2-3}$$

where $F(0)$ and $F(\infty)$ are the instantaneous force at time = 0 s and the equilibrium force at infinite time, respectively. $F(0)$, $F(\infty)$, and D were fitting parameters, and they were initially guessed for the purpose of normalizing a force relaxation curve. The normalized dimensionless curve was fitted with the fitting parameters to a master curve [15]:

$$g(\tau) = 0.491e^{-0.908\sqrt{\tau}} + 0.509e^{-1.679\tau}. \tag{2-4}$$

As a result of the curve fitting, $F(0)$, $F(\infty)$, and D were determined, allowing f_{poro} to be estimated [4,11]:

$$f_{poro} \sim \frac{1}{\tau_{poro}} = \frac{D}{a^2} \tag{2-5}$$

where τ_{poro} is the poroelastic time constant.

2.3.5. Statistical Analysis

The Kruskal-Wallis test was used to determine the statistical difference in phase shift and dynamic modulus among four test sets (hydrated cartilage at a_{small}, a_{medium}, and a_{large}, and dehydrated cartilage). If a significant difference was found from the above step, the Mann-Whitney U test was used to identify the source of the significant difference by comparing two test sets. In addition, the Kruskal-Wallis test was used to determine the dependence of phase shift and dynamic modulus on frequency in each test set. All statistical analysis was conducted using MATLAB (The MathWorks, Inc., Natick, MA). A significance level of 5% was employed for all tests.

2.4. Results

Phase shifts of hydrated cartilage from a_{small} were significantly different from those from a large contact radius (i.e., a_{medium} and a_{large}) ($p<0.05$) (Figure 2-3a). Phase shift from a_{small} gradually decreased from 5 Hz to 100 Hz, and its dependence on frequency was significant ($p<0.05$). The maximum and minimum values were 30.50 ± 2.19 degrees at 5 Hz and 13.74 ± 1.28 degrees at 100 Hz, respectively. Phase shift from a_{medium} was steady over the frequency range, and it was not significantly frequency-dependent ($p>0.05$). The values at 5 Hz and 100 Hz were 9.97 ± 1.50 degrees and 8.16 ± 2.87 degrees, respectively. Phase shift from a_{medium} was lower than that from a_{small} over the frequency range (20.53 degrees at 5 Hz and 5.58 degrees at 100 Hz).

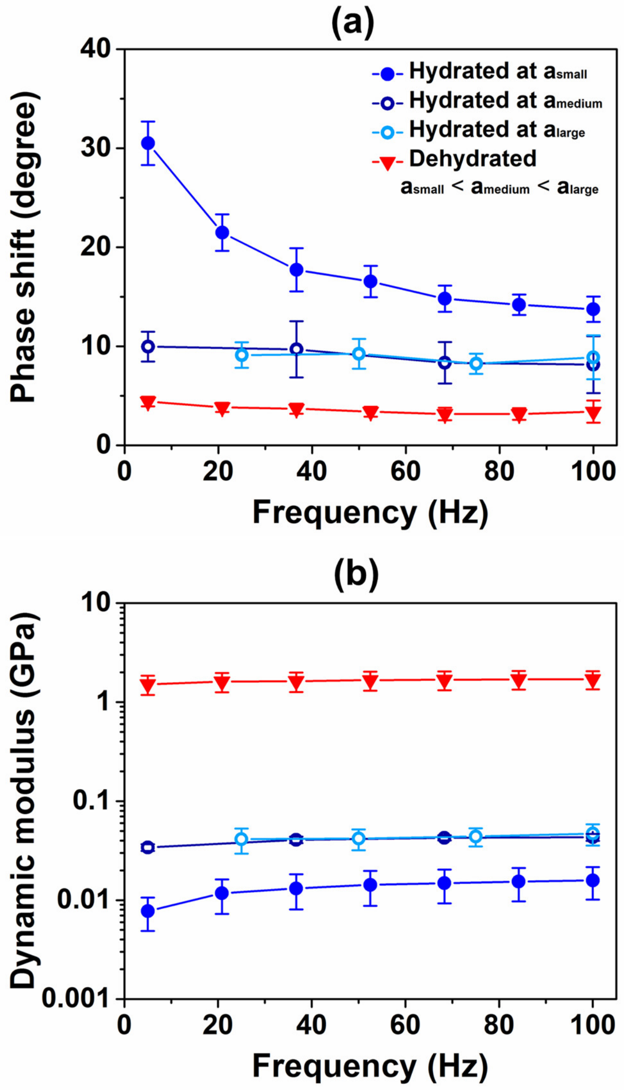

Figure 2-3: (a) Phase shifts and (b) dynamic moduli of hydrated and dehydrated cartilage. Error bars show standard deviation.

In contrast, phase shifts of hydrated cartilage from a_{medium} and a_{large} were not significantly different from each other (p>0.05). They were not dependent on frequency (p>0.05) (Figure 2-3a). Phase shifts from a_{large} were 9.12 ± 1.29 degrees at 25 Hz and 8.89 ± 2.22 degrees at 100 Hz.

Phase shift of dehydrated cartilage was significantly lower than phase shifts of hydrated cartilage (Figure 2-3a) (p<0.05). The phase shift at the dehydrated state was not dependent on frequency (4.42 ± 0.49 degrees at 5 Hz and 3.41 ± 1.13 degrees at 100 Hz) ($p>0.05$). Phase shift of dehydrated cartilage was approximately 3-7 times lower than that of hydrated cartilage.

Hydrated cartilage tested at a_{small} showed significantly lower dynamic modulus than that tested at a large contact radius (i.e., a_{medium} and a_{large}) ($p<0.05$), but dynamic moduli from a_{medium} and a_{large} were not significantly different (Figure 2-3b) ($p>0.05$). Dynamic modulus from a_{small} increased in a frequency-dependent manner from 7.74 ± 2.86 MPa at 5 Hz to 15.83 ± 5.71 MPa at 100 Hz ($p<0.05$). Dynamic modulus from a_{medium} slightly increased from 34.07 ± 2.68 MPa at 5 Hz to 43.18 ± 3.47 MPa at 100 Hz, and only the modulus at 5 Hz was significantly different than at any other frequencies ($p<0.05$). Dynamic modulus from a_{large} was not frequency-dependent ($p>0.05$), and the values at 25 Hz and 100 Hz were 41.19 ± 11.70 MPa and 47.00 ± 11.33 MPa. Although overall dynamic moduli at a large contact radius (i.e., a_{medium} and a_{large}) were significantly ($p<0.05$) higher than those at a_{small}, the relative increase with frequency was higher at a_{small}.

Dynamic modulus at the dehydrated state was significantly higher than that at the hydrated state (Figure 2-3b) ($p<0.05$). Dynamic modulus of dehydrated cartilage ranged from 1.51 ± 0.33 GPa at 5 Hz to 1.70 ± 0.35 GPa at 100 Hz, and it was not significantly dependent on frequency ($p>0.05$). Dynamic modulus at the dehydrated state was about 120 times and about 40 times higher than the overall dynamic moduli from a_{small} and a large contact radius (i.e., a_{medium} and a_{large}), respectively.

D was determined by fitting normalized force relaxation curves at a_{small} to the master curve (Eq. 2-3 and Eq. 2-4). As a result, D was evaluated to be $(3.89 \pm 1.64) \times 10^{-11}$ m^2/s, and the R-squared value for the curve fitting was 0.97 ± 0.01 (Figure 2-4). Furthermore, f_{poro} was estimated as 0.22 ± 0.09 Hz by substituting the determined D into Eq. 2-5.

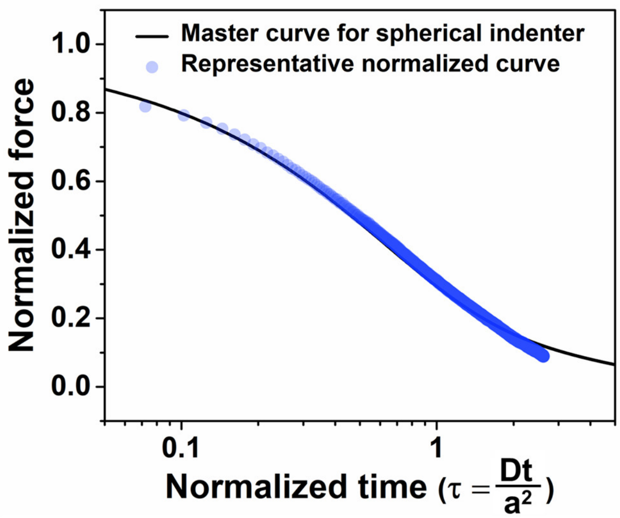

Figure 2-4: Representative of fitting normalized force relaxation to master curve for contact between spherical indenter and half-space poroelastic material [15]. The R-squared values for all of the fits were $\mathbf{0.97 \pm 0.01}$.

Weight and thickness of cartilage dramatically decreased during dehydration (Figure 2-5). The decrease rate of weight was relatively high until about 1.5 hours, gradually slowed down, and became steady after about 4 hours. Weight of dehydrated cartilage at steady state was about 0.25 times that of hydrated cartilage at the beginning. The decrease rate of thickness showed a trend similar to that of weight. It was relatively high in the beginning, and progressively reached steady state. Thickness of dehydrated cartilage at steady state was about 0.3 times that of hydrated cartilage at the beginning. The slight fluctuation of thickness after 4 hours was due to the effect of edge curl on the measurement.

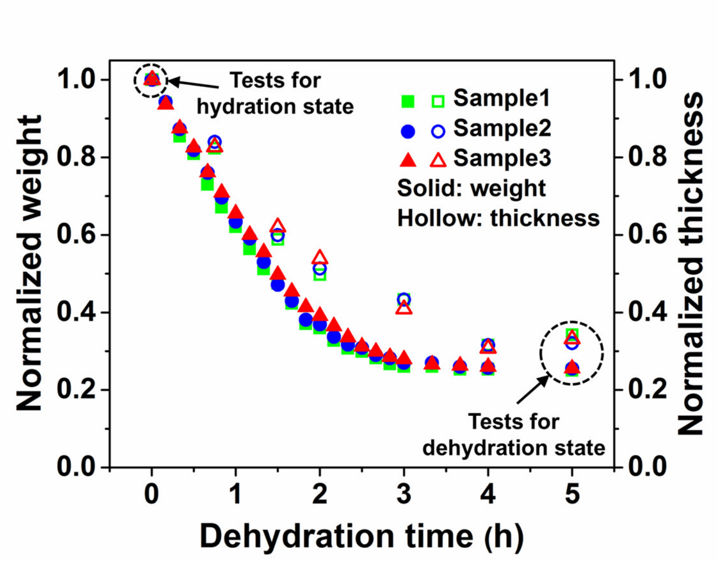

Figure 2-5: Change in weight and thickness of cartilage during dehydration.

2.5. Discussion

Intrinsic viscoelasticity provided baseline of dissipation over the broadband frequency, and poroelasticity additionally increased overall dissipation (Figure 2-3a and Figure 2-6). Phase shifts from a_{small} and large contact radii (i.e., a_{medium} and a_{large}) originate from poroviscoelastic dissipation and intrinsic viscoelastic dominant dissipation, respectively (Figure 2-3a). Therefore, the difference between phase shifts with a_{small} and a_{medium} was from the contribution of poroelasticity-driven dissipation; assuming that poroelastic and viscoelastic time constants are sufficiently different at these contact radii, simple superposition of dissipative effects due to each mechanism is a reliable approximation. The experimentally-measured poroelastic contribution was maximum at 5 Hz in the applied frequency range and a_{small}, which was consistent with a trend estimated from f_{poro} (0.22 ± 0.09 Hz). However, the contribution of poroelasticity-driven dissipation at a specific frequency varies depending on a characteristic length (contact radius) [4,11]. As the contact radius decreases, the curve of poroelasticity-driven phase shift moves toward a high frequency because f_{poro} is inversely proportional to the square of a contact radius (Eq. 2-5) [4,11]. For instance, previous work [4] showed poroelastic peaks of cartilage at higher frequencies (about 11 Hz) with smaller contact radii (about 6 μm) than the current study.

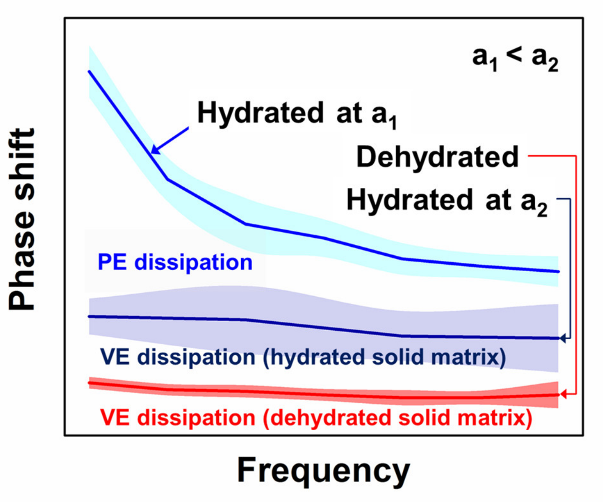

Figure 2-6: Separation of total energy dissipation into poroelastic, PE, and intrinsic viscoelastic dissipation, VE, over frequency range (5 Hz – 100 Hz). This schematic diagram was plotted based on Figure 2-3a. Standard deviation was connected using the modified Bezier curve. Intrinsic viscoelasticity provides baseline of dissipation, and poroelasticity additionally increases overall dissipation. Dehydration decreases intrinsic viscoelastic dissipation.

Hydrated cartilage dissipated energy predominantly via molecular friction and rearrangement of the solid matrix (intrinsic viscoelasticity [4,8]) at large contact radii (i.e., a_{medium} and a_{large}). The independence of phase shift on contact radius showed that phase shifts at a_{medium} and a_{large} were predominantly from intrinsic viscoelasticity (Figure 2-3a). In addition, the steady trend of phase shift over the frequency range (5 Hz – 100 Hz) was consistent with previous studies that report macroscale compression and microscale shear results (about 5-14 degrees [6,7,16]). Since τ_{poro} is proportional to the square of contact radius (Eq. 2-5), poroelastic dissipation is most likely to be suppressed under macroscale compression. Some discrepancies in numerical values could be attributed to various factors: species, age, and test conditions (i.e., full-thickness and induced stress). Consequently, a_{medium} was large enough to restrict interstitial fluid flow within the applied frequency range, and therefore phase shift at a_{medium} was predominantly from intrinsic viscoelasticity. This finding demonstrated that broadband intrinsic properties of cartilage can be measured at microscale characteristic lengths; previous studies were limited to macroscale characteristic lengths.

Hydrated cartilage dissipated energy through poroelasticity (solid-fluid frictional interaction [4,5]) as well as intrinsic viscoelasticity at a_{small}. Significant difference in phase shifts between a_{small} and large contact radii (i.e., a_{medium} and a_{large}) showed additional dissipated energy through poroelasticity at a_{small} (Figure 2-3a). Also, the frequency-dependence of phase shift measured at a_{small} was consistent with the theoretical poroelastic peak, f_{poro} (0.22 ± 0.09 Hz); it increased toward the peak frequency. D (($3.89 \pm 1.64) \times 10^{-11}$ m^2/s), used for the estimation of f_{poro}, was consistent with previous studies that used different measurement methods (1.97×10^{-11} m^2/s [17], 2.30×10^{-11} m^2/s [18], and 8.35×10^{-10} m^2/s [19]); some discrepancies could be due to samples and strain dependency of D [20,21]. However, the overall consistency of values of D indicates that the simplifying assumption of isotropy is reasonable for this study. The gradual decrease of phase shift over about two decades was also consistent with previous studies that reported poroelasticity-driven phase shift of cartilage [4,5]. Therefore, phase shift of cartilage at a_{small} was dominantly from poroelasticity.

Normalizing the frequency with the square of contact radius reiterates the viscoelastic (a_{medium} and a_{large}) and combined poroviscoelatic (a_{small}) dissipation regimes [11]. In the normalized frequency domain, the phase shifts at different contact radii formed united curves (Figure 2-7). Both the phase shift and the normalized frequency range were consistent with previous macroscale tests (about 10 degrees at 6.76×10^{-5} - $5.95\times10^{-5}10^{-3}$ m^2/s [7]). While most data points were along a united curve, the phase shift from a_{medium} at low frequency (f=5Hz, $a^2f= 5.37\times10^{-9}$ m^2/s) deviated from the overall trend. This was likely due to contact radius decreasing poroelastic dissipation, which was previously observed in biological tissues [4,11,22,23]. Combined with the consistency with phase shifts measured at similar frequencies via small magnitude shear loading (about 10 degrees at 0.01, 0.1, and 1 Hz [16]), this suggests predominantly viscoelastic dissipation for a_{medium} at low frequency.

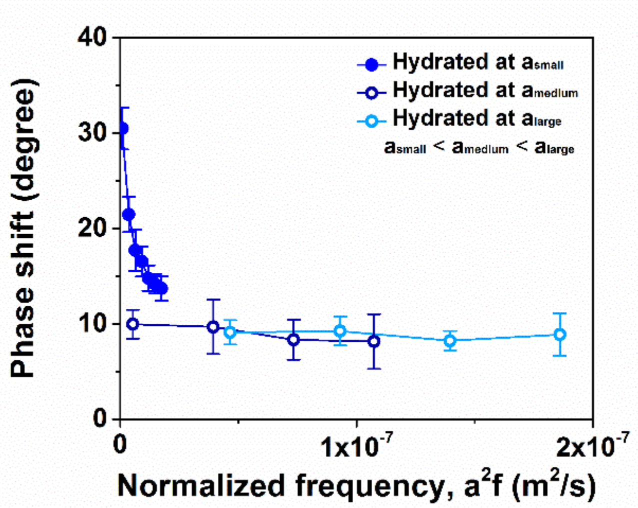

Figure 2-7: Phase shift curves as function of normalized frequency. The frequency was normalized with the squared of contact radius.

Cartilage exhibited superior energy dissipation compared to isotropic poroelastic materials (e.g., gel); the uncoupled dissipation mechanisms provided reasons of the superiority (Figure 2-3a, Figure 2-6). A previous paper reported the analytical solution of phase shift for dynamic indentation on an isotropic poroelastic material, and verified it by performing dynamic testing on gel with a 25 µm diameter tip [11]. The analytical solution shows that the maximum phase shift from the contact of a sphere with a half-space poroelastic material is about 12 degrees at the poroelastic peak frequency. It is much lower than the maximum phase shift of cartilage measured in this current study (30.50 ± 2.19 degrees at 5 Hz). The current finding revealed that intrinsic viscoelasticity of cartilage provided the baseline of about 9 degree phase shift over the frequency range (Figure 2-3a). Even if the contribution of intrinsic viscoelastic dissipation was excluded, the poroelasticity-driven phase shift of cartilage, which was between phase shifts between a_{small} and a_{medium} (approximately 20 degrees at 5 Hz), was still higher than the maximum value of an isotropic porous material (12 degrees) [11]. This could be due to the effect of fiber-reinforced structure [4] and anisotropy [1] of cartilage on poroelasticity-driven dissipation. The anisotropy of collagen fibrils could affect dissipation as they direct fluid flow [24]; the degree of the anisotropy is expected to be relatively minor when considering the sample age (5-6 months old) [25].

Fluid pressurization was likely the driving factor behind the dependence of dynamic modulus on contact radius. The dependence of overall dynamic modulus on contact radius (Figure 2-3b) could be due to the degree of interstitial fluid pressurization over the frequency range, evidenced by the uncoupled dominant mechanisms and previous studies. While poroelasticity was dominant at a_{small}, it was suppressed at large contact radii (i.e., a_{medium} and a_{large}). Poroelasticity is volumetric effect, so this suggests that cartilage deformed isochorically at large contact radii (i.e., a_{medium} and a_{large}). Also, the Peclet number ($\propto \tau_{poro}$ at the same loading rate [26]), a measure of fluid pressurization [26–28], is much higher at a large contact radius (i.e., a_{medium} and a_{large}) compared to a_{small}. Therefore, fluid pressurization at a large contact radius (i.e., a_{medium} and a_{large}) can be inferred to be higher than that at a_{small} in the corresponding frequency (i.e. loading rate) [4,8,26,27]. The higher fluid pressure was likely to cause relatively high tensile strain of nonlinear solid matrix [29], resulting in higher dynamic modulus at a large contact radius (i.e., a_{medium} and a_{large}). The values of dynamic modulus at a large contact radius (i.e., a_{medium} and a_{large}) were consistent with previous studies at macroscale [6,7]. Some discrepancies could be attributed to species and test conditions (i.e., scale and compressive stress). The dependence of self-stiffening of cartilage on contact radius (Figure 2-3b) was likely due to the effect of frequency on fluid pressurization, underpinned by the determined dominant mechanisms and previous studies [4,8]. The self-stiffening is defined here as the ratio of dynamic moduli at 100 Hz and 5 Hz, and a_{small} (about 2.05) exhibited a higher ratio than a_{medium} (about 1.25). Phase shift at a_{small} showed that poroelastic effect decreased toward 100 Hz, resulted from a relative increase of loading rate in the same poroelastic diffusion time [4,8,27]. As a result, interstitial fluid pressure likely increased with frequency, and thus dynamic modulus at a_{small} gradually increased [4,8,27]. Note that a_{small} at 100 Hz was not incompressible because phase shift at a_{small} was higher than that at a_{medium}, indicating some poroelastic effect. In contrast, in the case of a_{medium}, cartilage was virtually incompressible (isochoric deformation) over the frequency range. Consequently, fluid pressurization was relatively steady with frequency, and therefore dynamic modulus was almost constant [8]. It was consistent with steady trends of dynamic moduli at macroscale from previous studies [6,7]. The slight self-stiffening at a_{medium} could be attributed to intrinsic viscoelasticity of solid matrix.

Dehydration dramatically decreased water content and thickness of cartilage (Figure 2-5). Weight of total water in cartilage is about 60 – 85 % of its wet weight and about 30 % of the total water belongs to intrafibrillar space [1–3]. Therefore, 25 % of the initial cartilage weight at the dehydration state indicated that cartilage lost substantial water in extrafibriliar and intrafibriliar spaces. Similar to weight, the considerable decrease in thickness was also due to loss of water in extrafibriliar and intrafibriliar spaces. The dramatic change in water content and thickness by air dehydration were consistent with previous studies (e.g., cartilage [30] and type I collagen [31]).

Such extreme dehydration had a pronounced effect on phase shift and dynamic modulus of cartilage over the frequency range studied (Figure 2-3 and Figure 2-6). Poroelasticity-driven dissipation did not arise due to substantial loss of fluid, evidenced by the disappearance of a poroelastic peak trend in phase shift. A decrease in intrinsic viscoelasticity was most likely due to loss of interfibrillar fluid and increased density of solid matrix (similar to foam materials). This is supported by previous studies on individual collagen fibrils and polymeric structural foams: energy dissipation of Type I collagen fibrils decreased with a progressive dehydration [32] and density of foams influenced on their absorbed energy [33]. This finding suggested that a decreased ability of cartilage to sustain fluid in disease could decrease energy dissipation under dynamic loading conditions *in vivo*. In addition to affecting energy dissipation, dehydration sharply increased dynamic modulus (Figure 2-3b). It was likely due to the compaction of cartilage by dehydration, resulting from collapsed pore space and shrinkage of the solid matrix. It could be inferred from the huge decrease in thickness after dehydration. A previous study on Type 1 collagen fibrils provided evidence on shrinkage of fibrils during dehydration [31]. The increase in dynamic modulus was consistent with previous studies that showed fibrils [31,34] and cartilage [30] became stiffer after dehydration through quasi-static tests. This finding implies that a decreased ability of the solid matrix to maintain fluid due to disease could affect poroelasticity-driven dissipation over the frequency range of interest because increased stiffness of solid matrix decreases volumetric deformation under the same stress level; poroelasticy-driven dissipation originates from solid-fluid frictional interaction, and fluid flow is related to volumetric deformation [35].

It is worthwhile to discuss a few limitations of this study. Although the applied frequency (5-100 Hz) covered most of daily activity-induced frequencies (timescales) [4] (e.g., walking: 1-8Hz [36], running: 4-100 Hz [37], kicking: 4 -11Hz [38], and jumping: 2-100 Hz [39]), a low frequency range (< 5 Hz) was not covered. It was scarified due to limitations in the data acquisition point coupled with the duration for equilibrium. Nevertheless, the trend of phase shift (5-100 Hz) matched well with that inferred from the expected peak at f_{poro}. The testing conditions employed in this study are not the same as vivo conditions (e.g., full-thickness); however, they provided information on isolated properties of cartilage (i.e., superficial zone), which enabled uncoupling poroelastic and intrinsic viscoelastic dissipation. The dehydration process was conducted in ambient conditions under controlled humidity. Although the weight and thickness of cartilage was considerably reduced after 5 hours of dehydration, fully-dry cartilage matrix conditions cannot be ensured as the hydration level of cartilage should equilibrate with the ambient humidity. Fully-dry cartilage matrix could be obtained by controlled drying processes such as freeze-drying [40,41].

In our view, this study provided useful information for cartilage-like dampers [42,43] and showed a possibility that the current approach could be used to investigate early osteoarthritic damage [44]. The uncoupled poroelastic and intrinsic viscoelasticity of cartilage suggested that cartilage-like dampers with efficient and sustained dissipation could be designed by inducing poroelasticity-driven dissipation in addition to intrinsic viscoelasticity-driven dissipation. The current study combined with previous studies [4,42] suggested dissipation of cartilage-like dampers at a specific frequency can be maximized by utilizing the dependence of f_{poro} on a characteristic length and diffusivity. In addition, it was demonstrated that poroelastic and intrinsic viscoelastic-dominant properties of superficial zone can be measured at microscale characteristic lengths. This approach could be useful to investigate early osteoarthritis, initiating from superficial zone [1,44].

2.6. Conclusions

In this study, dissipative properties due to poroelasticity and intrinsic viscoelasticity of cartilage were investigated over physiological loading frequencies. Uncoupling between poroelasticity and intrinsic viscoelasticity was achieved via dependence of poroelastic relaxation on characteristic lengths (contact radii in dynamic indentation tests). The uncoupled dissipation mechanisms provided novel information on origins of efficient and sustained broadband dissipation of cartilage; intrinsic viscoelasticity provides baseline of dissipation, and poroelasticity additionally increases overall dissipation. The confirmation of intrinsic viscoelasticity broke the existing broadband test scale of intrinsic properties, limited to macroscale length, and provided a possibility to measure poroelastic (flow-dependent) and intrinsic viscoelastic (flow-independent) properties of cartilage at similar microscale lengths. The decreased dissipation of cartilage following dehydration highlighted the importance of hydration in both poroelasticity and intrinsic viscoelasticity-related losses. The findings extended the current understanding in dynamic dissipative and mechanical properties of cartilage. Promising aspects of cartilage as efficient and sustained dampers were experimentally confirmed, and the findings could be useful to design them as suggested elsewhere [42,43].

2.7. Acknowledgment

Funding from the National Science Foundation (CMMI-DCSD-1662456) is gratefully acknowledged. The authors are grateful to Shannon K. Walsh and Sunjung Kim for helpful discussions on statistical analysis.

2.8. References

[1] Mow, V. C., Ratcliffe, A., and Robin Poole, A., 1992, “Cartilage and Diarthrodial Joints as Paradigms for Hierarchical Materials and Structures,” Biomaterials, 13(2), pp. 67–97.

[2] Torzilli, P. A., 1985, “Influence of Cartilage Conformation on Its Equilibrium Water Partition,” J. Orthop. Res., 3(4), pp. 473–483.

[3] Maroudas, A., Wachtel, E., Grushko, G., Katz, E. P., and Weinberg, P., 1991, “The Effect of Osmotic and Mechanical Pressures on Water Partitioning in Articular Cartilage,” Biochim. Biophys. Acta BBA - Gen. Subj., 1073(2), pp. 285–294.

[4] Nia, H., Han, L., Li, Y., Ortiz, C., and Grodzinsky, A., 2011, “Poroelasticity of Cartilage at the Nanoscale,” Biophys. J., 101(9), pp. 2304–2313.

[5] Nia, H. T., Bozchalooi, I. S., Li, Y., Han, L., Hung, H. H., Frank, E., Youcef-Toumi, K., Ortiz, C., and Grodzinsky, A., 2013, “High-Bandwidth AFM-Based Rheology Reveals That Cartilage Is Most Sensitive to High Loading Rates at Early Stages of Impairment,” Biophys. J., 104(7), pp. 1529–1537.

[6] Fulcher, G. R., Hukins, D. W., and Shepherd, D. E., 2009, “Viscoelastic Properties of Bovine Articular Cartilage Attached to Subchondral Bone at High Frequencies,” BMC Musculoskelet. Disord., 10, p. 61.

[7] Lawless, B. M., Sadeghi, H., Temple, D. K., Dhaliwal, H., Espino, D. M., and Hukins, D. W. L., 2017, “Viscoelasticity of Articular Cartilage: Analysing the Effect of Induced Stress and the Restraint of Bone in a Dynamic Environment,” J. Mech. Behav. Biomed. Mater., 75, pp. 293–301.

[8] Tavakoli Nia, H., Han, L., Soltani Bozchalooi, I., Roughley, P., Youcef-Toumi, K., Grodzinsky, A. J., and Ortiz, C., 2015, “Aggrecan Nanoscale Solid–Fluid Interactions Are a Primary Determinant of Cartilage Dynamic Mechanical Properties,” ACS Nano, 9(3), pp. 2614–2625.

[9] June, R. K., Ly, S., and Fyhrie, D. P., 2009, “Cartilage Stress-Relaxation Proceeds Slower at Higher Compressive Strains,” Arch. Biochem. Biophys., 483(1), pp. 75–80.

[10] Mak, A. F., 1986, “The Apparent Viscoelastic Behavior of Articular Cartilage—The Contributions From the Intrinsic Matrix Viscoelasticity and Interstitial Fluid Flows,” J. Biomech. Eng., 108(2), pp. 123–130.

[11] Lai, Y., and Hu, Y., 2017, “Unified Solution for Poroelastic Oscillation Indentation on Gels for Spherical, Conical and Cylindrical Indenters,” Soft Matter, 13(4), pp. 852–861.

[12] Henak, C. R., Ross, K. A., Bonnevie, E. D., Fortier, L. A., Cohen, I., Kennedy, J. G., and Bonassar, L. J., 2016, “Human Talar and Femoral Cartilage Have Distinct Mechanical Properties near the Articular Surface,” J. Biomech.

[13] Hysitron, I., 2014, “TriboIndenter NanoDMA^{TM} User Manual.”

[14] Hertz, H., 1881, “On the Contact of Elastic Solids,” J. Reine Angew. Math., 92, pp. 156–171.

[15] Hu, Y., Zhao, X., Vlassak, J. J., and Suo, Z., 2010, “Using Indentation to Characterize the Poroelasticity of Gels,” Appl. Phys. Lett., 96(12), p. 121904.

[16] Buckley, M. R., Bonassar, L. J., and Cohen, I., 2013, “Localization of Viscous Behavior and Shear Energy Dissipation in Articular Cartilage Under Dynamic Shear Loading,” J. Biomech. Eng., 135(3), pp. 031002-031002–9.

[17] Lee, J. I., Sato, M., Ushida, K., and Mochida, J., 2011, “Measurement of Diffusion in Articular Cartilage Using Fluorescence Correlation Spectroscopy,” BMC Biotechnol., 11, p. 19.

[18] Leddy, H. A., Christensen, S. E., and Guilak, F., 2008, “Microscale Diffusion Properties of the Cartilage Pericellular Matrix Measured Using 3D Scanning Microphotolysis,” J. Biomech. Eng., 130(6), pp. 061002-061002–8.

[19] Aoki, T., Watanabe, A., Nitta, N., Numano, T., Fukushi, M., and Niitsu, M., 2012, “Correlation between Apparent Diffusion Coefficient and Viscoelasticity of Articular Cartilage in a Porcine Model,” Skeletal Radiol., 41(9), pp. 1087–1092.

[20] Lai, W. M., Mow, V. C., and Roth, V., 1981, “Effects of Nonlinear Strain-Dependent Permeability and Rate of Compression on the Stress Behavior of Articular Cartilage,” J. Biomech. Eng., 103(2), pp. 61–66.

[21] Greene, G. W., Zappone, B., Söderman, O., Topgaard, D., Rata, G., Zeng, H., and Israelachvili, J. N., 2010, “Anisotropic Dynamic Changes in the Pore Network Structure, Fluid Diffusion and Fluid Flow in Articular Cartilage under Compression,” Biomaterials, 31(12), pp. 3117–3128.

[22] Connizzo, B. K., and Grodzinsky, A. J., 2017, “Tendon Exhibits Complex Poroelastic Behavior at the Nanoscale as Revealed by High-Frequency AFM-Based Rheology,” J. Biomech., 54, pp. 11–18.

[23] Oftadeh, R., Connizzo, B. K., Nia, H. T., Ortiz, C., and Grodzinsky, A. J., 2018, “Biological Connective Tissues Exhibit Viscoelastic and Poroelastic Behavior at Different Frequency Regimes: Application to Tendon and Skin Biophysics,” Acta Biomater., 70, pp. 249–259.

[24] Federico, S., and Herzog, W., 2008, “On the Anisotropy and Inhomogeneity of Permeability in Articular Cartilage,” Biomech. Model. Mechanobiol., 7(5), pp. 367–378.

[25] Gannon, A. R., Nagel, T., Bell, A. P., Avery, N. C., and Kelly, D. J., 2015, “Postnatal Changes to the Mechanical Properties of Articular Cartilage Are Driven by the Evolution of Its Collagen Network,” Eur. Cell. Mater., 29, pp. 105–121; discussion 121-123.

[26] Quinn, T. M., Allen, R. G., Schalet, B. J., Perumbuli, P., and Hunziker, E. B., 2001, “Matrix and Cell Injury Due to Sub-Impact Loading of Adult Bovine Articular Cartilage Explants: Effects of Strain Rate and Peak Stress,” J. Orthop. Res., 19(2), pp. 242–249.

[27] Caligaris, M., and Ateshian, G. A., 2008, “Effects of Sustained Interstitial Fluid Pressurization under Migrating Contact Area, and Boundary Lubrication by Synovial Fluid, on Cartilage Friction,” Osteoarthr. Cartil. OARS Osteoarthr. Res. Soc., 16(10), pp. 1220–1227.

[28] Bonnevie, E. D., Baro, V. J., Wang, L., and Burris, D. L., 2012, “Fluid Load Support during Localized Indentation of Cartilage with a Spherical Probe,” J. Biomech., 45(6), pp. 1036–1041.

[29] Cohen, B., Lai, W. M., and Mow, V. C., 1998, “A Transversely Isotropic Biphasic Model for Unconfined Compression of Growth Plate and Chondroepiphysis,” J. Biomech. Eng., 120(4), pp. 491–496.

[30] Boettcher, K., Kienle, S., Nachtsheim, J., Burgkart, R., Hugel, T., and Lieleg, O., 2016, “The Structure and Mechanical Properties of Articular Cartilage Are Highly Resilient towards Transient Dehydration,” Acta Biomater., 29, pp. 180–187.

[31] Andriotis, O. G., Chang, S. W., Vanleene, M., Howarth, P. H., Davies, D. E., Shefelbine, S. J., Buehler, M. J., and Thurner, P. J., 2015, “Structure–Mechanics Relationships of Collagen Fibrils in the Osteogenesis Imperfecta Mouse Model,” J. R. Soc. Interface, 12(111), p. 20150701.

[32] Uhlig, M. R., and Magerle, R., 2017, “Unraveling Capillary Interaction and Viscoelastic Response in Atomic Force Microscopy of Hydrated Collagen Fibrils,” Nanoscale, 9(3), pp. 1244–1256.

[33] Avalle, M., Belingardi, G., and Montanini, R., 2001, “Characterization of Polymeric Structural Foams under Compressive Impact Loading by Means of Energy-Absorption Diagram,” Int. J. Impact Eng., 25(5), pp. 455–472.

[34] Wenger, M. P. E., Bozec, L., Horton, M. A., and Mesquida, P., 2007, “Mechanical Properties of Collagen Fibrils,” Biophys. J., 93(4), pp. 1255–1263.

[35] Lakes, P. R., 2009, *Viscoelastic Materials*, Cambridge University Press, Cambridge ; New York.

[36] Cross, R., 1999, “Standing, Walking, Running, and Jumping on a Force Plate,” Am. J. Phys., 67(4), p. 304.

[37] Dickinson, J. A., Cook, S. D., and Leinhardt, T. M., 1985, “The Measurement of Shock Waves Following Heel Strike While Running,” J. Biomech., 18(6), pp. 415–422.

[38] Tanaka, Y., Shiokawa, M., Yamashita, H., and Tsuji, T., 2006, “Manipulability Analysis of Kicking Motion in Soccer Based on Human Physical Properties,” *2006 IEEE International Conference on Systems, Man and Cybernetics*, pp. 68–73.

[39] Richards, D. P., Ajemian, S. V., Wiley, J. P., and Zernicke, R. F., 1996, “Knee Joint Dynamics Predict Patellar Tendinitis in Elite Volleyball Players,” Am. J. Sports Med., 24(5), pp. 676–683.

[40] Taylor, A. C., 1945, “The Rates of Freezing, Drying and Rehydration of Nerves,” J. Cell. Comp. Physiol., 25(3), pp. 161–173.

[41] Polak, R., and Pitombo, R. N. M., 2011, “Care during Freeze-Drying of Bovine Pericardium Tissue to Be Used as a Biomaterial: A Comparative Study,” Cryobiology, 63(2), pp. 61–66.

[42] Liu, L., Usta, A. D., and Eriten, M., 2017, “A Broadband Damper Design Inspired by Cartilage-like Relaxation Mechanisms,” J. Sound Vib., 406(Supplement C), pp. 1–14.

[43] Boz, U., and Eriten, M., 2018, “A Numerical Investigation of Damping in Fuzzy Oscillators with Poroelastic Coating Attached to a Host Structure,” J. Sound Vib., 417, pp. 277–293.

[44] Hollander, A. P., Pidoux, I., Reiner, A., Rorabeck, C., Bourne, R., and Poole, A. R., 1995, “Damage to Type II Collagen in Aging and Osteoarthritis Starts at the Articular Surface, Originates around Chondrocytes, and Extends into the Cartilage with Progressive Degeneration.,” J. Clin. Invest., 96(6), pp. 2859–2869.

Chapter 3 Macroscopic dissipation as function of matrix integrity*

Guebum Han, Utku Boz, Melih Eriten, and Corinne R. Henak

*(*Prepared for submission to a journal)*

3.1. Abstract

High-frequency material behavior of cartilage is not widely understood, despite the range of contact lengths and frequencies experienced *in vivo*. For example, high-frequency loading occurs during traumatic impact and heel strike, making high-frequency behavior relevant in the context of structural failure. Therefore, this study examined macroscopic dissipative and mechanical responses of intact and glycosaminoglycan (GAG)-depleted cartilage under previously unexplored high-frequency loading. These dynamic responses were complemented with evaluation of quasi-static responses. A custom dynamic mechanical analyzer was used to obtain dynamic responses, and stress relaxation testing was performed to obtain the quasi-static responses. Under high-frequency loading, cartilage energy dissipation increased with GAG depletion and decreased with strain, while showing opposite trends in dynamic modulus. Similarly, under quasi-static loading, compressive strength and relaxation time constant of cartilage decreased with GAG depletion. In combination with previous research, these results suggest that the increased energy dissipation of GAG-depleted cartilage at high frequencies was dominantly due to increased diffusivity, altering the contribution of poroelastic dissipation. These findings broaden fundamental properties of cartilage as a function of solid matrix integrity in an unprecedented loading regime. They also provide a foundation for analyzing energy dissipation associated with cartilage failure induced by traumatic impact.

Keywords Energy dissipation; glycosaminoglycan; osteoarthritis; high-frequency loading; quasi-static loading

3.2. Introduction

Articular cartilage is a load-bearing and dissipative material that cushions the ends of bones in diarthrodial joints and protects against load-induced damage. Cartilage solid matrix is made of proteoglycans (PGs) with sulfated glycosaminoglycan (GAG) side chains (4-7% of wet weight [1]) embedded in a dense collagen fibril matrix (15-22% of wet weight [1]). While collagen fibrils under tension maintain cartilage integrity [2–5], negatively charged GAGs provide positive swelling force and thus compressive resistance through osmotic pressure and repulsive interactions between charge groups [1,6]. The largest component of cartilage is fluid (about 60-85% of wet weight), which swells the solid matrix and pore space [1,7,8].

Dissipative and mechanical responses of cartilage arise due to poroelastic (PE) and intrinsic viscoelastic (VE) relaxations [9–13]. PE relaxation is caused by drag due to stress-induced pore fluid diffusion, resulting in energy dissipation via fluid-solid frictional interaction [10,14,15]. PE relaxation time depends on a characteristic diffusion length and diffusivity [9,10,16–18]. Intrinsic VE relaxation is induced by interactions and rearrangement of solid matrix macromolecules [15,19,20]. Therefore, VE relaxation time is length- and diffusion-independent at the continuum level [9,17,20]. PE and VE relaxation mechanisms play an important role in dissipative capacity and failure of cartilage [10,14,18,21–24].

Although dissipative and mechanical responses of cartilage at microscale lengths have been explored up to high frequencies as a function of the solid matrix integrity, they are only partially understood at macroscopic length scales. At the microscale, GAG-depleted cartilage has higher permeability due to increased pore size, resulting in lower dynamic modulus and a shift in an increased peak frequency of PE dissipation in the 1-10 kHz range [18]. In the 5-100 Hz range, VE dissipation provides a baseline for dissipation, while PE dissipation increases overall dissipation at relatively small length scales [9]. Under quasi-static loading at microscopic length scales, elastic moduli of GAG-depleted cartilage were much lower than those of intact cartilage across the full-thickness sample, but permeability showed an opposite trend [25]. These previous studies provide dissipative and mechanical responses of cartilage at microscale lengths across the frequency contents involved while walking (1-8 Hz), jumping (2-100 Hz), and running (4-100 Hz), occurring with heel strike, and during traumatic impact (≥200 Hz) [18]; the frequency ranges of walking, running, and jumping were not verified by independently measuring loading applied to cartilage and thus might be overestimated as the loading is transmitted via soft dissipative tissues such as tendon. However, cartilage responses at macroscale lengths (≥ 2 mm) have only been partially explored in a relatively low frequency range. This gap is important because *in vivo* contact occurs at the macroscale [26,27] and includes high-frequency loading during traumatic impact and heel strike. At macroscale lengths, storage and loss moduli of intact cartilage gradually reaches constant values at around 15 Hz and maintains them up to 92 Hz, and higher applied stresses decrease phase shift [22,24]. Matrix depletion decreases modulus and increases phase shift under shear at 0.1 Hz and compressive loading up to 40 Hz [28,29]. Currently, macroscopic dissipative and mechanical responses of cartilage were not investigated under high-frequency loading (≥ about 95 Hz) as a function of strain and matrix depletion.

The aim of this study is to fill this gap by examining the effects of solid matrix integrity and strain on dissipative and mechanical responses of cartilage up to 300 Hz in order to cover previously unexplored trauma scenarios under macroscopic contact lengths.

3.3. Methods

3.3.1. Sample Preparation: Intact cartilage

Patellae from eight porcine joints were harvested from a local abattoir (8 animals, 5-6 months old, sex unknown and assumed random). A total of 16 cylindrical cores with a diameter of 4 mm were obtained using a biopsy punch and a scalpel (two cylindrical cores per animal). A microtome was used to remove subchondral bone and achieve a deep surface parallel to the articular surface. Eight of the total 16 cores were used to measure dynamic responses of intact and GAG-depleted cartilage, and the others were used to measure the quasi-static responses (Figure 3-1). Cartilage samples were kept hydrated during the preparation process in Dulbecco's phosphate-buffered saline (DPBS) with protease inhibitor (PI).

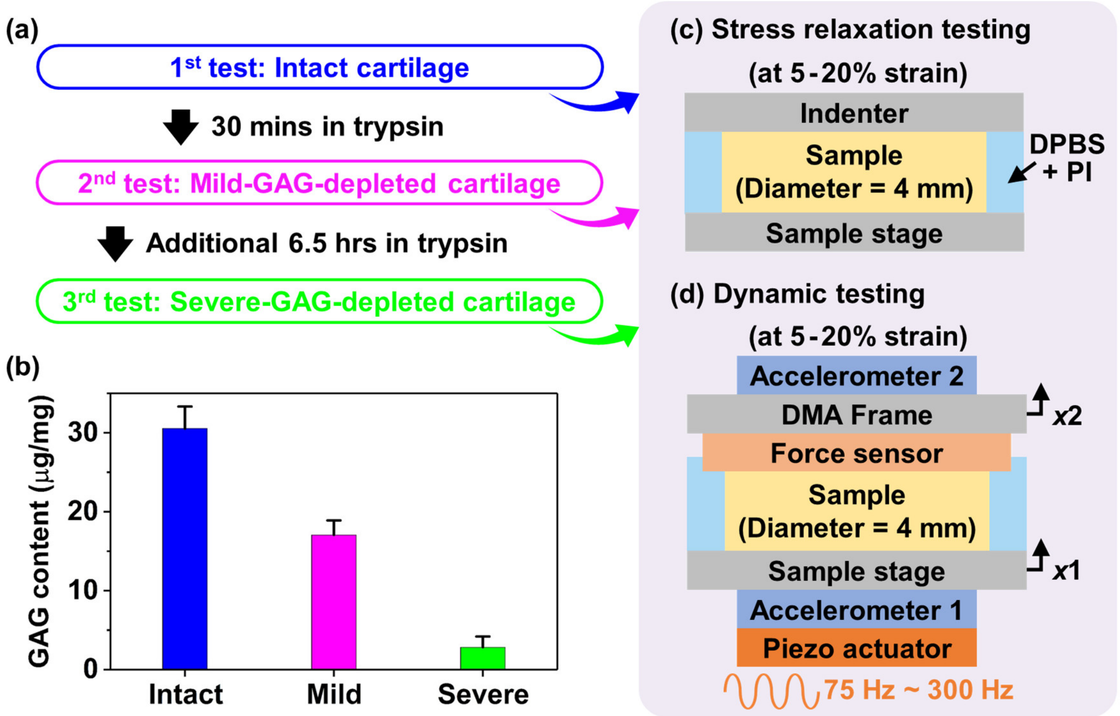

Figure 3-1: (a) Overview of experiments. (b) GAG contents of intact and GAG-depleted cartilage were quantified via the DMMB assay. Schematic diagrams of (c) stress relaxation and (d) dynamic testing setups (not drawn to scale).

3.3.2. Quasi-static testing

Quasi-static responses of intact and GAG-depleted cartilage were examined by measuring stress relaxation responses under unconfined compression at four different strain levels (Figure 3-1a-c). Tests were conducted on a 3230-AT Series III test instrument (TA Instruments, New Castle, DE) with a 6 mm diameter flat glass indenter. Intact cartilage was attached to a stage, compressed up to 5% strain with a 0.1 s^{-1} strain rate, and relaxed for 11 minutes. Additional steps of 5% strain and holding period were repeatedly applied up to 20% strain. After testing intact cartilage, mild-GAG-depletion was induced via a 30 minute incubation period in 0.25% trypsin at 37°C, and the test protocol used for intact cartilage was conducted. Severe-GAG-depletion was then induced via an additional 6.5 hour incubation in 0.25% trypsin at 37°C, and the testing was repeated. Trypsin selectively digests GAG without affecting a collagen fibril matrix [28,30]. GAG contents after trypsin treatments were estimated from pilot samples subjected to a dimethylmethylene blue (DMMB) assay (intact: 32.03±5.32 μg/mg, PG depletion for 1 hour: 17.42±4.83 μg/mg, and PG depletion for 6 hours: 8.80±2.15 μg/mg) (Figure 3-1b).

Stress relaxation responses were used to quantify peak stresses, equilibrium moduli, and relaxation times of intact and GAG-depleted cartilage. First Piola-Kirchhoff peak stress for each strain level was calculated by dividing a peak load (unrelaxed state) with reference configuration area, A (= πr^2 mm^2 = 12.57 mm^2). Equilibrium stress was calculated by dividing equilibrium load (relaxed state) by A. Equilibrium load for each strain was defined as the load response after 10 minutes of relaxation (Figure 3-2a) because there was virtually no further relaxation; load relaxation between 10 minutes and 11 minutes was less than 0.08 % of total relaxation defined as from peak load to equilibrium load for each strain. A linear function was fitted to average equilibrium stresses as a function of strain, and its slope represented equilibrium modulus of cartilage. Relaxation time was defined as the time required to relax 90 % of the total relaxation.

3.3.3. Dynamic testing

Microscopic dynamic responses of intact and GAG-depleted cartilage under high-frequency loading were investigated by measuring phase shift and dynamic modulus using a dynamic mechanical analyzer (DMA) (Figure 3-1a,b and d). Intact cartilage was compressed to 5% strain and relaxed for 10 minutes to reach equilibrium (relaxed state). Then, a frequency sweep from 75 Hz to 300 Hz with a small oscillation (about 650 nm) was applied to a sample stage using a piezo actuator (PI P250.20, PI, Auburn, MA). This dynamic testing was repeated at 10, 15, and 20% strain, with strain levels matched to the quasi-static testing. Acceleration of the sample stage and DMA frame induced by the piezo actuator were measured with two accelerometers (PCB333B30, PI, Auburn, MA) (Figure 3-1d). Displacements $x1$ for the sample stage and $x2$ for the DMA frame, were obtained from the double integration of measured acceleration. The force response during the frequency sweep was measured by a dynamic force sensor (PCB208C01, PI, Auburn, MA). The sampling frequency for acceleration and force was 5 kHz. Using these measured responses, the complex dynamic stiffness, $K(\omega)$, was obtained through the frequency domain analysis as follows:

$$K(\omega) = \frac{F(\omega)}{X1(\omega) - X2(\omega)} \tag{3-1}$$

where $F(\omega)$ is the force response and $X1(\omega)$ and $X2(\omega)$ are the displacements of the sample stage and DMA frame, respectively, in the frequency domain. Then, the complex dynamic modulus, $E(\omega)$, was calculated as follows:

$$E(\omega) = \frac{K(\omega)l_c}{A} \tag{3-2}$$

where l_c is the thickness of cartilage at each stain level and A is the reference configuration contact area between the force sensor and cartilage. As the diameter of the force sensor was larger than that of cartilage, A was equal to the area of articular surface. The magnitude, $|E(\omega)|$, and phase, $\angle E(\omega)$ provide the dynamic modulus and phase shift of intact cartilage, respectively. Following intact cartilage, mild-GAG-depleted and severe-GAG-depleted cartilage were tested using the same test protocol in consecutive order. GAG-depleted samples were prepared in the same way as those used for the quasi-static testing.

3.3.4. Statistical Analysis

Data were not normally distributed and were therefore subjected to nonparametric analysis. A two-way aligned rank transformation analysis of variance (ART ANOVA) was used to assess the effects of both GAG depletion and strain on peak stress, equilibrium stress, relaxation time, phase shift and dynamic modulus, as well as the effects of frequency on phase shift and dynamic modulus.

3.4. Results

Quasi-static peak stresses, equilibrium stresses, and relaxation times of cartilage increased with strain and decreased with GAG depletion (Figure 3-2a). Peak stresses of intact cartilage depended on GAG depletion ($p < 2.22 \times 10^{-16}$), and the values at 5% and 20% strain were 2.28 times and 2.37 times larger than those of severe-GAG-depleted cartilage, respectively (Figure 3-2b). Equilibrium stresses of cartilage decreased with GAG depletion ($p < 2.22 \times 10^{-16}$) and increased with strain ($p < 2.22 \times 10^{-16}$) (Figure 3-2c). Intact cartilage at 5% and 20% strain exhibited 25.05 times and 17.33 times larger equilibrium stresses than severe-GAG-depleted cartilage, respectively.

Equilibrium stresses of intact and severe-GAG-depleted cartilage at 20% strain were 3.87 times and 5.58 times higher than those at 5% strain, respectively. From the slopes of the linear fits (Figure 3-2c), equilibrium moduli of intact, mild-GAG-depleted, and severe-GAG-depleted cartilage were 0.89 MPa ($R^2 > 0.99$), 0.34 MPa ($R^2 = 0.94$), and 0.05 MPa ($R^2 = 0.97$), respectively. Relaxation times of cartilage reduced with GAG-depletion ($p < 2.22 \times 10^{-16}$) and increased with strain ($p = 2.55 \times 10^{-11}$) (Figure 3-2d). Severe-GAG-depleted cartilage at 5% and 20% strain relaxed 6.74 times and 7.28 times faster than intact cartilage. Relaxation times of intact and severe-GAG-depleted cartilage from 5% strain to 20% strain increased 1.8 times and 1.66 times, respectively.

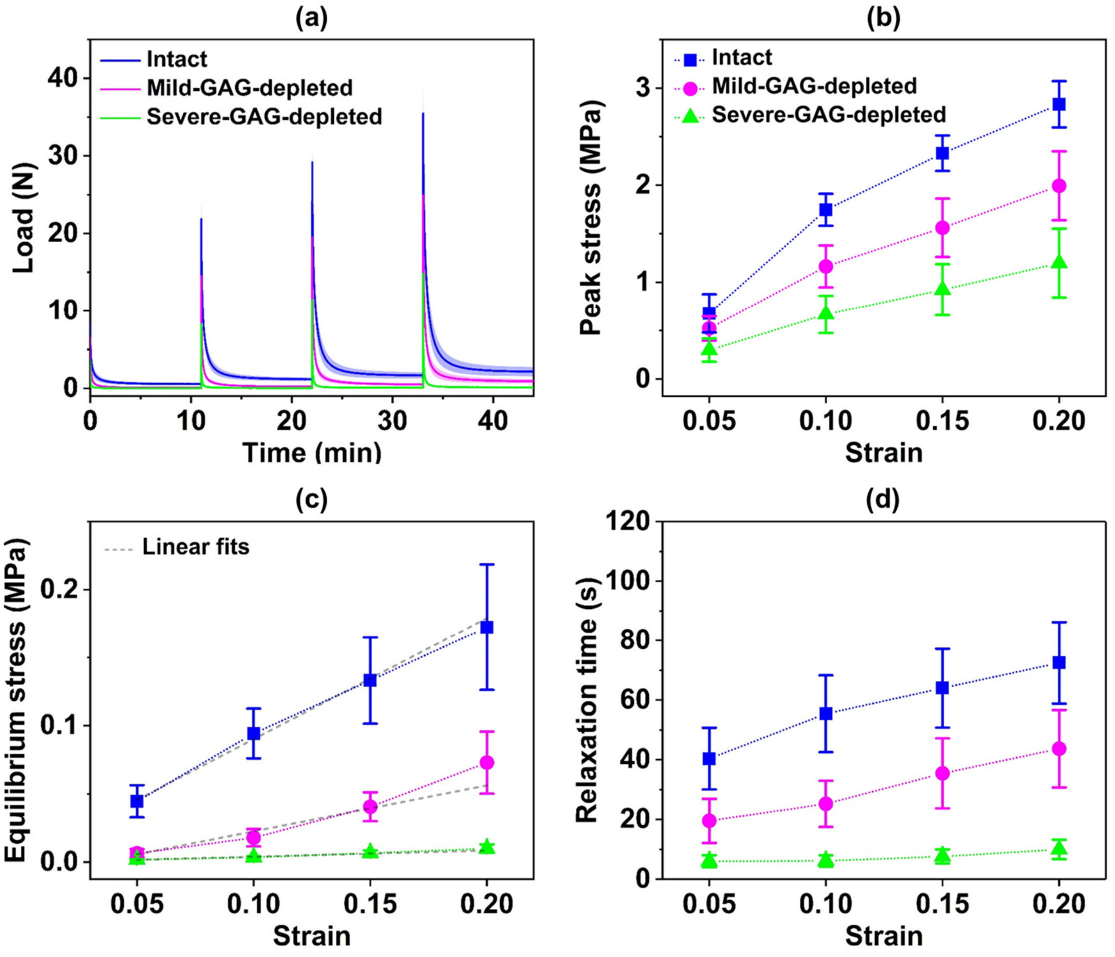

Figure 3-2: Results of quasi-static testing on intact and GAG-depleted cartilage: (a) load relaxation responses, (b) peak stresses, (c) equilibrium streeses, and (d) relaxation times.

High-frequency phase shifts and dynamic moduli of cartilage depended on GAG-depletion and strain (Figure 3-3). Phase shifts of cartilage increased with GAG depletion ($p < 2.22 \times 10^{-16}$) and decreased with strain ($p < 2 \times 10^{-16}$). For example, at 200 Hz under 5% strain, phase shifts increased from about 7.37 degrees to about 12.91 degrees after inducing severe-GAG-depletion. Phase shifts at 200 Hz decreased about 1.5 degrees from 5% strain to 20% strain for intact cartilage, and this decreasing trend was also observed in mild- and severe-GAG-depleted cartilage. Phase shifts of intact and GAG-depleted cartilage were statistically rate-dependent in the high frequency range of interest ($p = 1 \times 10^{-9}$), but the numerical values only increased about one degree from 75 Hz to 300 Hz. In contrast to trends in phase shifts, dynamic moduli of cartilage decreased with GAG depletion ($p < 2 \times 10^{-16}$) and increased with strain ($p < 2 \times 10^{-16}$). For instance, dynamic moduli of intact cartilage at 5% strain at 200 Hz (32.79 MPa) were 2.6 times larger than those of severe-GAG-depleted cartilage at 5% strain (12.49 MPa). From 5% strain to 20% strain, dynamic moduli of intact and severe-GAG-depleted cartilage increased about 1.35 times and about 1.48 times, respectively.

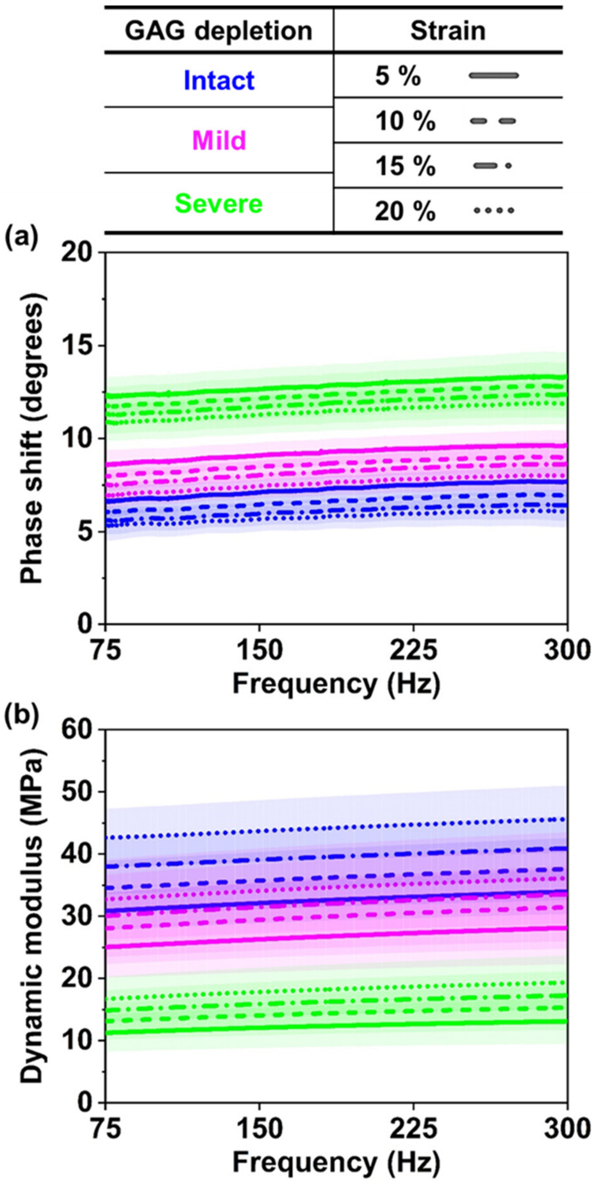

Figure 3-3: (a) Phase shifts and (b) dynamic moduli of intact and GAG-depleted cartilage at 75-300 Hz.

3.5. Discussion

Macroscopic energy dissipation of intact cartilage stems from intrinsic VE dissipation under high-frequency loading. Cartilage undergoes nearly isochoric deformation with restricted fluid flow when PE relaxation time constant [17] is sufficiently larger than the inverse of the induced strain rate [31]. PE relaxation time is proportional to the square of a characteristic length, but inversely proportional to diffusivity. A previous study with dynamic testing at multiple contact radii showed that energy dissipation of intact cartilage at a contact radius of about 40 μm was dominated by intrinsic VE dissipation under oscillatory loading (5-100 Hz with small amplitude of about 1.25 nm) [9]. Thus, under the current conditions with a larger contact radius, amplitude, and frequency range, intact cartilage likely behaved as a nearly incompressible solid and dominantly dissipated energy through intrinsic VE. Further, the measured phase shift (about 7 degrees at 5 % strain) was consistent with that of intrinsic VE dissipation reported in previous work (about 8 degrees at 0.8 % representative strain) in the overlapped frequency range (75 - 100 Hz) [9]; samples used for both studies had the same age and species and were also harvested from the same local abattoir. Strain- and frequency-dependent phase shift of intact cartilage were consistent with macroscopic VE properties reported in previous studies (1-92 Hz) [22,24]; some minor discrepancies in phase shift were likely due to species, age, and test conditions.

GAG depletion enhanced energy dissipation of cartilage under high-frequency loading. GAG-depleted cartilage exhibited higher phase shift than intact cartilage, showing that the loss of GAG content increases energy dissipation (Figure 3-3a). As GAG depletion increases diffusivity [18,25] without affecting a collagen fibril matrix [28,30], the difference in phase shifts of intact and GAG-depleted cartilage was likely due to altered PE dissipation. A sharp decrease in relaxation time after GAG depletion (Figure 3-2d) also suggests an increase in diffusivity. These results imply that osteoarthritis, which includes GAG loss, could increase energy dissipation of cartilage under high-frequency loading.

The degeneration of the solid matrix decreased the resistance of cartilage to being deformed under relatively fast dynamic and quasi-static loading. Dynamic modulus of GAG-depleted cartilage was smaller than that of intact cartilage (Figure 3-3b). This suggests that GAG-depleted cartilage undergoes large deformation under the same pressure generated by high-frequency loading. The decreased resistance could be attributed to relatively decreased lateral expansion of cartilage (i.e., less volumetric change) due to the increased diffusivity after GAG depletion, resulting in a decrease in tensile strain of collagen fibrils [2,9,32]. In addition, a sharp decrease in equilibrium modulus as a function of the solid matrix integrity showed that GAG-depleted cartilage cannot resist quasi-static compression as much as intact cartilage (Figure 3-2c). This was likely because the loss of negatively charged GAGs decreased osmotic pressure and repulsive force between charge groups, as shown in previous studies [1,3,25,33]. The effects of the GAG loss on moduli were much larger under quasi-static loading than high-frequency loading. These findings suggest that cartilage could gradually lose the ability to resist dynamic and quasi-static loading at early stages of osteoarthritis.

This study has a few limitations. The test conditions do not exactly represent *in vivo* conditions; however, DMA and stress relaxation tests provided dissipative and mechanical properties of cartilage at a macroscopic length scale, comparable to contact lengths in the native joints *in vivo* [26,27], as a function of the solid matrix integrity. Osteoarthritis-like cartilage damage was simulated by depleting GAGs through enzymatic treatments, and therefore these findings do not represent osteoarthritis occurring with degeneration of other solid matrix components such as collagen fibrils.

3.6. Conclusions

This study investigated dissipative and mechanical responses of intact and osteoarthritis-like cartilage at a macroscopic length in a previously unexplored high frequency range. Different degrees of GAG depletion were induced via trypsin enzymatic digestion of cartilage. Under high-frequency loading representing traumatic impact and heel strike, energy dissipation of cartilage increased with the degeneration of the solid matrix and decreased with strain. In addition, the resistance of cartilage to being deformed decreased with the degree of GAG depletion. Under quasi-static loading representing human beings rest, GAG-depleted cartilage relaxed much faster and lost compressive strength in equilibrium in comparison to intact cartilage. Sharply decreased relaxation times after the GAG depletion were thought to be mainly due to an increase diffusivity, suggesting an increase in dissipation of GAG-depleted cartilage in the high frequency of interest stemmed from altered PE dissipation. These dissipative and mechanical properties measured at a contact length comparable to the native joints *in vivo* filled the knowledge gaps about dissipative and mechanical properties of intact and osteoarthritis-like cartilage in an unprecedented high frequency range. In particular, they lay the foundation for interpreting energy dissipation associated with cartilage failure as a function of the solid matrix integrity under traumatic injury and high-rate physiological loading.

3.7. Acknowledgment

Funding from the National Science Foundation (CMMI-DCSD-1662456) is gratefully acknowledged. We are grateful to Shannon K. Walsh for helpful discussions on statistical analysis.

3.8. References

[1] Mow, V. C., Ratcliffe, A., and Robin Poole, A., 1992, “Cartilage and Diarthrodial Joints as Paradigms for Hierarchical Materials and Structures,” Biomaterials, 13(2), pp. 67–97.

[2] Andriotis, O. G., Desissaire, S., and Thurner, P. J., 2018, “Collagen Fibrils: Nature’s Highly Tunable Nonlinear Springs,” ACS Nano, 12(4), pp. 3671–3680.

[3] Eisenberg, S. R., and Grodzinsky, A. J., 1985, “Swelling of Articular Cartilage and Other Connective Tissues: Electromechanochemical Forces,” J. Orthop. Res., 3(2), pp. 148–159.

[4] Kempson, G. E., Freeman, M. a. R., and Swanson, S. a. V., 1968, “Tensile Properties of Articular Cartilage,” Nature, 220(5172), pp. 1127–1128.

[5] Soulhat, J., Buschmann, M. D., and Shirazi-Adl, A., 1999, “A Fibril-Network-Reinforced Biphasic Model of Cartilage in Unconfined Compression,” J. Biomech. Eng., 121(3), pp. 340–347.

[6] Han, E., Chen, S. S., Klisch, S. M., and Sah, R. L., 2011, “Contribution of Proteoglycan Osmotic Swelling Pressure to the Compressive Properties of Articular Cartilage,” Biophys. J., 101(4), pp. 916–924.

[7] Maroudas, A., Wachtel, E., Grushko, G., Katz, E. P., and Weinberg, P., 1991, “The Effect of Osmotic and Mechanical Pressures on Water Partitioning in Articular Cartilage,” Biochim. Biophys. Acta BBA - Gen. Subj., 1073(2), pp. 285–294.

[8] Torzilli, P. A., 1985, “Influence of Cartilage Conformation on Its Equilibrium Water Partition,” J. Orthop. Res., 3(4), pp. 473–483.

[9] Han, G., Hess, C., Eriten, M., and Henak, C. R., 2018, “Uncoupled Poroelastic and Intrinsic Viscoelastic Dissipation in Cartilage,” J. Mech. Behav. Biomed. Mater., 84, pp. 28–34.

[10] Nia, H., Han, L., Li, Y., Ortiz, C., and Grodzinsky, A., 2011, “Poroelasticity of Cartilage at the Nanoscale,” Biophys. J., 101(9), pp. 2304–2313.

[11] Akizuki, S., Mow, V. C., Müller, F., Pita, J. C., Howell, D. S., and Manicourt, D. H., 1986, “Tensile Properties of Human Knee Joint Cartilage: I. Influence of Ionic Conditions, Weight Bearing, and Fibrillation on the Tensile Modulus,” J. Orthop. Res., 4(4), pp. 379–392.

[12] Matthews, L. S., Sonstegard, D. A., and Henke, J. A., 1977, “Load Bearing Characteristics of the Patello-Femoral Joint,” Acta Orthop. Scand., 48(5), pp. 511–516.

[13] Boettcher, K., Kienle, S., Nachtsheim, J., Burgkart, R., Hugel, T., and Lieleg, O., 2016, “The Structure and Mechanical Properties of Articular Cartilage Are Highly Resilient towards Transient Dehydration,” Acta Biomater., 29, pp. 180–187.

[14] Nia, H., Han, L., Soltani Bozchalooi, I., Roughley, P., Youcef-Toumi, K., Grodzinsky, A. J., and Ortiz, C., 2015, "Aggrecan Nanoscale Solid–Fluid Interactions Are a Primary Determinant of Cartilage Dynamic Mechanical Properties," ACS Nano, 9(3), pp. 2614–2625.

[15] Lakes, P. R., 2009, *Viscoelastic Materials*, Cambridge University Press, Cambridge ; New York.

[16] DiDomenico, C. D., Lintz, M., and Bonassar, L. J., 2018, "Molecular Transport in Articular Cartilage — What Have We Learned from the Past 50 Years?," Nat. Rev. Rheumatol., 14(7), p. 393.

[17] Lai, Y., and Hu, Y., 2017, "Unified Solution for Poroelastic Oscillation Indentation on Gels for Spherical, Conical and Cylindrical Indenters," Soft Matter, 13(4), pp. 852–861.

[18] Nia, H., Bozchalooi, I. S., Li, Y., Han, L., Hung, H.-H., Frank, E., Youcef-Toumi, K., Ortiz, C., and Grodzinsky, A., 2013, "High-Bandwidth AFM-Based Rheology Reveals That Cartilage Is Most Sensitive to High Loading Rates at Early Stages of Impairment," Biophys. J., 104(7), pp. 1529–1537.

[19] Huang, C.-Y., Soltz, M. A., Kopacz, M., Mow, V. C., and Ateshian, G. A., 2003, "Experimental Verification of the Roles of Intrinsic Matrix Viscoelasticity and Tension-Compression Nonlinearity in the Biphasic Response of Cartilage," J. Biomech. Eng., 125(1), pp. 84–93.

[20] Mak, A. F., 1986, "The Apparent Viscoelastic Behavior of Articular Cartilage—The Contributions from the Intrinsic Matrix Viscoelasticity and Interstitial Fluid Flows," J. Biomech. Eng., 108(2), pp. 123–130.

[21] Edelsten, L., Jeffrey, J. E., Burgin, L. V., and Aspden, R. M., 2010, "Viscoelastic Deformation of Articular Cartilage during Impact Loading," Soft Matter, 6(20), pp. 5206–5212.

[22] Fulcher, G. R., Hukins, D. W. L., and Shepherd, D. E. T., 2009, "Viscoelastic Properties of Bovine Articular Cartilage Attached to Subchondral Bone at High Frequencies," BMC Musculoskelet. Disord., 10, p. 61.

[23] Han, G., Eriten, M., and Henak, C. R., 2019, "Rate-Dependent Crack Nucleation in Cartilage under Microindentation," J. Mech. Behav. Biomed. Mater., 96, pp. 186–192.

[24] Lawless, B. M., Sadeghi, H., Temple, D. K., Dhaliwal, H., Espino, D. M., and Hukins, D. W. L., 2017, "Viscoelasticity of Articular Cartilage: Analysing the Effect of Induced Stress and the Restraint of Bone in a Dynamic Environment," J. Mech. Behav. Biomed. Mater., 75, pp. 293–301.

[25] Wahlquist, J. A., DelRio, F. W., Randolph, M. A., Aziz, A. H., Heveran, C. M., Bryant, S. J., Neu, C. P., and Ferguson, V. L., 2017, "Indentation Mapping Revealed Poroelastic, but Not

Viscoelastic, Properties Spanning Native Zonal Articular Cartilage," Acta Biomater., 64, pp. 41–49.

[26] Chan, D. D., Cai, L., Butz, K. D., Trippel, S. B., Nauman, E. A., and Neu, C. P., 2016, "*In Vivo* Articular Cartilage Deformation: Noninvasive Quantification of Intratissue Strain during Joint Contact in the Human Knee," Sci. Rep., 6, p. 19220.

[27] Fukubayashi, T., and Kurosawa, H., 1980, "The Contact Area and Pressure Distribution Pattern of the Knee: A Study of Normal and Osteoarthrotic Knee Joints," Acta Orthop. Scand., 51(1–6), pp. 871–879.

[28] Griffin, D. J., Vicari, J., Buckley, M. R., Silverberg, J. L., Cohen, I., and Bonassar, L. J., 2014, "Effects of Enzymatic Treatments on the Depth-Dependent Viscoelastic Shear Properties of Articular Cartilage," J. Orthop. Res., 32(12), pp. 1652–1657.

[29] Park, S., Nicoll, S. B., Mauck, R. L., and Ateshian, G. A., 2008, "Cartilage Mechanical Response under Dynamic Compression at Physiological Stress Levels Following Collagenase Digestion," Ann. Biomed. Eng., 36(3), pp. 425–434.

[30] Nguyen, Q., Murphy, G., Roughley, P. J., and Mort, J. S., 1989, "Degradation of Proteoglycan Aggregate by a Cartilage Metalloproteinase. Evidence for the Involvement of Stromelysin in the Generation of Link Protein Heterogeneity in Situ.," Biochem. J., 259(1), pp. 61–67.

[31] Quinn, T. M., Allen, R. G., Schalet, B. J., Perumbuli, P., and Hunziker, E. B., 2001, "Matrix and Cell Injury Due to Sub-Impact Loading of Adult Bovine Articular Cartilage Explants: Effects of Strain Rate and Peak Stress," J. Orthop. Res., 19(2), pp. 242–249.

[32] Wong, M., Ponticiello, M., Kovanen, V., and Jurvelin, J. S., 2000, "Volumetric Changes of Articular Cartilage during Stress Relaxation in Unconfined Compression," J. Biomech., 33(9), pp. 1049–1054.

[33] Qin, L., Zheng, Y., Leung, C., Mak, A., Choy, W., and Chan, K., 2002, "Ultrasound Detection of Trypsin-Treated Articular Cartilage: Its Association with Cartilaginous Proteoglycans Assessed by Histological and Biochemical Methods," J. Bone Miner. Metab., 20(5), pp. 281–287.

Chapter 4 Rate-dependent crack nucleation in cartilage under microindentation*

Guebum Han, Melih Eriten, and Corinne R. Henak

*(*Reprinted from Journal of the Mechanical Behavior of Biomedical Materials*
with permission from Elsevier)

4.1. Abstract

This study investigates rate-dependent crack nucleation in cartilage under microindentation using a poroviscoelastic framework and nano/microscopic images. Localized crack failure was induced at known locations and at different loading rates via microindentation with an axisymmetric sphero-conical indenter. Finite element (FE) modeling was used to reproduce results of microindentation tests within a PVE framework. Scanning electron microscopy (SEM) was used to examine nano- and microscale structural features of crack surfaces. Microindentation results showed rate-dependent crack nucleation in cartilage. In particular, critical total work required for crack nucleation was larger at the slow loading rate compared to the fast loading rate. FE results suggested that viscoelastic relaxation of cartilage was a major contributor to the rate dependency and that tensile stresses localized at the indenter tip was a governing factor in crack nucleation. SEM images combined with microindentation and FE results suggested that the solid matrix in the vicinity of the tip experienced relatively large relaxation and kinematic fiber rearrangement at the slow loading rate in comparison to the fast loading rate. These findings extend current understanding of rate-dependent failure mechanisms in cartilage.

Keywords Rate dependence; fracture; crack nucleation; poroelasticity; intrinsic viscoelasticity

4.2. Introduction

Articular cartilage is a heterogeneous material composed of dense solid matrix and fluid. The major constituents of the solid matrix are collagen fibrils (about 15-22 % of wet weight [1]) and proteoglycans (PGs) with sulfated glycosaminoglycan (GAG) side chains (about 4-7 % of wet weight [1]). Collagen fibrils primarily resist tension [2–4]. Cohesive strength of cartilage is attributed to collagen fibril-based interactions rather than GAG-based interactions [5,6]. Negatively charged GAGs provide compressive resistance via charge-to-charge repulsion and osmotic pressure [1,7]. Fluid is the largest portion of cartilage (about 60-85 % of wet weight), and it plays an important role in swelling collagen fibrils (about 30 % of total water) and creating pore space in the solid matrix [1,8,9]. Cartilage functions as a load-bearing and dissipative material because of its composition [10–14]. These functions of cartilage may not be maintained after failure (i.e., cracks [15,16]) under various loading conditions. Nevertheless, mechanisms of rate-dependent cartilage failure are only partially understood.

Poroelastic (PE) and viscoelastic (VE) relaxations govern the rate-dependent mechanical response of intact cartilage. PE relaxation originates from stress-induced fluid flow (diffusion), which dissipates energy through fluid-solid frictional interaction [11,17,18]. As PE relaxation is flow-dependent, its time constant depends on a characteristic diffusion length scale [10,11,19]. For example, the contact length between an indenter and a sample can be considered as a characteristic diffusion length where fluid flows. A PE time constant is proportional to the square of a characteristic diffusion length (e.g., contact radius) [10,11]. Intrinsic VE relaxation originates from rearrangement and interactions of solid matrix macromolecules (i.e., collagen fibrils and PGs) [11,18,20]. Hence, in contrast to PE relaxation, VE relaxation is flow-independent, and therefore its time constant of effective intrinsic VE relaxation can be assumed independent of any characteristic diffusion length scales at continuum [10,19,21]. Combined effect of poroviscoelastic (PVE) relaxations is shown to explain the observations of rate-dependent mechanical properties [10,22–24] and is utilized in finite element (FE) models of cartilage [24–27]. Those relaxation mechanisms, however, have not yet been tied to rate-dependent failure mechanics in cartilage. A recent study showed that VE relaxation successfully accounts for the rate-dependent failure in hydrogels (i.e., rate-dependence of stress and stretch at failure, and crack opening profiles) [28]. Despite significant ultrastructural differences, hydrogels and cartilage exhibit similarities in their time-dependent response, which suggests that time-dependent mechanical response can explain rate-dependent failure in cartilage.

Rate dependence of failure properties of cartilage has been observed at macroscopic length scales, but is not linked to rate-dependent mechanics at nano/microscopic length scales. For instance, cyclic tensile loading at a relatively low frequency was found to slow the growth of a pre-existing crack in cartilage and cause necking phenomena [29]. Cyclic compressive loading at a relatively high frequency appeared to shorten the time to equilibrate and cause more damage to the microstructure of cartilage [30]. In addition, cyclic compressive loading at a relatively high frequency was found to induce large crack lengths regardless of an applied maximum load [31]. Mechanical impact has been used to investigate the onset of post-traumatic osteoarthritis (OA) and caused cartilage failure such as micro/macrocracks and fissures [32–34]. Lastly, a more recent study with a sharp blade showed that critical load, critical displacement, and critical energy required for crack nucleation decreased with increased loading rates [35]. Notwithstanding, a lack of nano/microscopic observation of rate-dependent crack nucleation in cartilage has limited the understanding of its mechanisms. Conversely, rate-dependent crack nucleation has been observed in skin, a collagen-rich tissue with structural similarities to cartilage. For instance, nano/microscopic fractography in skin showed relatively slow strain rate caused fiber bundles to split, indicating fibers had sufficient time to relax and slide [36]. Furthermore, nano/microscopic observation of skin under tensile loading demonstrated that the rearrangement of fibrils toward fracture involved rotation, straightening, stretching, sliding, and delamination of fibrils [37]. In order to effectively observe such rate-dependent features of cartilage failure at nano/microscopic scales, localized failure should be introduced at precise rates and locations. A previous study showed microindentation with an axisymmetric indenter could achieve crack initiation tests on cartilage with smaller standard deviations compared to macroscopic tests [38]. However, rate-dependence of cartilage failure was not evaluated. The small standard deviation was noteworthy as failure results of soft tissues are notorious for high variation [38,39]. Therefore, the combination of microindentation-based crack initiation and nano/microscopic imaging techniques can provide a possible link between rate-dependent cartilage failure and physical mechanisms.

The objective of this study is to explain rate-dependent crack nucleation in cartilage under microindentation using nano/microscopic images and a PVE framework. Crack nucleation was generated at different loading rates by microindentation at a well-defined location around the indenter tip. Crack nucleation was defined as a failure event inducing a sudden burst of load during the displacement-controlled indentation due to rupture of intact cartilage. Critical load, critical displacement, and critical total work were determined at a sudden burst of load with a negative slope in a load-displacement curve. Fractographic examination was performed by observing nano- and micro-scale features of crack surfaces via scanning electron microscopy (SEM). A 3D axisymmetric FE model with PVE relaxations was developed, and then tuned based on the results of microindentation tests. FE predictions suggested the relative role of PVE relaxations in rate-dependent crack nucleation; in conjunction with nano/microscopic images of crack surfaces, this aids in interpreting experimentally-measured rate-dependence in crack nucleation under microindentation.

4.3. Methods

4.3.1. Sample Preparation

Eight full-thickness cartilage samples were harvested from patellae of porcine joints acquired from a local abattoir (4 animals, 5-6 months old, sex unknown and assumed random). A biopsy punch and a scalpel were used to obtain 6 mm diameter cylindrical cores. Subchondral bone was removed using a microtome to create a deep surface parallel to the articular surface and allow indentations to be perpendicular to the articular surface. Cores were cut in half to make hemi-cylindrical samples. The deep zone of each sample was attached to a Petri dish using cyanoacrylate (Loctite 495, Henkel, Germany). Samples were kept hydrated during preparation in Dulbecco's phosphate-buffered saline (DPBS). The average cartilage thickness was 1.58±0.20 mm.

4.3.2. Crack nucleation via microindentation tests

Microindentation tests were performed to create crack nucleation at different loading rates. Tests were conducted on a Bruker TI 950 TriboIndenter (Bruker, Eden Prairie, MN) with a diamond sphero-conical tip (tip radius, R = 20 μm and tip angle, θ_{tip} = 60 degrees) (Figure 4-1a). Cartilage samples were indented perpendicular to articular surface at 1 μm/s (slow loading rate: SLR) and 600 μm/s (fast loading rate: FLR) while load response was measured. These contrasting rates were selected because the time required for crack nucleation at the SLR was sufficiently longer than the relaxation time of cartilage, while the time at the FLR was shorter. In addition, reliable data could not be obtained at loading rates lower than 1 μm/s and greater than 600 μm/s, primarily due to thermal drift and time lag in controller response. Samples were kept hydrated in DPBS and protease inhibitor (PI) during tests. Critical load, critical displacement, and critical total work were determined at a sudden drop with a negative slope in a load-displacement curve (Figure 4-1b), indicating sudden rupture of intact cartilage that was sufficiently large to be captured with the current instrument. This failure was defined as crack nucleation in the current study. Critical total work was calculated from the area under load-displacement curves using trapezoidal integration in Origin 2017 software (OriginLab, Northampton, MA). Each loading rate was tested at one location on eight samples (2 samples from each animal). Test locations between samples were consistently controlled based on testing stage coordinates (Figure 4-1a).

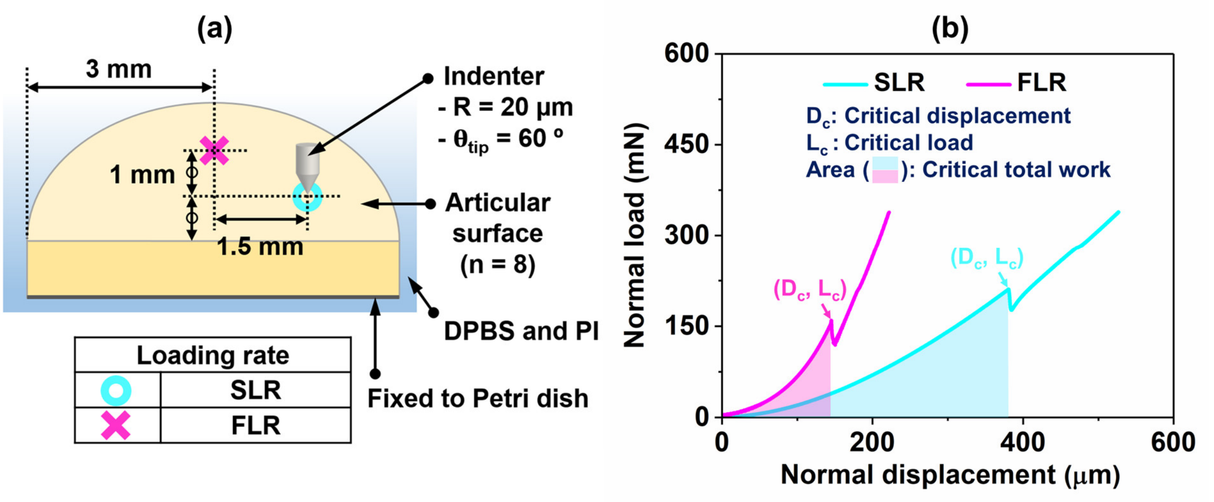

Figure 4-1: (a) Schematic diagram of experimental setup and (b) representative load-displacement curves of crack nucleation tests with key parameters (critical displacement, critical load, and critical total work). Samples were completely immersed in DPBS and PI during tests, and the indenter direction was perpendicular to articular surface. Loading rates were determined by considering the relaxation time of cartilage.

4.3.3. Nano/microscopic evaluation of cracks

Crack surfaces created by microindentation tests were observed using SEM (S-3200, Hitachi, Tokyo) in order to image nano/microscopic structural features (~ 100 nm). Prior to SEM imaging, cartilage samples were fixed in 10% formalin for a minimum of 24 hours. Samples were chemically dehydrated in graded concentrations of ethanol, then critical point dried (Samdri 780, Tousimis, Rockville, MD), and coated with platinum via a sputter coater (Auto Conductavac IV, SeeVac, PA).

4.3.4. FE modeling

A 3D axisymmetric FE model (wedge angle of 3 degrees) of the indenter-sample system was used to explain rate-dependent behavior of cartilage within a PVE framework, and determine a governing factor in crack nucleation. The dimensions of the indenter tip model were identical to the diamond tip used for microindentation tests (tip radius, R: 20 μm and tip angle, θ_{tip}: 60 degrees) (Figure 4-2). The dimensions of the cartilage model were 1.58 mm in thickness and 2 mm in radius. The average cartilage thickness was selected (1.58±0.20 mm). The radius of the cartilage model was sufficiently large in comparison to the indentation depth and contact radii at failure so that there is no boundary effect. The indenter tip model was set to indent the cartilage model at different loading rates (SLR: 1 μm/s and FLR: 600 μm/s) corresponding to the experimental indentation tests. The front face of the cartilage model was fixed in the direction of y-axis, the bottom face was fixed in all directions, and the axis of symmetry was fixed in the directions of x- and y-axes (Figure 4-2). The contact between the tip and cartilage models was set as frictionless biphasic-on-rigid contact (facet-to-facet contact with the augmented Lagrangian method). The surface outside the contact was set as free-draining conditions. The contact between the back face of the cartilage model and the symmetry plane was set as a tension-compression contact interface (zero displacement in the out-of-plane direction and unconstrained displacement in the in-plane direction), enforcing a symmetric constraint. Boundary and contact conditions are explained with a whole FE model in Appendix A (Figure A-1). The rigid tip and cartilage models were generated in SolidWorks 2017, Gmesh [40], and PreView version 1.20.2, respectively.

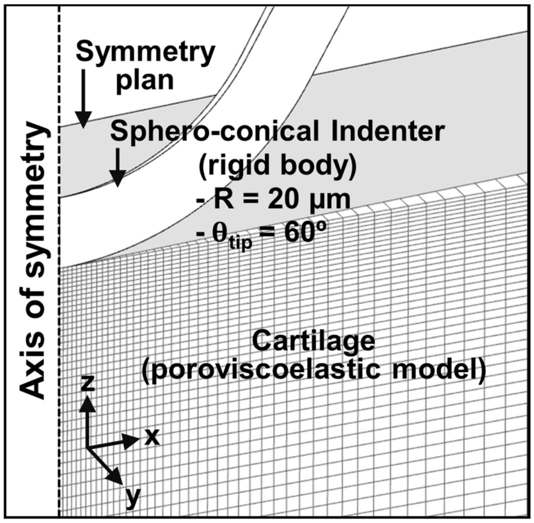

Figure 4-2: Sphero-conical indenter (rigid body) and cartilage (PVE model) for FE modeling. A whole FE model with key indications is presented in Appendix A (Figure A-1).

Cartilage was modeled as a fiber-reinforced PVE solid, and the indenter was modelled as rigid and impermeable (Figure 4-2). Cartilage was discretized into hexahedral (20,592 elements) and pentahedral (144 elements) elements. The cartilage mesh was biased with the smallest elements at axis of symmetry. The number of elements required was determined by mesh convergence analysis. The non-fibrillar cartilage matrix, also often called as the porous matrix, was modeled as a biphasic material via the combination of a neo-Hookean material (elastic modulus, E = 0.6 MPa [41], and Poisson's ratio, v = 0.3 [41]) and strain-dependent permeability (Holmes-Mow with permeability, k_0 = 0.0027 mm^4/Ns [42], power-law exponent, M = 2.2 [42], and power-law exponent, α_{perm} = 2 [42]). A porous-permeable solid matrix, mainly representing

PGs, and fluid were assumed to be incompressible, but the combined porous matrix was modeled to be compressible due to the volumetric change by the exudation of fluid from the pore space. The fibrillar cartilage matrix was modeled as a nonlinear elastic material with an isotropic distribution (power of exponential argument, β = 2.15 [25] and modulus, ξ = fitting parameter). VE response of fibrils was imposed with one time constant (relaxation time, τ =1.8 seconds [43], and VE coefficient, γ = fitting parameter); one relaxation time constant was selected to represent the VE response in order to minimize the number of parameters [43]. The definitions of the material parameters in the models are given in Appendix A. The indenter tip was made of diamond, and thus it was reasonable to set the indenter model as rigid and impermeable. FE simulations were solved in FEBio version 2.5.2 [44].

The fitting parameters (ξ and γ) were determined by fitting simulated load-displacement curves to average load-displacement curves from microindentation tests at 1 μm/s (SLR) and 600 μm/s (FLR). Average curves were obtained by averaging all load-displacement curves just prior to crack failure. The range of the average curves used for the fitting process was up to the lowest critical displacement at each loading rate. ξ and γ were determined by fitting simulated curves to the average load-displacement curves at the SLR and FLR. The curve fitting was evaluated with R-squared values. Distributions of principal solid Cauchy stresses (σ_1 and σ_3), principal Lagrangian strains (E_1 and E_3), and strain energy density just prior to crack nucleation were taken along the axis of symmetry where their maximum absolute values were generated. These results were relatively insensitive to the fitting parameters (ξ and γ), and therefore reliable. Specifically, plus and minus 10 % of ξ changed 4.96±3.55 % and 5.07±3.70 % of the FE-predicted results, respectively. Plus and minus 10 % of γ changed 2.18±3.15 % and 2.23±3.20 % of the FE-predicted results, respectively. The upper and lower bounds of the distributions were estimated at plus or minus one standard deviation of the average critical displacement from microindentation tests, respectively. Principal stresses, principal strains, and strain energy densities of the solid matrix were evaluated along the axis of symmetry and at the critical displacements because the end of the tip just prior to crack nucleation was the region of interest. These FE results were obtained in PostView version 1.10.2.

4.3.5. Statistical Analysis

Mann-Whitney U test (nonparametric test) was used to statistically compare experimental data from the two loading rates. All statistical analysis was conducted using MATLAB (The MathWorks, Inc., Natick, MA). A significance level of 5% was employed for all tests.

4.4. Results

While critical load was not significantly different between the SLR and FLR, critical displacement and critical total work were significantly larger at the SLR compared to the FLR. Although critical load at the SLR (189.06±35.50 mN) was numerically 1.19 times higher than that at the FLR (159.24±48.47 mN), the difference was not significant (p = 0.16) (Figure 4-3a). Critical displacement at the SLR (390.45±75.54 μm) was 2.74 times higher than that at the FLR (142.72±16.03 μm), and the rate dependence of the critical displacement was significant ($p = 1.55\times10^{-4}$) (Figure 4-3b). Critical total work at the SLR (29.10±10.03 μJ) was 3.49 times higher than that at the FLR (8.34±3.83 μJ), and the rate dependence of the critical total work was significant ($p = 1.55\times10^{-4}$) (Figure 4-3c). Therefore, the rate dependence of cartilage was predominant in the critical displacement and total work in comparison to the critical load. All load-displacement curves used for the determination of critical parameters (Figure 4-3) are provided in Appendix A (Figure A-2).

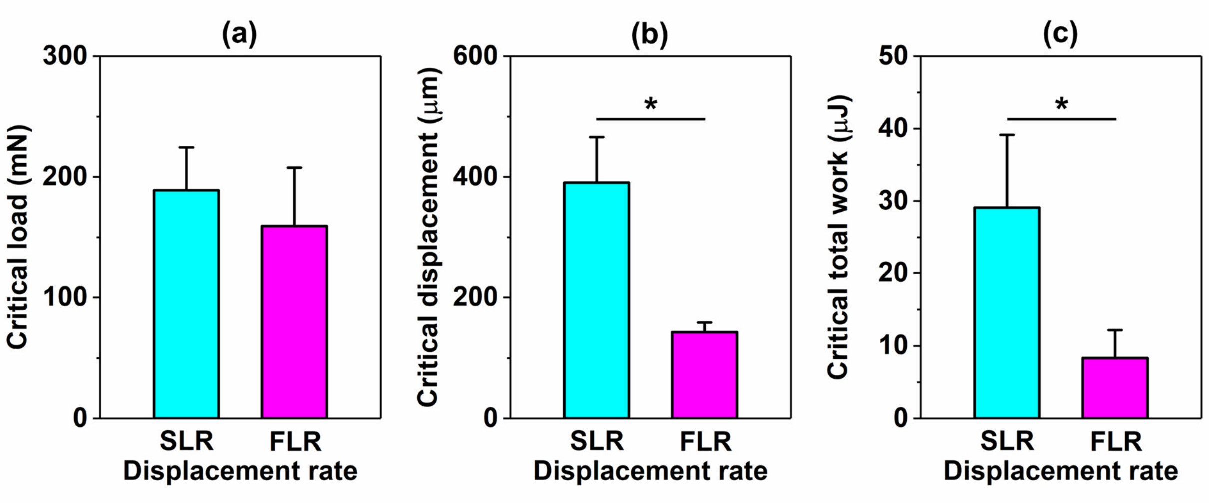

Figure 4-3: (a) Critical load, (b) critical displacement, and (c) critical total work. * indicates statistical significance between loading rates.

SEM images of cracks at the articular surface showed different morphological characteristics following initiation at the SLR and FLR. Low magnification images (Figure 4-4a and d) showed that crack nucleation initially occurred by opening and breaking the highly dense solid matrix in a plane perpendicular to the indentation direction. The images of crack surfaces at the center (Figure 4-4b and e) showed different morphology of the solid matrix depending on the loading rate. The solid matrix, including collagen fibrils, after crack nucleation at the SLR was relatively aligned in the direction perpendicular to the indentation direction (Figure 4-4b). In contrast, the solid matrix, including collagen fibrils, after crack nucleation at the FLR was relatively random orientation (Figure 4-4e). Crack edges (Figure 4-4c and f) showed rate-dependent morphology of the solid matrix. The crack edges generated at the SLR showed a relatively aligned solid matrix perpendicular to crack-growth direction, while that generated at the FLR exhibited a relatively thin and disordered solid matrix bridging the crack.

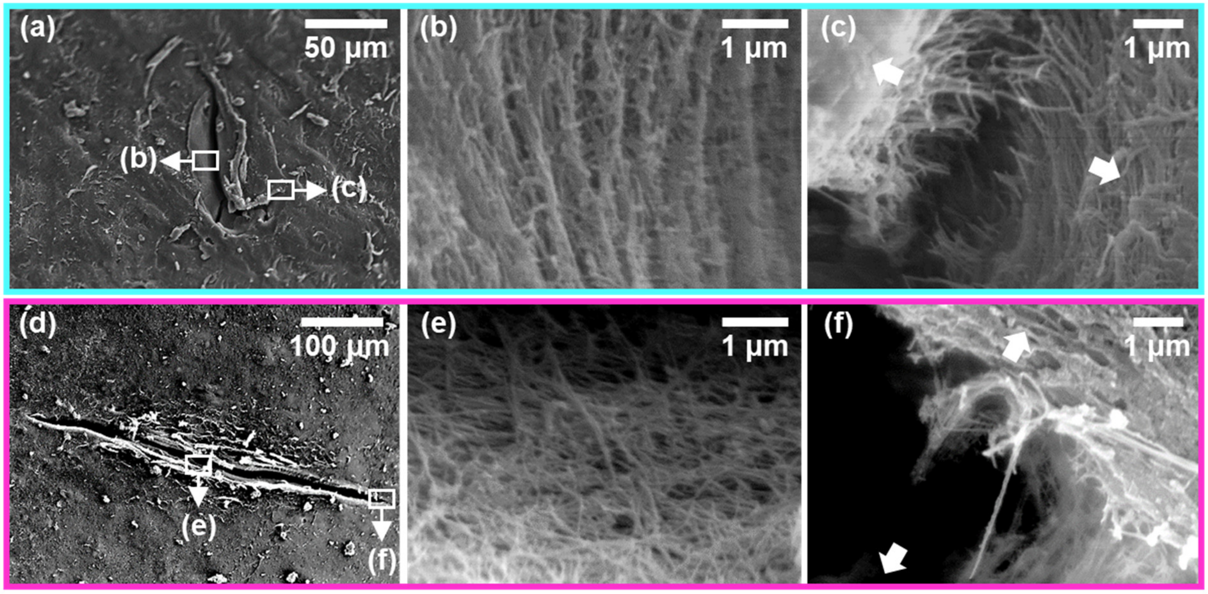

Figure 4-4: SEM images of cracks created by microindentation at different loading rates ((a-c) SLR and (d-f) FLR). (a) and (d) show the whole cracks. (b) and (e) were from the centers of cracks. (c) and (f) were from the edges of cracks. The arrows in (c) and (f) indicate the crack-opening direction at the edges.

Rate-dependent experimental load-displacement curves from microindentation tests were reproduced using a single set of material properties in the FE model (Figure 4-5a). Load-displacement curves from the FE model fitted the average curves of experimental curves ($R^2 > 0.99$ for the SLR and FLR). The determined values of the fitting parameters were $\xi = 3.7$ MPa and $\gamma = 6.1$.

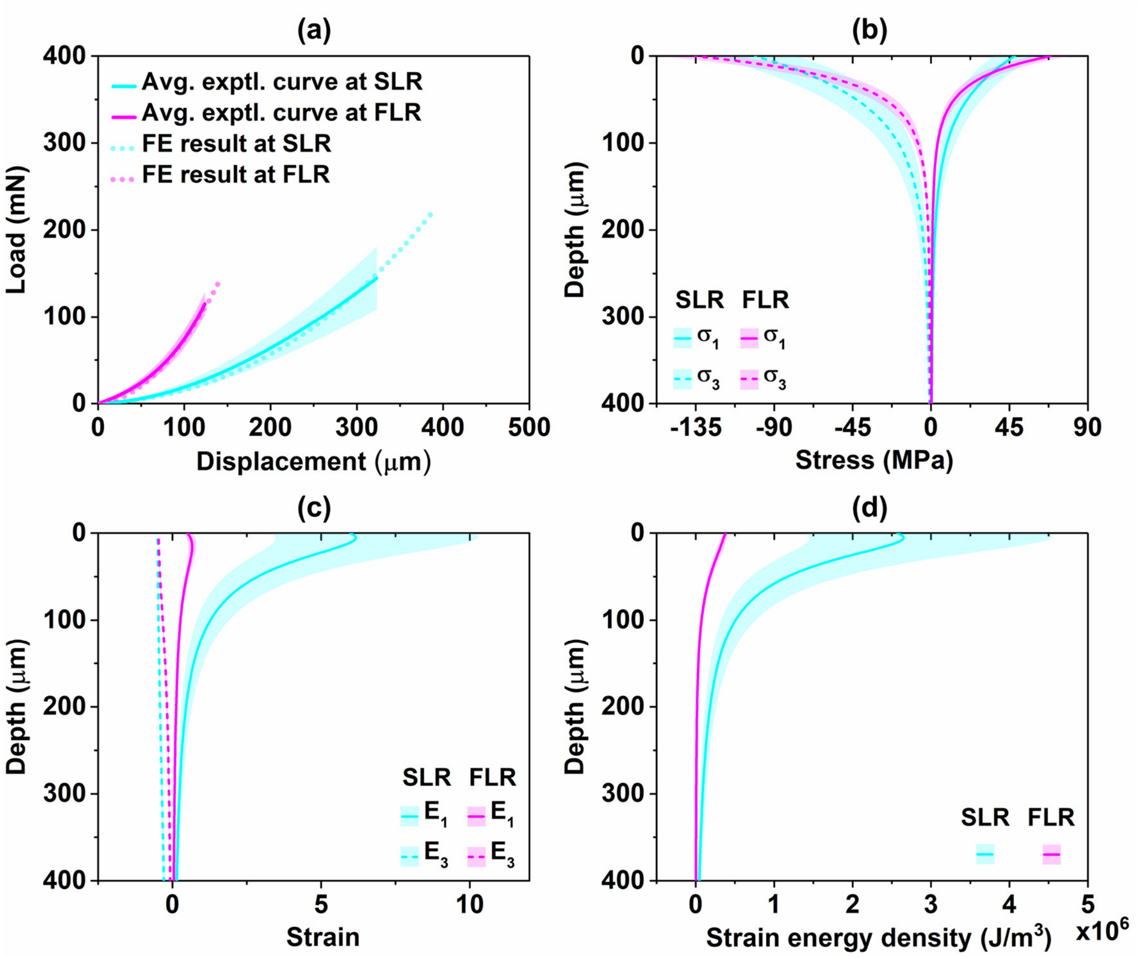

Figure 4-5: FE-predicted results: (a) comparison between FE-predicted and experimentally measured load-displacement curves, (b) FE-predicted principal Cauchy stresses, (c) FE-predicted principal Lagrangian strains, and (d) FE-predicted strain energy density. FE predictions were sampled along the symmetry axis as a function of depth in the undeformed configuration.

While the distributions of the principal stresses (i.e., σ_1 and σ_3) from the two loading rates were relatively similar to each other, the distributions of the principal strains (i.e., E_1 and E_3) and strain energy densities were not (Figure 4-5b-d). The maximum principal stresses at the SLR were 47.91 MPa for σ_1 and -100.85 MPa for σ_3. For the FLR, the maximum principal stresses were 68.44 MPa for σ_1 and -135.16 MPa for σ_3. In both cases, σ_1 was perpendicular to the indentation direction (i.e., parallel to the radial and circumferential directions), and σ_3 was parallel to the indentation direction. The maximum principal strains at the SLR were 6.17 for E_1 and -0.49 for E_3. The maximum principal strains at the FLR were 0.66 for E_1 and -0.47 for E_3. The maximum strain energy densities at the SLR and FLR were at 2.65×10^6 J/m^3 and 0.38×10^6 J/m^3, respectively. All values of the stresses, strains, and strain energy densities became negligible beyond a depth of about 350 μm. The contour plots of theses FE-predicted results are presented in Appendix A (Figure A3-5).

4.5. Discussion

Microindentation-based crack nucleation in articular cartilage was rate-dependent, and FE predictions indicated that cartilage sufficiently underwent relaxation at the SLR, but not at the FLR. In particular, crack nucleation at the SLR required more work than crack nucleation at the FLR (Figure 4-3c). A substantial amount of the total work at the SLR was likely used for PVE relaxations during loading in the vicinity of the indenter tip because the SLR was sufficiently slower than the major relaxation (5-10 seconds) of cartilage [10,21,45]; crack nucleation occurred at 390.45±75.54 seconds. The FE parametric study on the SLR showed that the exclusion of the PE and VE relaxations in the FE modeling did not have a pronounced effect on the load-displacement curves at the SLR, supporting the conclusion that the relaxations sufficiently occurred at the SLR (Figure A-6a). In addition, the FE-predicted strain rates at the SLR were 0.04 s^{-1} for E_1 and -3.54×10^{-5} s^{-1} for E_3 just prior to failure and could correspond to humans resting; the estimation process is included in Figure A-7. In contrast, most of the total work at the FLR was likely used for crack nucleation without substantial energy dissipation because the loading rate was faster than the major relaxation time scales of cartilage [10,21,45]; crack nucleation occurred at 0.24±0.03 seconds. The FE-predicted strain rates at the FLR were 4.74 s^{-1} for E_1 and -0.23 s^{-1}

for E_3 just prior to failure and could correspond to the lower bound of the strain rates induced during walking, jumping, and running (Figure A-7).

VE relaxation likely governed the rate-dependent load response. The FE parametric studies on the FLR and the SLR showed that the relative contribution of VE relaxation to the rate dependence of the load-displacement curves was larger than PE relaxation (Figure A-6). While the FE model that only included VE relaxation reproduced most of the rate-dependent load response, the FE model only including PE relaxation could not even with an extended range of permeability ($0.1 \times k_0$ and $10 \times k_0$) (Figure A-6b). Therefore, k_0 was obtained from a previous study [42], with values consistent with additional literature [46,47]. In addition, fluid pressure in the vicinity of the tip at the FLR was less than 2 % of the solid stresses (Figure A-5), reiterating the relative contribution of VE relaxation to the load response was much larger in comparison with PE relaxation.

Rate-dependent nano- and microscale features of crack surfaces reiterated the role of relaxation in crack nucleation. The distinct morphological difference between the SLR and FLR was likely due to the degree of relaxation in cartilage at a given loading rate. The SEM image of SLR crack surfaces at the center of the crack showed that the solid matrix was rearranged perpendicular to the indentation direction (Figure 4-4b), suggesting that the solid matrix in the vicinity of the tip had a sufficient time to undergo relatively large VE relaxation (i.e., rearrangement and alignment along tensile principal stresses (i.e., σ_1)) while accommodating the slowly applied loading by the sphero-conical tip. This sufficient relaxation of cartilage at the SLR was supported with the microindentation and FE results. In addition, a previous study observed such loading-induced kinematic rearrangement of type I collagen fibrils in skin [37]. On the other hand, the image of FLR crack surfaces showed more random distribution of the solid matrix including broken fibrils (Figure 4-4e) when compared to the SLR, suggesting that the solid matrix did not have sufficient time to be rearranged to accommodate the sudden loading.

In addition to the center areas, the edges of cracks showed rate-dependent morphological characteristics and the process of crack growth. The image of the crack edge created at the SLR suggested that the solid matrix experienced large enough relaxation to rearrange the solid matrix perpendicular to crack-growth direction, and eventually rupture (Figure 4-4c). In contrast, the image of the crack edge created at the FLR suggested the solid matrix did not undergo severe relaxation (Figure 4-4f). Also, the comparison of the solid matrix in the intact area and crack edge showed the fast crack opening might cause delamination of the solid matrix including fibrils, resulting in relatively thin structural features bridging the crack edge surfaces. Previous studies also observed delamination of fibrils in collagenous materials [37,48] and thin structural features bridging crack edges [34]. The line shapes of cracks at the SLR and FLR (Figure 4-4a and d) suggested that cracks likely opened along the preferential orientation of the solid matrix, which was consistent with previous studies showing that articular surface has preferential opening orientation [49,50].

Cartilage relaxation delayed principal tensile stresses build-up at the indenter tip, resulting in delayed crack nucleation. Experimental results, nano/microscopic images, and FE predictions indicated that crack nucleation in cartilage experienced much larger relaxation at the SLR compared to the FLR. FE-predicted principal tensile stresses (i.e., maximum σ_1) from the SLR and FLR were relatively similar to each other (Figure 4-5b), whereas principal tensile strains (i.e., maximum E_1) were not (Figure 4-5c). Therefore, tensile stresses localized at the indenter tip were likely a governing factor in crack nucleation. Thus, the experimental results combined with the FE predictions suggested that the SLR reached the critical tensile stresses more slowly than those at the FLR due to relaxation and kinematic rearrangement of the solid matrix in the vicinity of the tip during loading. In addition, these results combined with the line shapes of cracks (Figure 4-4a and d) suggested that crack nucleation was initiated by opening and separating the solid matrix via the critical tensile stresses generated in the vicinity of the tip and in its preferential orientation [49,50]. The predicted critical tensile stresses (σ_1 = 47.91 MPa at SLR and σ_1 = 68.44 MPa at FLR (Figure 4-5b)) of the bulk solid matrix were comparable with previously reported fracture stresses of individual Type 1 collagen fibrils (71±23 MPa [51] and 60±10 MPa [43]). This comparison could be supported by a previous study showing that collagen fibrils, which are the major constituent of the solid matrix, were associated with cartilage failure in its preferential orientation as well as non-preferential orientation [49]. The difference between the predicted tensile stresses of the bulk solid matrix and those of individual collagen fibrils could be due to non-fibrillar matrix (i.e., PGs) [51], collagen fibrils-PGs interaction [51], types of collagen fibrils, and depth-dependent properties of cartilage. Nevertheless, previous studies showed that cohesive strength of cartilage was dominantly governed from collagen fibrils rather than PGs-based interactions [5,6].

Even though this study extends our understanding of underlying mechanisms of rate-dependent failure in articular cartilage, it has some limitations. The polarized loading rates used for tests successfully showed rate-dependent crack nucleation in cartilage, but the transitional behavior between the loading rates was outside of the scope of this study. Crack sizes and depths were not quantitatively evaluated because it was challenging to terminate tests right after crack nucleation. Thus, SEM images (Figure 4-4) qualitatively showed rate-dependent morphological features of cartilage cracks under microindentation. The FLR (600 μm/s) was lower than the impact loading rates (about 0.25 m/s) employed in previous studies [32,33]; however, it was fast enough to induce failure behavior distinguished from the SLR by limiting relaxation processes (e.g., realignment of fibrils). Experimental conditions do not match *in vivo* conditions, instead localized damage induced by a geometrically well-defined tip allowed for efficient study of rate-dependent cartilage failure. SEM images of cracks were taken after swelling and unloading processes and therefore did not represent nano- and microscale features of the solid matrix at the moment of crack nucleation. Swelling and unloading processes were likely to decrease the density of cartilage compared to the moment of failure. The FE model did not consider the depth-dependent material properties or structure [1,52–54]. This simplification was made in order to minimize the number of fitting parameters. However, the effect of the fibril orientation would be relatively negligible when considering that samples were obtained from immature animals (5-6 months old) [52]. The FE model was generated at continuum and therefore did not predict individual ultrastructural behavior, which would require more sophisticated models at different length scales [55,56]. Contact between the indenter and cartilage was assumed to be frictionless [11,57] because cartilage exhibits a low coefficient of friction due to excellent lubrication mechanisms such as biphasic lubrication [58]. In particular, as cartilage was being compressed during the indentation, negligible friction was expected due to the exudation of fluid in the vicinity of the indenter tip. Nonetheless, the FE model provided useful information for interpreting microindentation results and nano/microscopic changes in the vicinity of crack surfaces. The current findings do not directly explain microsplits and wrinkle-like structures observed in the early OA [59]. However, they suggested that mechanical loading rate could affect failure mechanisms of cartilage, ultimately resulting in the early OA. Our findings suggest that the dominant resistance of cartilage to crack initiation stems from the capacity of solid matrix realignment and VE losses associated with that realignment.

4.6. Conclusions

This paper investigated rate-dependent crack nucleation in cartilage under microindentation with interpretation aided by nano/microscopic images of crack surfaces and a PVE FE model. Microindentation with an axisymmetric sphero-conical indenter effectively induced localized rate-dependent crack nucleation at known locations. Combined FE modeling and experimental results suggested that VE relaxation of cartilage played a dominant role in rate-dependent crack nucleation compared to PE relaxation, and that tensile stresses localized at the indenter tip governed cartilage failure. The confirmation of rate-dependent crack surfaces combined with the microindentation and FE results indicated that the solid matrix in the vicinity of the tip experienced relatively large relaxation at the SLR compared to the FLR, resulting in delayed crack nucleation. These findings provided possible mechanisms governing rate-dependent cartilage failure. They also showed promising aspects of microindentation-based crack nucleation tests as a technique to investigate cartilage. In addition, the critical parameters obtained from crack nucleation tests can be used for the development of predictive models.

4.7. Acknowledgment

We gratefully acknowledge the help provided by Benjamin Stadnick and Richard Nay at Bruker. Support for this research was provided by the University of Wisconsin-Madison, Office of the Vice Chancellor for Research and Graduate Education with funding from the Wisconsin Alumni Research Foundation.

4.8. References

[1] Mow, V. C., Ratcliffe, A., and Robin Poole, A., 1992, “Cartilage and Diarthrodial Joints as Paradigms for Hierarchical Materials and Structures,” Biomaterials, 13(2), pp. 67–97.

[2] Kempson, G. E., Freeman, M. a. R., and Swanson, S. a. V., 1968, “Tensile Properties of Articular Cartilage,” Nature, 220(5172), pp. 1127–1128.

[3] Andriotis, O. G., Desissaire, S., and Thurner, P. J., 2018, “Collagen Fibrils: Nature’s Highly Tunable Nonlinear Springs,” ACS Nano, 12(4), pp. 3671–3680.

[4] Soulhat, J., Buschmann, M. D., and Shirazi-Adl, A., 1999, “A Fibril-Network-Reinforced Biphasic Model of Cartilage in Unconfined Compression,” J. Biomech. Eng., 121(3), pp. 340–347.

[5] Broom, N. D., and Silyn-Roberts, H., 1990, “Collagen-Collagen versus Collagen-Proteoglycan Interactions in the Determination of Cartilage Strength,” Arthritis Rheum, 33(5), pp. 1512–1517.

[6] Zhu, W., Iatridis, J. C., Hlibczuk, V., Ratcliffe, A., and Mow, V. C., 1996, “Determination of Collagen-Proteoglycan Interactions in Vitro,” J. Biomech., 29(6), pp. 773–783.

[7] Han, E., Chen, S. S., Klisch, S. M., and Sah, R. L., 2011, “Contribution of Proteoglycan Osmotic Swelling Pressure to the Compressive Properties of Articular Cartilage,” Biophys. J., 101(4), pp. 916–924.

[8] Maroudas, A., Wachtel, E., Grushko, G., Katz, E. P., and Weinberg, P., 1991, “The Effect of Osmotic and Mechanical Pressures on Water Partitioning in Articular Cartilage,” Biochim. Biophys. Acta BBA - Gen. Subj., 1073(2), pp. 285–294.

[9] Torzilli, P. A., 1985, “Influence of Cartilage Conformation on Its Equilibrium Water Partition,” J. Orthop. Res., 3(4), pp. 473–483.

[10] Han, G., Hess, C., Eriten, M., and Henak, C. R., 2018, “Uncoupled Poroelastic and Intrinsic Viscoelastic Dissipation in Cartilage,” J. Mech. Behav. Biomed. Mater., 84, pp. 28–34.

[11] Nia, H., Han, L., Li, Y., Ortiz, C., and Grodzinsky, A., 2011, “Poroelasticity of Cartilage at the Nanoscale,” Biophys. J., 101(9), pp. 2304–2313.

[12] Akizuki, S., Mow, V. C., Müller, F., Pita, J. C., Howell, D. S., and Manicourt, D. H., 1986, “Tensile Properties of Human Knee Joint Cartilage: I. Influence of Ionic Conditions, Weight Bearing, and Fibrillation on the Tensile Modulus,” J. Orthop. Res., 4(4), pp. 379–392.

[13] Matthews, L. S., Sonstegard, D. A., and Henke, J. A., 1977, “Load Bearing Characteristics of the Patello-Femoral Joint,” Acta Orthop. Scand., 48(5), pp. 511–516.

[14] Boettcher, K., Kienle, S., Nachtsheim, J., Burgkart, R., Hugel, T., and Lieleg, O., 2016, “The Structure and Mechanical Properties of Articular Cartilage Are Highly Resilient towards Transient Dehydration,” Acta Biomater., 29, pp. 180–187.

[15] Pritzker, K. P. H., Gay, S., Jimenez, S. A., Ostergaard, K., Pelletier, J.-P., Revell, P. A., Salter, D., and van den Berg, W. B., 2006, “Osteoarthritis Cartilage Histopathology: Grading and Staging.,” Osteoarthr. Cartil. OARS Osteoarthr. Res. Soc., 14(1), pp. 13–29.

[16] Bauer, M., and Jackson, R. W., 1988, “Chondral Lesions of the Femoral Condyles: A System of Arthroscopic Classification,” Arthrosc. J. Arthrosc. Relat. Surg., 4(2), pp. 97–102.

[17] Lakes, P. R., 2009, *Viscoelastic Materials*, Cambridge University Press, Cambridge ; New York.

[18] Nia, H., Han, L., Soltani Bozchalooi, I., Roughley, P., Youcef-Toumi, K., Grodzinsky, A. J., and Ortiz, C., 2015, “Aggrecan Nanoscale Solid–Fluid Interactions Are a Primary Determinant of Cartilage Dynamic Mechanical Properties,” ACS Nano, 9(3), pp. 2614–2625.

[19] Lai, Y., and Hu, Y., 2017, “Unified Solution for Poroelastic Oscillation Indentation on Gels for Spherical, Conical and Cylindrical Indenters,” Soft Matter, 13, pp. 852–861.

[20] Williams, R. J., 2008, *Cartilage Repair Strategies*, Springer Science & Business Media.

[21] Mak, A. F., 1986, “The Apparent Viscoelastic Behavior of Articular Cartilage—The Contributions From the Intrinsic Matrix Viscoelasticity and Interstitial Fluid Flows,” J. Biomech. Eng., 108(2), pp. 123–130.

[22] Han, G., and Eriten, M., 2018, “Effect of Relaxation-Dependent Adhesion on Pre-Sliding Response of Cartilage,” R. Soc. Open Sci., 5(5), p. 172051.

[23] Huang, C. Y., Mow, V. C., and Ateshian, G. A., 2001, “The Role of Flow-Independent Viscoelasticity in the Biphasic Tensile and Compressive Responses of Articular Cartilage,” J. Biomech. Eng., 123(5), pp. 410–417.

[24] Chiravarambath, S., Simha, N. K., Namani, R., and Lewis, J. L., 2008, “Poroviscoelastic Cartilage Properties in the Mouse from Indentation,” J. Biomech. Eng., 131(1), pp. 011004-011004–9.

[25] Jones, B., Hung, C. T., and Ateshian, G., 2016, “Biphasic Analysis of Cartilage Stresses in the Patellofemoral Joint,” J. Knee Surg., 29(02), pp. 092–098.

[26] DiSilvestro, M. R., Zhu, Q., Wong, M., Jurvelin, J. S., and Suh, J.-K. F., 2000, “Biphasic Poroviscoelastic Simulation of the Unconfined Compression of Articular Cartilage: I—Simultaneous Prediction of Reaction Force and Lateral Displacement,” J. Biomech. Eng., 123(2), pp. 191–197.

[27] Wilson, W., van Donkelaar, C. C., van Rietbergen, B., and Huiskes, R., 2005, “A Fibril-Reinforced Poroviscoelastic Swelling Model for Articular Cartilage,” J. Biomech., 38(6), pp. 1195–1204.

[28] Guo, J., Liu, M., Zehnder, A. T., Zhao, J., Narita, T., Creton, C., and Hui, C.-Y., 2018, “Fracture Mechanics of a Self-Healing Hydrogel with Covalent and Physical Crosslinks: A Numerical Study,” J. Mech. Phys. Solids, 120, pp. 79–95.

[29] Sadeghi, H., Lawless, B. M., Espino, D. M., and Shepherd, D. E. T., 2018, "Effect of Frequency on Crack Growth in Articular Cartilage," J. Mech. Behav. Biomed. Mater., 77(May 2017), pp. 40–46.

[30] Kaplan, J. T., Neu, C. P., Drissi, H., Emery, N. C., and Pierce, D. M., 2017, "Cyclic Loading of Human Articular Cartilage: The Transition from Compaction to Fatigue," J. Mech. Behav. Biomed. Mater., 65(October 2016), pp. 734–742.

[31] Sadeghi, H., Shepherd, D. E. T., and Espino, D. M., 2015, "Effect of the Variation of Loading Frequency on Surface Failure of Bovine Articular Cartilage," Osteoarthritis Cartilage, 23(12), pp. 1–7.

[32] Kaleem, B., Maier, F., Drissi, H., and Pierce, D. M., 2017, "Low-Energy Impact of Human Cartilage: Predictors for Microcracking the Network of Collagen," Osteoarthritis Cartilage, 25(4), pp. 544–553.

[33] Su, A. W., Chen, Y., Dong, Y., Wailes, D. H., Wong, V. W., Chen, A. C., Cai, S., Bugbee, W. D., and Sah, R. L., 2018, "Biomechanics of Osteochondral Impact with Cushioning and Graft Insertion: Cartilage Damage Is Correlated with Delivered Energy," J. Biomech., 73, pp. 127–136.

[34] Henak, C. R., Bartell, L. R., Cohen, I., and Bonassar, L. J., 2017, "Multiscale Strain as a Predictor of Impact-Induced Fissuring in Articular Cartilage," J. Biomech. Eng., 139(3), p. 031004.

[35] Bartell, L. R., Xu, M. C., Bonassar, L. J., and Cohen, I., 2018, "Local and Global Measurements Show That Damage Initiation in Articular Cartilage Is Inhibited by the Surface Layer and Has Significant Rate Dependence," J. Biomech., 72, pp. 63–70.

[36] Arumugam, V., Naresh, M., and Sanjeevi, R., 1994, "Effect of Strain Rate on the Fracture Behaviour of Skin," J. Biosci., 19(3), pp. 307–313.

[37] Yang, W., Sherman, V. R., Gludovatz, B., Schaible, E., Stewart, P., Ritchie, R. O., and Meyers, M. A., 2015, "On the Tear Resistance of Skin," Nat. Commun., 6, p. 6649.

[38] Simha, N. K., Carlson, C. S., and Lewis, J. L., 2004, "Evaluation of Fracture Toughness of Cartilage by Micropenetration," J. Mater. Sci. Mater. Med., 15(5), pp. 631–639.

[39] Roberts, S., Weightman, B., Urban, J., and Chappell, D., 1986, "Mechanical and Biochemical Properties of Human Articular Cartilage in Osteoarthritic Femoral Heads and in Autopsy Specimens," J. Bone Joint Surg. Br., 68(2), pp. 278–288.

[40] Geuzaine, C., and Remacle, J.-F., 2009, "Gmsh: A 3-D Finite Element Mesh Generator with Built-in Pre- and Post-Processing Facilities," Int. J. Numer. Methods Eng., 79(11), pp. 1309–1331.

[41] Li, L. P., Korhonen, R. K., Iivarinen, J., Jurvelin, J. S., and Herzog, W., 2008, “Fluid Pressure Driven Fibril Reinforcement in Creep and Relaxation Tests of Articular Cartilage,” Med. Eng. Phys., 30(2), pp. 182–189.

[42] Ateshian, G. A., Warden, W. H., Kim, J. J., Grelsamer, R. P., and Mow, V. C., 1997, “Finite Deformation Biphasic Material Properties of Bovine Articular Cartilage from Confined Compression Experiments,” J. Biomech., 30(11), pp. 1157–1164.

[43] Yang, L., van der Werf, K. O., Dijkstra, P. J., Feijen, J., and Bennink, M. L., 2012, “Micromechanical Analysis of Native and Cross-Linked Collagen Type I Fibrils Supports the Existence of Microfibrils,” J. Mech. Behav. Biomed. Mater., 6, pp. 148–158.

[44] Maas, S. A., Ellis, B. J., Ateshian, G. A., and Weiss, J. A., 2012, “FEBio: Finite Elements for Biomechanics,” J. Biomech. Eng., 134(1), p. 011005.

[45] Miller, G. J., and Morgan, E. F., 2010, “Use of Microindentation to Characterize the Mechanical Properties of Articular Cartilage: Comparison of Biphasic Material Properties across Length Scales,” Osteoarthr. Cartil. OARS Osteoarthr. Res. Soc., 18(8), pp. 1051–1057.

[46] Athanasiou, K. A., Rosenwasser, M. P., Buckwalter, J. A., Malinin, T. I., and Mow, V. C., 1991, “Interspecies Comparisons of in Situ Intrinsic Mechanical Properties of Distal Femoral Cartilage,” J. Orthop. Res., 9(3), pp. 330–340.

[47] Moore, A. C., DeLucca, J. F., Elliott, D. M., and Burris, D. L., 2016, “Quantifying Cartilage Contact Modulus, Tension Modulus, and Permeability with Hertzian Biphasic Creep,” J. Tribol., 138(4), pp. 041405–041405.

[48] Khayer Dastjerdi, A., and Barthelat, F., 2015, “Teleost Fish Scales amongst the Toughest Collagenous Materials,” J. Mech. Behav. Biomed. Mater., 52, pp. 95–107.

[49] Sasazaki, Y., Shore, R., and Seedhom, B. B., 2006, “Deformation and Failure of Cartilage in the Tensile Mode,” J. Anat., 208(6), pp. 681–694.

[50] Below, S., Arnoczky, S. P., Dodds, J., Kooima, C., and Walter, N., 2002, “The Split-Line Pattern of the Distal Femur: A Consideration in the Orientation of Autologous Cartilage Grafts,” Arthrosc. J. Arthrosc. Relat. Surg., 18(6), pp. 613–617.

[51]Liu, Y., Ballarini, R., and Eppell, S. J., 2016, “Tension Tests on Mammalian Collagen Fibrils,” Interface Focus, 6(1), p. 20150080.

[52] Gannon, A. R., Nagel, T., Bell, A. P., Avery, N. C., and Kelly, D. J., 2015, “Postnatal Changes to the Mechanical Properties of Articular Cartilage Are Driven by the Evolution of Its Collagen Network,” Eur. Cell. Mater., 29, pp. 105–121; discussion 121-123.

[53] Gao, L.-L., Zhang, C.-Q., Gao, H., Liu, Z.-D., and Xiao, P.-P., 2014, “Depth and Rate Dependent Mechanical Behaviors for Articular Cartilage: Experiments and Theoretical Predictions,” Mater. Sci. Eng. C, 38, pp. 244–251.

[54] Wahlquist, J. A., DelRio, F. W., Randolph, M. A., Aziz, A. H., Heveran, C. M., Bryant, S. J., Neu, C. P., and Ferguson, V. L., 2017, "Indentation Mapping Revealed Poroelastic, but Not Viscoelastic, Properties Spanning Native Zonal Articular Cartilage," Acta Biomater., 64, pp. 41–49.

[55] Buehler, M. J., 2006, "Atomistic and Continuum Modeling of Mechanical Properties of Collagen: Elasticity, Fracture, and Self-Assembly," J. Mater. Res., 21(8), pp. 1947–1961.

[56] Depalle, B., Qin, Z., Shefelbine, S. J., and Buehler, M. J., 2015, "Influence of Cross-Link Structure, Density and Mechanical Properties in the Mesoscale Deformation Mechanisms of Collagen Fibrils," J. Mech. Behav. Biomed. Mater., 52, pp. 1–13.

[57] Gupta, S., Lin, J., Ashby, P., and Pruitt, L., 2009, "A Fiber Reinforced Poroelastic Model of Nanoindentation of Porcine Costal Cartilage: A Combined Experimental and Finite Element Approach," J. Mech. Behav. Biomed. Mater., 2(4), pp. 326–338.

[58] Ateshian, G. A., 2009, "The Role of Interstitial Fluid Pressurization in Articular Cartilage Lubrication," J. Biomech., 42(9), pp. 1163–1176.

[59] Kumar, R., Grønhaug, K. M., Davies, C. L., Drogset, J. O., and Lilledahl, M. B., 2015, "Nonlinear Optical Microscopy of Early Stage (ICRS Grade-I) Osteoarthritic Human Cartilage," Biomed. Opt. Express, 6(5), pp. 1895–1903.

Chapter 5 Rate-dependent crack nucleation as function of matrix integrity*

Guebum Han, Uraching Chowdhury, Melih Eriten, and Corinne R. Henak

*(*Prepared for submission to a journal)*

5.1. Abstract

Articular cartilage can experience load-induced damage at any degenerative stage. However, the effects of solid matrix integrity and loading rates on cartilage failure are only partially understood. Thus, this paper examined rate-dependent crack nucleation as a function of cartilage integrity and its relation to relaxation mechanisms. Cartilage integrity was altered by enzymatically depleting glycosaminoglycans (GAGs). Localized crack nucleation was induced on intact and GAG-depleted cartilage at different loading rates via microindentation with an axisymmetric indenter. Relaxation responses of intact and GAG-depleted cartilage were measured with the identical indenter. Total work required for crack nucleation in GAG-depleted cartilage was higher than that in intact cartilage for all loading rates, and poroviscoelastic (PVE) relaxation of GAG-depleted cartilage were faster than those of intact cartilage. These results indicated that GAG depletion enabled cartilage to accommodate localized loading around the tip through relatively rapid PVE relaxations compared to intact cartilage, delayed crack nucleation at given loading rates. For both intact and GAG-depleted cartilage, total work required for crack nucleation sharply increased with decreasing loading rates. This result combined with the relaxation results suggested that cartilage near the crack tip had sufficient time to relax at relatively slow loading rates and eventually delayed crack nucleation in intact and GAG-depleted cartilage. In addition, crack shapes induced in a pre-relaxation timescale were distinct from those induced in a post-relaxation timescale, and their transition occurred in a transitional-relaxation timescale. Consistent crack shapes of intact cartilage generated under microindentation allowed the estimation of critical energy release rate (1.51 ± 0.63 to 1.60 ± 0.55 kJ/m^2). In summary, these results strongly indicated that rate-dependent crack nucleation is governed by the degree of PVE relaxation just prior to failure at given cartilage integrity and loading rates. These findings provide possible mechanisms underlying rate-dependent cartilage failure at different stages of degeneration.

Keywords Rate dependence; fracture; crack nucleation; glycosaminoglycan; poroviscoelasticity; articular cartilage

5.2. Introduction

Articular cartilage, a heterogeneous and dissipative material, exhibits impressive resistance to failure under a range of *in vivo* activities. Cartilage is composed of a tightly woven solid matrix hydrated by fluid. The solid matrix mainly consists of a collagen network (about 15-22 % of wet weight [1]) intertwined with proteoglycans (PGs) with sulfated glycosaminoglycan (GAG) side chains (about 4-7 % of wet weight [1]). Negatively charged GAGs generate swelling force via osmotic pressure and electrostatic repulsion between charges and thus provide compressive strength to cartilage [1,2]. A collagen network counterbalances the GAG-induced swelling force under tension [3–5]. Cohesive strength of cartilage mainly stems from a collagen network rather than PGs with GAGs [6–8]. While remarkable resistance of cartilage to failure protects the ends of bones in diarthrodial joints for decades of life, cartilage can undergo load-induced degeneration and injury [9,10]. Capacity of cartilage for self-repair is very limited [11] and cartilage may not effectively function as a loading-bearing and dissipative material after failure [12,13]. Therefore, understanding failure mechanisms of cartilage is important to prevent load-induced degeneration and injury of cartilage. Nevertheless, the onset of cartilage failure triggered by mechanical loading is incompletely understood.

In the sub-failure regime, rate-dependent mechanical behavior of cartilage originates from poroviscoelastic (PVE) relaxation and depends on solid matrix integrity. Poroelastic (PE) relaxation arises from drag generated by pressure-induced fluid flow in pore space and dissipates energy through frictional solid-fluid interactions (Lakes, 2009; Nia et al., 2011; Nia et al., 2015). Intrinsic viscoelastic (VE) relaxation occurs due to molecular rearrangement of a dense solid matrix [14,17,18]. PVE relaxation, which arises from the combination of the two, has been observed in cartilage sub-failure behavior. Solid matrix integrity governs PVE relaxations. For example, relaxation times of cartilage at small contact lengths (about 6 μm) was proportional to the square of a characteristic length, showing dominant PE relaxation in cartilage at microscale contact lengths [15]. GAG-depleted cartilage, simulating osteoarthritis-like cartilage, exhibited relaxation time shorter than intact cartilage, due to enlarged pore size after GAG depletion and subsequent increase in diffusivity [19–21]. Intrinsic VE relaxation dominated when applied loading rates were relatively faster than PE relaxation time [22,23]. At physiological loading frequencies (5 – 100 Hz), intrinsic VE relaxation formed the basis of dissipation, and PE relaxation additionally increased dissipation at small contact lengths [22]. Therefore, PVE dissipation mechanisms in cartilage can serve to protect joints across multiple length scales.

Conversely, little is known about effects of solid matrix integrity and PVE relaxation on rate-dependent cartilage failure. The undoubted rationale for understanding load-induced cartilage failure has attracted a few previous studies. For example, cartilage failure slowed down and occurred with necking phenomena under low-frequency tensile loading [24]. Large crack lengths and severe damage to microstructural features were induced under high-frequency compressive loading compared to low-frequency compressive loading [25,26]. Impact loading, simulating the onset of post-traumatic osteoarthritis, caused fissures and cracks [27–29]. Cartilage-on-cartilage fatigue loading caused softening accompanied with surface fibrillation [30]. Localized loading at different loading rates showed that crack nucleation in cartilage was rate-dependent [31,32]. In addition, nano/microscopic images of crack surfaces in cartilage showed that the solid matrix in the vicinity of localized loading underwent large relaxation and rearrangement at the slow loading rate compared to the fast loading rate, delaying crack nucleation [32]. Solid matrix alignment under loading was also observed in other collagen-rich tissues with ultrastructural similarities to cartilage. Their nano/microscopic images proved that applied loading caused straightening, stretching, sliding, and delamination of collagen fibers [33,34]. Tensile creep and uniaxial tension tests showed that PG extraction expedited reorganization and alignment of the collagen network, but did not influence failure strength of cartilage [7]; uniaxial tension tests were only performed at a slow constant rate. This indicated that cohesive strength of cartilage was dominantly governed by a collagen network [6–8]. Although previous studies describe rate-dependent cartilage failure, links between PVE relaxation and cartilage failure are incompletely established. Furthermore, rate-dependent cartilage failure as a function of solid matrix integrity has not been investigated. This is relevant because load-induced cartilage failure can be induced at different stages of cartilage integrity and loading rates [9,10].

To fill these gaps, the current study establishes a link between rate-dependent crack nucleation and relaxation mechanisms as a function of cartilage integrity. In particular, crack nucleation in intact and GAG-depleted cartilage is induced at multiple loading rates under microindentation. Microindentation with an axisymmetric tip can generate crack nucleation in hydrated cartilage at a well-defined location with smaller standard deviations in comparison to macroscopic testing [32,35]. These advantages allow effective investigation on effects of independent variables on dependent variables. Crack nucleation is identified as a sudden drop in load response, and critical load, displacement, and total work at that instance are reported for each test configuration. In addition, relaxation tests are performed on intact and GAG-depleted cartilage with the indenter used for crack nucleation tests. Cracks induced at different loading rates are imaged via an optical microscope. Experimental results suggest that rate-dependent crack nucleation in intact and GAG-depleted cartilage was governed by PVE relaxation.

5.3. Methods

5.3.1. Sample Preparation

Patellae of 20 porcine joints were harvested from a local abattoir (14 animals, 5-6 months old, sex unknown and assumed random) to prepare 100 full-thickness cartilage samples (Figure 5-1a). Six mm diameter cylindrical cores were obtained using a biopsy punch and a scalpel. A bottom surface parallel to an articular surface was created by eliminating subchondral bone with a microtome, allowing an indenter to be placed perpendicular to the articular surface. Half of the samples underwent GAG depletion prior to testing. GAG depletion was induced by incubating cartilage in 0.25% trypsin (Corning, Manassas, VA) at 37°C for 7 hours, resulting in selective digestion of GAG without affecting a collagen matrix [36,37].The bottom surface of each sample was fixed to a Petri dish using cyanoacrylate (Loctite 495, Henkel, Germany). Dulbecco's phosphate-buffered saline (DPBS) with protease inhibitor (PI) was used to keep samples hydrated during preparation and testing.

5.3.2. Microindentation-induced crack nucleation at multiple loading rates

Crack nucleation in intact and GAG-depleted cartilage was induced by performing microindentation tests at multiple loading rates. Tests were performed on a 3230-AT Series III test instrument (TA Instruments, New Castle, DE) with a diamond spherical-conical tip (tip radius, R = 100 μm and tip angle, θ = 90 degrees) (Anton Paar, Austria) (Figure 5-1a). Under displacement control, the articular surface of intact and GAG-depleted cartilage was indented at loading rates of 5, 0.5, 0.05, and 0.005 $mm{\cdot}s^{-1}$ while the load response was recorded. Those loading rates span pre- to post-relaxation timescales of intact and GAG-depleted cartilage. Rupture of intact and GAG-depleted cartilage was identified as a sudden drop in the measured load response (Figure 5-1b). In this study, the first detectable load drop with the current instrument was defined as major crack nucleation. Indentation displacement was prescribed based on preliminary data or manually terminated so that only a single crack was nucleated for all of the cases except for GAG-depleted cartilage at 5 $mm{\cdot}s^{-1}$ (Figure 5-1b). Maintaining single crack nucleation in GAG-depleted cartilage at 5 $mm{\cdot}s^{-1}$ failed because sequential crack events occurred randomly. Crack nucleation was quantified with critical load, L_c, displacement, D_c, and total work, W_c (Figure 5-1b). Critical total work was obtained from the integral of load-displacement curve from zero to critical displacement (trapezoidal integration, Origin 2018 (OriginLab, Northampton, MA)). Furthermore, the time required for crack nucleation was defined as critical time and determined by dividing critical displacement by corresponding loading rate. Ten tests for each loading rate were conducted at the center of 10 samples.

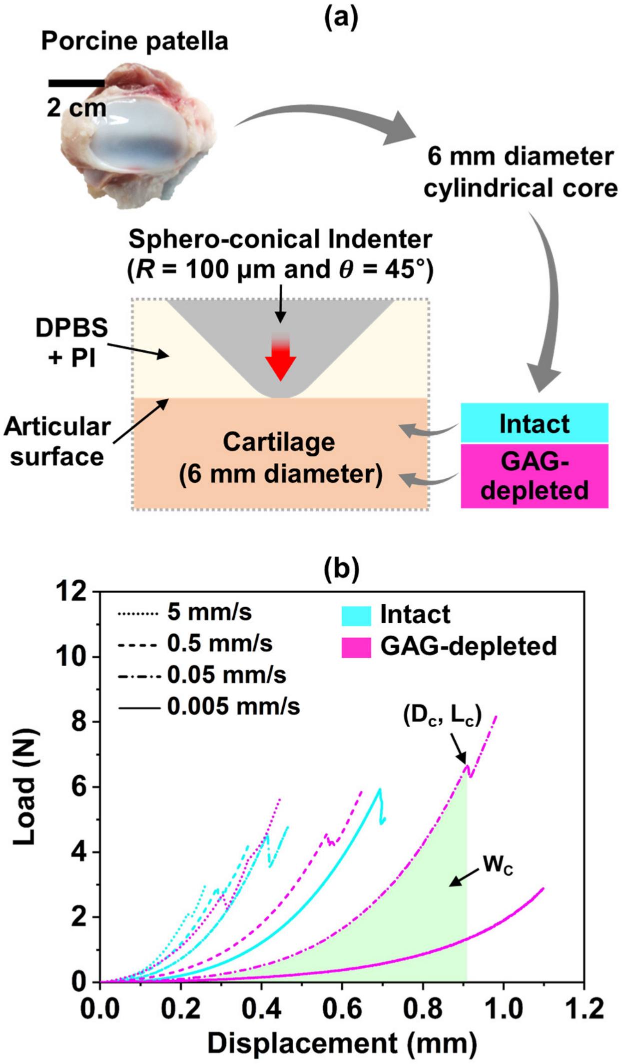

Figure 5-1: (a) Schematic diagram of sample preparation and experimental configuration and (b) representative load-displacement curves of crack nucleation tests on intact and GAG-depleted cartilage. The moment of crack nucleation was quantified with key parameters: critical displacement, D_c, critical load, L_c, and critical total work, W_c.

5.3.3. Relaxation responses

Relaxation responses of intact and GAG-depleted cartilage were measured by conducting indentation tests on articular surfaces. Tests were performed on the instrument with the sphero-conical indenter used for the crack nucleation tests. The indenter was moved down to a displacement of 0.3 mm (~18% of the average sample thickness) at a loading rate of 0.1 mm·s^{-1} then held for 200 s while load response was measured. GAG-depleted cartilage was prepared in the same way as that for crack nucleation tests. A total of 10 measurements for both intact and GAG-depleted cartilage were performed at the center of the samples; one location per sample was tested and 10 different samples were acquired from 10 different animals. Times required to reach 50, 70, and 90% of total relaxation were calculated from the results of the relaxation responses. The total relaxation was defined from maximum load to equilibrium load while the displacement was held constant. The equilibrium load was determined at 200 s of relaxation, beyond which load relaxation rates became negligibly small (~10^{-4} N·s^{-1}) compared to the initial rates (~1.5 N·s^{-1} for intact cartilage and ~0.6 N·s^{-1} for GAG-depleted cartilage).

5.3.4. Optical images of cracks

Cracks induced by microindentation tests were assessed through optical images. India ink was dropped on articular surface and gently wiped. Then a crack on the articular surface was imaged using a IX-71 inverted microscope (Olympus, Tokyo, Japan). Crack lengths and number of crack branches were measured manually using the segmented line tool in ImageJ (version 1.52a, National Institutes of Health). Each crack was measured three times and averaged to obtain the final crack length.

5.3.5. Statistical Analysis

The Kruskal-Wallis test was used to determine the dependence of crack nucleation results on loading rates, and relaxation time on relaxation degree. The Mann-Whitney U test was used to statistically compare experimental results from intact and GAG-depleted cartilage for each loading rate. All statistical analysis was performed using MATLAB (The MathWorks, Inc., Natick, MA). A significance level of 5% was used for all tests

5.4. Results

Loading rate and GAG depletion significantly affected critical load, critical displacement, and critical total work (Figure 5-2). For each loading rate, load responses of intact cartilage were higher than those of GAG-depleted cartilage (Figure 5-2a). Average load-displacement curves were acquired up to minimum critical displacements. However, the curve for GAG-depleted cartilage at 0.005 $mm \cdot s^{-1}$ was obtained up to the applied displacement as crack nucleation was not induced, and therefore its critical parameters were not obtained. Critical load of intact cartilage decreased as the loading rate increased ($p = 6.04 \times 10^{-8}$) (Figure 5-2b), and the value at 0.005 $mm \cdot s^{-1}$ (7.08 ± 0.97 N) was approximately 4 times higher on average than that at 5 $mm \cdot s^{-1}$ (1.86 ± 0.37 N). Critical load of GAG-depleted cartilage also decreased with increased loading rate ($p = 2.49 \times 10^{-6}$) (Figure 5-2b), and the value at 0.05 $mm \cdot s^{-1}$ (6.61 ± 0.96 N) was approximately 3 times higher on average than that at 5 $mm \cdot s^{-1}$ (2.46 ± 0.27 N). Critical load of GAG-depleted cartilage was approximately 30 - 45 % higher than that of intact cartilage at corresponding loading rates (5 - 0.05 $mm \cdot s^{-1}$, $p \leq 1.71 \times 10^{-3}$). Critical displacement of intact cartilage decreased with increasing loading rates ($p = 5.63 \times 10^{-8}$) (Figure 5-2c), and the value at 0.005 $mm \cdot s^{-1}$ (0.78 ± 0.07 mm) was nearly 4 times larger on average than that at 5 $mm \cdot s^{-1}$ (0.20 ± 0.02 mm). Likewise, critical displacement of GAG-depleted cartilage decreased nearly 3 times on average from 0.05 $mm \cdot s^{-1}$ (0.91 ± 0.06 mm) to 5 $mm \cdot s^{-1}$ (0.32 ± 0.03 mm) ($p = 2.49 \times 10^{-6}$) (Figure 5-2c). GAG depletion increased critical displacement by approximately 55 % - 100 % for all of the loading rates (5 - 0.05 $mm \cdot s^{-1}$, $p = 1.83 \times 10^{-4}$). Lastly, critical total work of intact cartilage sharply decreased as the loading rate increased ($p = 6.48 \times 10^{-8}$) (Figure 5-2d). The critical work at 0.005 $mm \cdot s^{-1}$ (1.41 ± 0.27 mJ) was nearly 11 times larger on average than that at 5 $mm \cdot s^{-1}$ (0.13 ± 0.04 mJ). Similarly, critical total work of GAG-depleted cartilage was rate-dependent ($p = 2.49 \times 10^{-6}$) and went down nearly 6 times from 0.05 mm·s^{-1} (1.42 ± 0.26 mJ) to 5 mm·s^{-1} (0.25 ± 0.04 mJ). GAG depletion increased total work required for crack nucleation by approximately 80 - 150 % across all of the loading rates (5 - 0.05 mm·s^{-1}, $p \leq 4.40 \times 10^{-4}$).

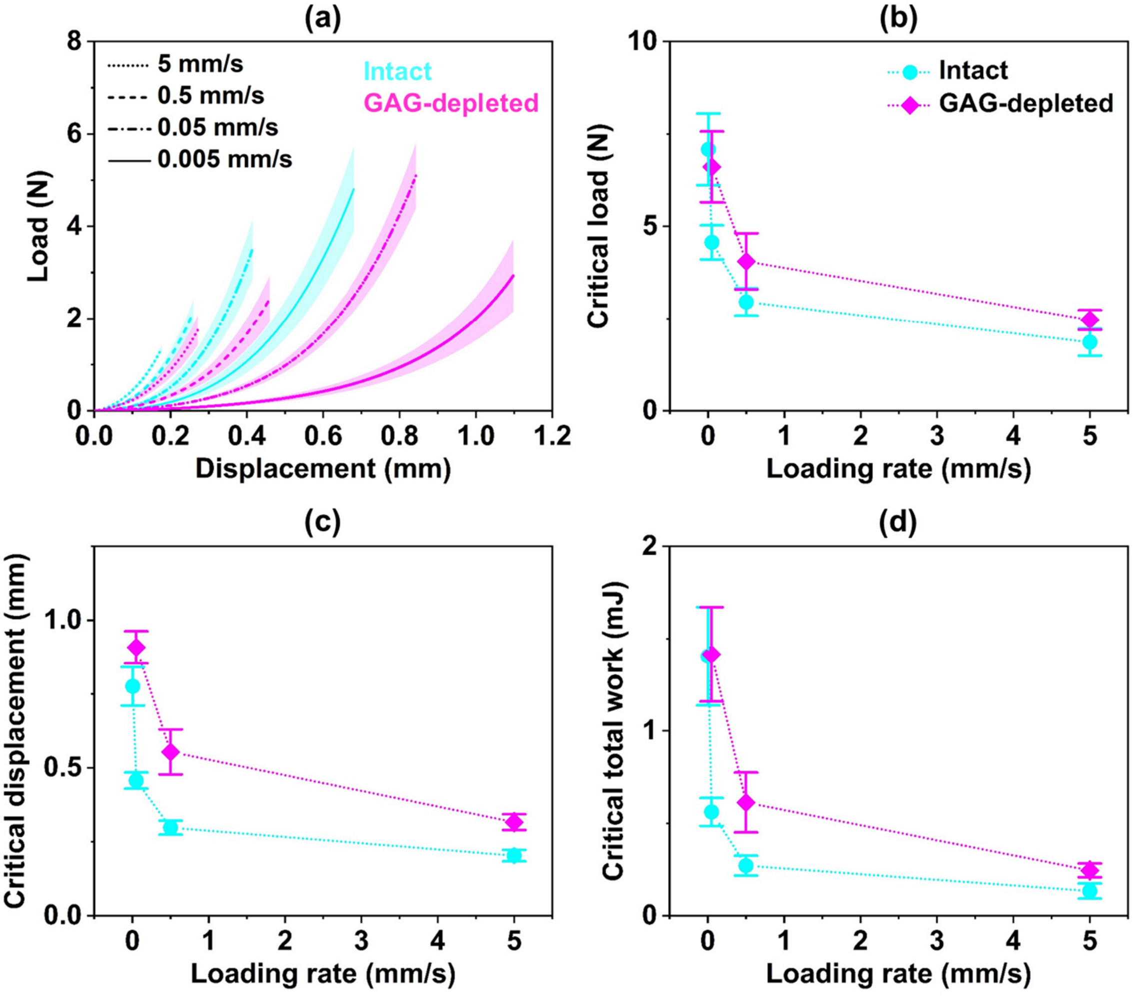

Figure 5-2: Results of crack nucleation tests: (a) average load-displacement curves prior to crack nucleation, (b) critical load, (c) critical displacement, and (d) critical total work. The average curves were obtained up to minimum critical displacement. However, the average curve for GAG-depleted cartilage at 0.005 mm·s^{-1} was up to the end of a prescribed displacement because crack nucleation did not occur at the maximum displacement allowed by the experimental setup.

Relaxation behavior of GAG-depleted cartilage was distinct from that of intact cartilage (Figure 5-3). The peak load of intact cartilage (2.12 ± 0.26 N) was nearly 6 times higher on average than that of GAG-depleted cartilage (0.33 ± 0.05 N) (Figure 5-3a). The equilibrium load of intact cartilage (0.18 ± 0.03 N) after 200 s was 9 times higher on average than that of GAG-depleted cartilage (0.02 ± 0.01 N) (Figure 5-3a). Intact cartilage relaxed faster than GAG-depleted cartilage (50 - 90 % of the total relaxation, $p \leq 1.01 \times 10^{-3}$) (Figure 5-3b). Relaxation time of intact cartilage was affected by relaxation degree; at 50, 70, and 90 % of the total relaxation was 1.29 ± 0.12 s, 3.18 ± 0.29 s, and 13.07 ± 1.17 s, respectively ($p = 2.49 \times 10^{-6}$). For GAG-depleted cartilage, relaxation time at 50, 70, and 90 % of the total relaxation corresponded to 0.47 ± 0.14 s, 1.40 ± 0.44 s, and 8.04 ± 2.74 s, respectively ($p = 2.49 \times 10^{-6}$).

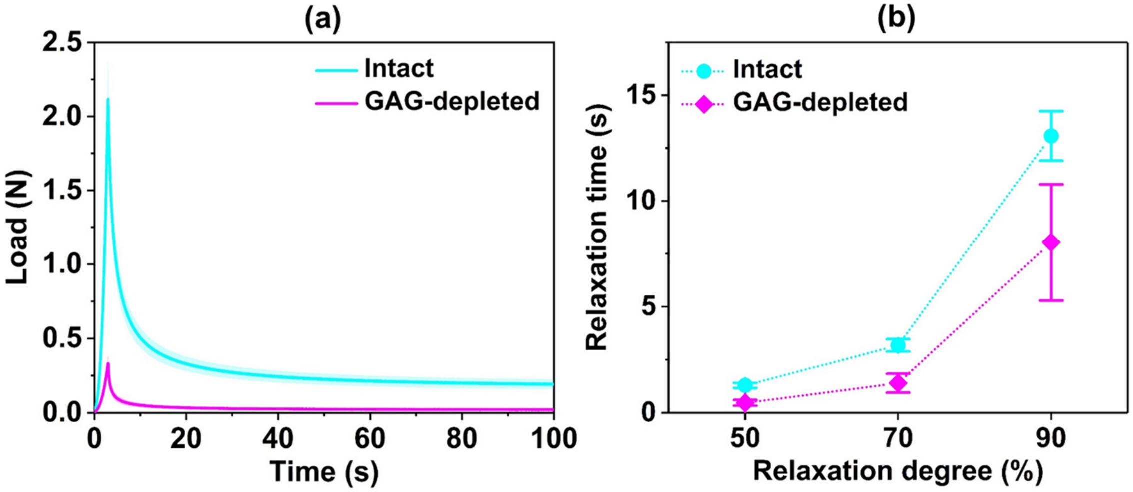

Figure 5-3: Results of relaxation tests: (a) average load-time relaxation curves and (b) relaxation times. Relaxation time was estimated at the points where relaxation reached 50, 70, and 90% of the total relaxation. The total relaxation was defined as the load relaxation from the peak load to the equilibrium load.

Crack nucleation in intact and GAG-depleted cartilage occurred across pre- and post-relaxation timescales (Figure 5-4). Critical time of intact and GAG-depleted cartilage decreased with increased loading rates ($p = 5.63 \times 10^{-8}$ for intact cartilage and $p = 2.49 \times 10^{-6}$ for GAG-depleted cartilage) (Figure 5-4a). Critical time of intact cartilage at 0.005 $mm \cdot s^{-1}$ (155.17 ± 13.04 s) was approximately 4000 times longer on average than that at 5 $mm \cdot s^{-1}$ (0.04 ± 0.004 s). Critical time of GAG-depleted cartilage at 0.05 $mm \cdot s^{-1}$ (18.16 ± 1.09 s) was approximately 300 times longer on average than that at 5 $mm \cdot s^{-1}$ (0.06 ± 0.005 s).

Critical total work plotted as a function of critical time and compared with relaxation time indicated a link between rate-dependent crack nucleation and relaxation timescales (Figure 5-4b). As for intact cartilage, critical time at 5 $mm \cdot s^{-1}$ and 0.5 $mm \cdot s^{-1}$ was shorter than relaxation time and thus were located in a pre-relaxation timescale. Conversely, critical time at 0.05 $mm \cdot s^{-1}$ and 0.005 $mm \cdot s^{-1}$ belonged to transitional- and post-relaxation timescales, respectively. In the case of GAG-depleted cartilage, critical time at 5 $mm \cdot s^{-1}$ was shorter than relaxation time and therefore corresponded to a pre-relaxation timescale. Critical time at 0.5 $mm \cdot s^{-1}$ and 0.05 $mm \cdot s^{-1}$ was within transitional- and post-relaxation timescales. Critical total work combined with the comparison between critical time and relaxation time allowed estimation of relaxation degrees just prior to crack nucleation. For both intact and GAG-depleted cartilage, critical total work were the smallest in a pre-relaxation timescale and sharply increased toward a post-relaxation timescale (Figure 5-4b).

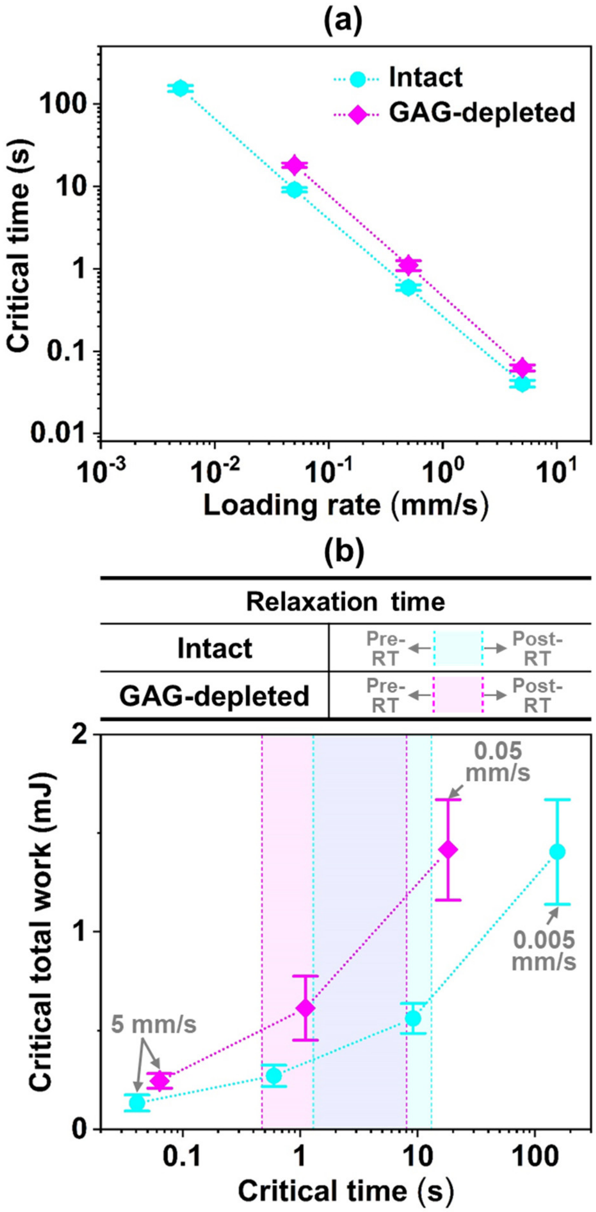

Figure 5-4: (a) Critical time and (b) critical total work as function of critical time with relaxation time (RT) overlaid. Critical time was defined as the time required for crack nucleation and calculated by dividing critical displacement by loading rates (Figure 5-2c). A range of RT from Figure 5-3b was plotted.

Optical images of cracks showed a transition in shapes from fast loading to slow loading (Figure 5-5). Images suggested that cracks were created by opening a dense solid matrix swollen by fluid (Figure 5-5a). For GAG-depleted cartilage loaded at 0.005 $mm \cdot s^{-1}$, no evidence of crack nucleation was observed, consistent with the results of crack nucleation tests (i.e., no sudden drop in load response). For intact cartilage, the number of branches increased with increasing loading rates from 2 at 5 $mm \cdot s^{-1}$ to 3 at 0.005 $mm \cdot s^{-1}$ ($p = 2.01 \times 10^{-6}$) (Figure 5-5b). Crack lengths increased from 430 ± 60 µm at 5 $mm \cdot s^{-1}$ to 865 ± 155 µm at 0.005 $mm \cdot s^{-1}$ ($p = 7.12 \times 10^{-7}$) (Figure 5-5c); the maximum crack length of 990 ± 175 µm was observed at 0.05 $mm \cdot s^{-1}$. Similarly, the number of branches induced in GAG-depleted cartilage increased from 2 at 5 $mm \cdot s^{-1}$ to 3 at 0.05 $mm \cdot s^{-1}$ ($p = 5.33 \times 10^{-5}$) (Figure 5-5b). Crack lengths were rate-dependent ($p = 1.20 \times 10^{-3}$) and slightly increased from 715 ± 135 µm at 5 $mm \cdot s^{-1}$ to 750 ± 190 µm at 0.05 $mm \cdot s^{-1}$ (Figure 5-5c); the maximum crack length was 1060 ± 215 µm at 0.5 $mm \cdot s^{-1}$. In order to investigate the relationship between rate-dependent crack morphological features and relaxation timescales, the number of branches and crack lengths in intact and GAG-depleted cartilage were plotted as a function of critical time with relaxation time (Figure 5-5b and c). Cracks at the fast (5$mm \cdot s^{-1}$ and 0.5 $mm \cdot s^{-1}$ for intact and 5 $mm \cdot s^{-1}$ for GAG-depleted) and slow (0.005 $mm \cdot s^{-1}$ for intact and 0.05 $mm \cdot s^{-1}$ for GAG-depleted) loading rates were generated in pre- and post-relaxation timescales, and their transitional periods matched the relaxation time.

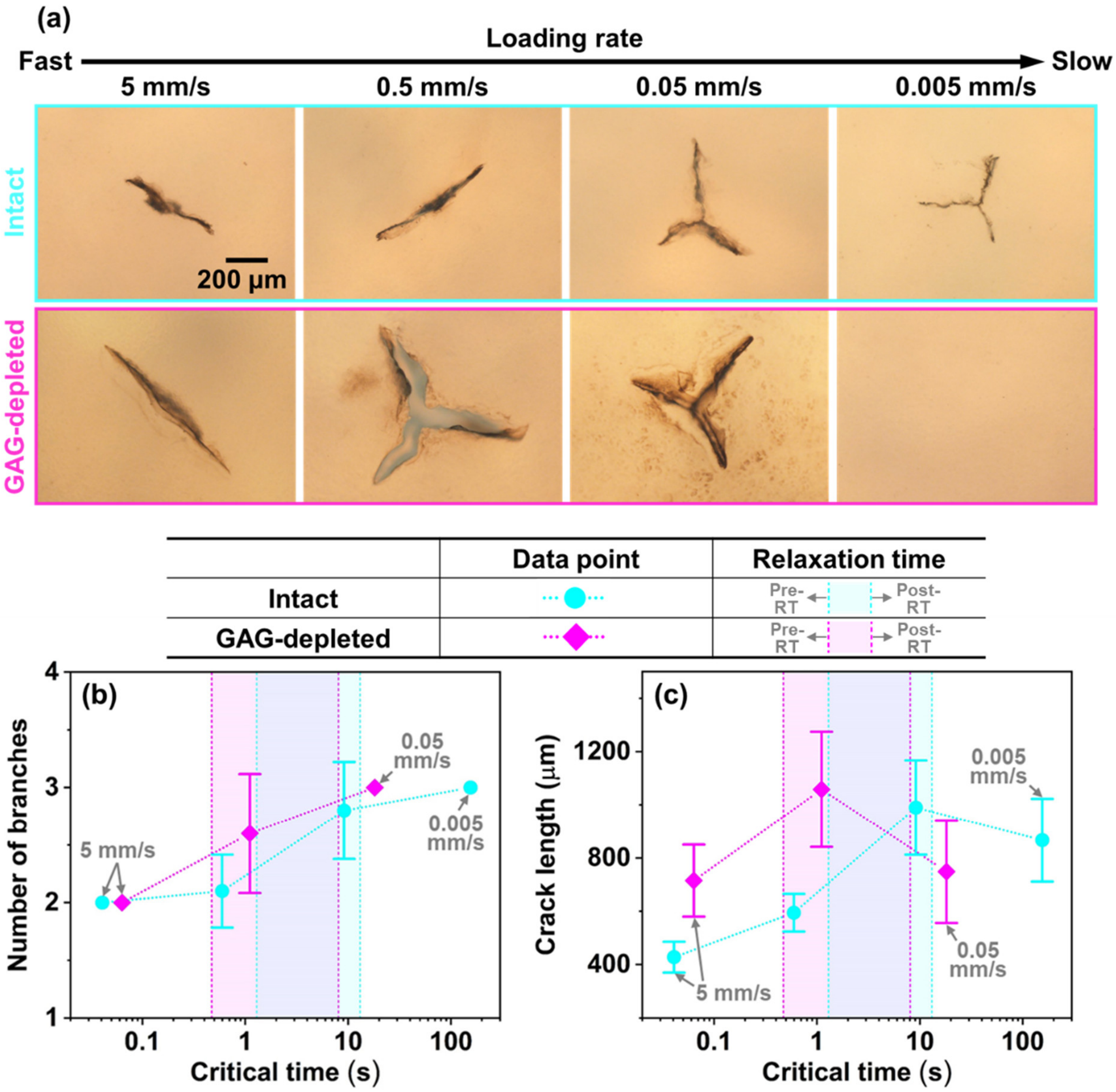

Figure 5-5: (a) Representative optical images of cracks, (b) number of crack branches, and (c) crack lengths. The scale bar in (a) is applied to all the images. The number of branches for a line-shaped crack was counted as two branches. A range of relaxation time (RT) in (c) was estimated from the relaxation tests (Figure 5-3b).

5.5. Discussion

Solid matrix integrity had a dramatic impact on crack nucleation, with GAG depletion causing delayed crack nucleation. Crack nucleation in intact cartilage required less critical total work than that in GAG-depleted cartilage (Figure 5-2d). GAG-depleted cartilage could accommodate the localized loading by the indenter tip at given loading rates more rapidly than intact cartilage could, and this leads to the enhanced resistance to crack nucleation. A significant decrease in relaxation time of cartilage after GAG depletion (Figure 5-3b) showed that the rearrangement of the solid matrix (VE relaxation) and fluid diffusion (PE relaxation) occurred faster in GAG-depleted cartilage compared to intact cartilage. Creep tests under tension also observed the enhanced capacity of the solid matrix realignment after PG extraction [7]. The decreased PVE relaxation times was mainly due to the altered PE relaxation because trypsin selectively depletes GAG without affecting a collagen matrix [36,37]; previous studies showed that GAG depletion increased pore size of cartilage from 2-11 nm to 14 nm [1,19], resulting in higher permeability and therefore shorter PE relaxation [20,21]. Our recent study on cartilage failure under microindentation suggested that tensile stresses built up in intact cartilage underneath the indenter tip and governed rate-dependent crack nucleation [32]. Consequently, the current findings combined with previous studies suggest that GAG depletion improved the ability to accommodate localized stress at the tip by rapidly rearranging the solid matrix (i.e., collagen fibrils) at given loading rates compared to intact cartilage, ultimately delaying crack nucleation. Effects of GAG depletion on failure strength were expected to be minor. This can be underpinned from previous studies showing that cohesive strength of intact cartilage mainly stems from collagen fibrils rather than PGs-based interactions [6–8] and extraction of PGs did not affected failure strength of cartilage [7].

Crack nucleation in intact and GAG-depleted cartilage was rate-dependent and was governed by the degree of relaxation, suggesting an apparent transition from ductile-like failure at slow loading rates to brittle-like failure at fast loading rates. In particular, crack nucleation at relatively fast loading rates required much less work than that at relatively slow loading rates (Figure 5-4). Intact cartilage at 5 and 0.5 $mm{\cdot}s^{-1}$ did not have sufficient time to relax before crack nucleation as the critical time was much shorter than PVE relaxation time (Figure 5-4b). Conversely, intact cartilage at 0.005 $mm{\cdot}s^{-1}$ had sufficient time to undergo relaxation prior to crack nucleation because the critical time was much longer than PVE relaxation time (Figure 5-4b). Similarly, crack nucleation in GAG-depleted cartilage at 5 $mm{\cdot}s^{-1}$ and 0.05 $mm{\cdot}s^{-1}$ occurred in its pre- and post-relaxation timescales (Figure 5-4b), respectively, and thus GAG-depleted cartilage sufficiently underwent PVE relaxation at 0.05 $mm{\cdot}s^{-1}$, but not 5 $mm{\cdot}s^{-1}$. These results suggested that total work for crack nucleation was relatively larger in a post-relaxation timescale compared to in a pre-relaxation timescale because a substantial amount of total work dissipated during load-induced deformation rather than crack nucleation. In a nutshell, it can be concluded that rate-dependent resistance of intact and GAG-depleted cartilage to crack nucleation originated from the degree of PVE relaxation (solid matrix realignment and fluid diffusion) in the vicinity of the tip prior to failure and a large amount of PVE relaxation delayed crack nucleation. In addition, the decreasing difference in critical total work between intact and GAG-depleted cartilage toward fast loading rates implied that the effect of GAG depletion on crack nucleation became weaker in a pre-relaxation timescale (Figure 5-4b).

Distinct crack morphology occurred with loading rates and GAG depletion. These features reiterated that the degree of relaxation governed crack nucleation. For both intact and GAG-depleted cartilage, the number of crack branches depended on the degree of relaxation at a given loading rate (Figure 5-5a and b). When cracks were generated in a pre-relaxation timescale, the number of crack branches was consistently two (line shape). In contrast, when cracks were induced in a post-relaxation timescale, the number of crack branches was consistently three (star shape). Interestingly, a transition in the number of branches occurred in a transitional-relaxation timescale when critical time matched relaxation time. The distinct crack morphology according to relaxation zones could imply that the degree of PVE relaxation contributed to rate-dependent crack nucleation. In addition, crack lengths also depended on the degree of relaxation (Figure 5-5a and d). The crack lengths of intact and GAG-depleted cartilage were the minimum in a pre-relaxation timescale; 90 % of GAG-depleted cartilage in a pre-relaxation timescale (5 $\mathrm{mm \cdot s^{-1}}$) underwent at least two crack nucleation events based on sudden changes in load-displacement curves and therefore its crack lengths might be overestimated, but other cracks were generated by a single crack nucleation event. For both intact and GAG-depleted cartilage, the maximum crack lengths occurred in a transitional-relaxation timescale (Figure 5-1c), implying that load-induced surface damage could be severe when critical time is comparable to relaxation time of cartilage at different levels of solid matrix integrity. Lastly, the consistent line shapes of cracks in intact cartilage in a pre-relaxation timescale (5 and 0.5 $\mathrm{mm \cdot s^{-1}}$) allowed the measurement of critical energy release rate via a model for sharp-tipped punch penetration [38,39]; the detailed information is given in Appendix B. The estimated critical energy release rate of intact cartilage was 1.51 ± 0.63 to 1.60 ± 0.55 $\mathrm{kJ/m^2}$ (5 - 0.5 $\mathrm{mm \cdot s^{-1}}$) and was consistent with the upper bound of previously reported values for cartilage (0.14±0.08 - 1.46±0.91 $\mathrm{kJ/m^2}$ [40], 0.83±0.19 - 1.12±0.2 $\mathrm{kJ/m^2}$ [35], and 0.8±1.05 - 1.17±1.13 $\mathrm{kJ/m^2}$ [41]); the discrepancies could be due to species, age, and test configurations. This suggested that microindentation-based crack nucleation tests could be useful to estimate the critical energy release rate of a small volume of soft hydrated materials.

This study filled gaps in knowledge related to the link between cartilage failure and PVE relaxation, but limitations should be explored further. The experimental conditions did not match *in vivo* conditions; however, a geometrically well-defined microscale tip induced localized crack nucleation at a known location, allowing for efficient investigation of rate-dependent crack nucleation in intact and GAG-depleted cartilage. This can extend our understanding of rate-dependent cartilage failure under physiological loading rates. Bulk strain rates of intact and GAG-depleted cartilage at the fast loading rate ($5\ mm{\cdot}s^{-1}$) were $3.35 \pm 0.25\ s^{-1}$ and $3.29 \pm 0.21\ s^{-1}$, respectively, and fall within the lower bound of the strain rates during walking, jumping, and running [20,42,43]. Bulk strain rates of intact ($0.005\ mm{\cdot}s^{-1}$) and GAG-depleted ($0.05\ mm{\cdot}s^{-1}$) cartilage at the slow loading rates were $0.0032 \pm 0.0003\ s^{-1}$ and $0.032 \pm 0.029\ s^{-1}$, respectively, and could represent human resting. Bulk strain rates were estimated by dividing the ratio of critical displacement to thickness by critical time. Minor cracks in the initial stages of indentation might not be captured due to the noise floor in the load cell. These minor cracks are expected to have a crack length of ≤100 μm, considering the rigid kinematic constraint imposed by the indenter tip. As cartilage is a hydrated material, the identification of these minor cracks with an optical microscope is challenging. In this sense, crack nucleation investigated in this study was defined as a major crack nucleation event which was detected with the current instrument. In order to distinguish between minor and major crack nucleation events, experimental instruments with higher force and displacement resolutions are required. Cartilage integrity was changed by depleting GAGs via trypsin digestion, and thus the current findings do not represent the influence of other solid matrix components (e.g., collagen fibrils) on rate-dependent crack nucleation.

5.6. Conclusions

This work examined a link between rate-dependent crack nucleation and PVE relaxation as a function of cartilage integrity. An axisymmetric micro-indenter effectively generated rate-dependent crack nucleation in intact and GAG-depleted cartilage at known locations from pre- to post-relaxation timescales. Rate-dependent crack nucleation was governed by the degree of PVE relaxation at given cartilage integrity and loading rates. The degeneration of solid matrix integrity by GAG depletion significantly decreased relaxation time and increased critical total work for cartilage failure. These results indicated that GAG depletion enhanced the capacity of kinematic fibril rearrangement and fluid diffusion at given loading rates and thus delayed rupture of a collagen network and crack nucleation. For both intact and GAG-depleted cartilage, crack nucleation at the fast and slow loading rates occurred in pre- and post-relaxation timescales, respectively, and total work for crack nucleation rapidly increased toward a post-relaxation timescale. These results showed that cartilage in the vicinity of the tip experienced relatively large PVE relaxation, accompanying with kinematic fibril rearrangement and fluid diffusion, at the slow loading rate, resulting in delayed crack nucleation. The strong dependence of rate-dependent crack morphology on the degree of relaxation before failure provided further evidence for relaxation-governed rate-dependent crack nucleation in intact and GAG-depleted cartilage. Consistent crack shapes showed a promising aspect of microindentation-based crack nucleation testing for measuring critical energy release rate of soft hydrated materials. These findings underlined the importance of PVE relaxation mechanisms in rate-dependent cartilage failure at different stages of degeneration, extending our understanding of the onset of load-induced cartilage damage. Also, they could be useful information for designing cartilage-like tough and dissipative materials.

5.7. Acknowledgment

We gratefully acknowledge funding from the National Science Foundation (CMMI-DCSD-1662456).

5.8. References

[1] Mow, V. C., Ratcliffe, A., and Robin Poole, A., 1992, “Cartilage and Diarthrodial Joints as Paradigms for Hierarchical Materials and Structures,” Biomaterials, 13(2), pp. 67–97.

[2] Han, E., Chen, S. S., Klisch, S. M., and Sah, R. L., 2011, “Contribution of Proteoglycan Osmotic Swelling Pressure to the Compressive Properties of Articular Cartilage,” Biophys. J., 101(4), pp. 916–924.

[3] Kempson, G. E., Freeman, M. a. R., and Swanson, S. a. V., 1968, “Tensile Properties of Articular Cartilage,” Nature, 220(5172), pp. 1127–1128.

[4] Andriotis, O. G., Desissaire, S., and Thurner, P. J., 2018, “Collagen Fibrils: Nature’s Highly Tunable Nonlinear Springs,” ACS Nano, 12(4), pp. 3671–3680.

[5] Soulhat, J., Buschmann, M. D., and Shirazi-Adl, A., 1999, “A Fibril-Network-Reinforced Biphasic Model of Cartilage in Unconfined Compression,” J. Biomech. Eng., 121(3), pp. 340–347.

[6] Broom, N. D., and Silyn-Roberts, H., 1990, “Collagen-Collagen versus Collagen-Proteoglycan Interactions in the Determination of Cartilage Strength,” Arthritis Rheum., 33(10), pp. 1512–1517.

[7] Schmidt, M. B., Mow, V. C., Chun, L. E., and Eyre, D. R., 1990, “Effects of Proteoglycan Extraction on the Tensile Behavior of Articular Cartilage,” J. Orthop. Res. Off. Publ. Orthop. Res. Soc., 8(3), pp. 353–363.

[8] Zhu, W., Iatridis, J. C., Hlibczuk, V., Ratcliffe, A., and Mow, V. C., 1996, “Determination of Collagen-Proteoglycan Interactions in Vitro,” J. Biomech., 29(6), pp. 773–783.

[9] Buckwalter, J. A., 1992, “Mechanical Injuries of Articular Cartilage,” Iowa Orthop. J., 12, pp. 50–57.

[10] Simon, T. M., and Jackson, D. W., 2018, “Articular Cartilage: Injury Pathways and Treatment Options,” Sports Med. Arthrosc. Rev., 26(1), pp. 31–39.

[11] Cheng, A., Hardingham, T. E., and Kimber, S. J., 2014, “Generating Cartilage Repair from Pluripotent Stem Cells.,” Tissue Eng. Part B Rev., 20(4), pp. 257–266.

[12] Pritzker, K. P. H., Gay, S., Jimenez, S. A., Ostergaard, K., Pelletier, J.-P., Revell, P. A., Salter, D., and van den Berg, W. B., 2006, "Osteoarthritis Cartilage Histopathology: Grading and Staging.," Osteoarthr. Cartil. OARS Osteoarthr. Res. Soc., 14(1), pp. 13–29.

[13] Bauer, M., and Jackson, R. W., 1988, "Chondral Lesions of the Femoral Condyles: A System of Arthroscopic Classification," Arthrosc. J. Arthrosc. Relat. Surg., 4(2), pp. 97–102.

[14] Lakes, P. R., 2009, *Viscoelastic Materials*, Cambridge University Press, Cambridge ; New York.

[15] Nia, H., Han, L., Li, Y., Ortiz, C., and Grodzinsky, A., 2011, "Poroelasticity of Cartilage at the Nanoscale," Biophys. J., 101(9), pp. 2304–2313.

[16] Nia, H., Han, L., Soltani Bozchalooi, I., Roughley, P., Youcef-Toumi, K., Grodzinsky, A. J., and Ortiz, C., 2015, "Aggrecan Nanoscale Solid–Fluid Interactions Are a Primary Determinant of Cartilage Dynamic Mechanical Properties," ACS Nano, 9(3), pp. 2614–2625.

[17] Huang, C.-Y., Soltz, M. A., Kopacz, M., Mow, V. C., and Ateshian, G. A., 2003, "Experimental Verification of the Roles of Intrinsic Matrix Viscoelasticity and Tension-Compression Nonlinearity in the Biphasic Response of Cartilage," J. Biomech. Eng., 125(1), pp. 84–93.

[18] Mak, A. F., 1986, "The Apparent Viscoelastic Behavior of Articular Cartilage—The Contributions from the Intrinsic Matrix Viscoelasticity and Interstitial Fluid Flows," J. Biomech. Eng., 108(2), pp. 123–130.

[19] Majda, D., Bhattarai, A., Riikonen, J., Napruszewska, B. D., Zimowska, M., Michalik-Zym, A., Töyräs, J., and Lehto, V.-P., 2017, "New Approach for Determining Cartilage Pore Size Distribution: NaCl-Thermoporometry," Microporous Mesoporous Mater., 241, pp. 238–245.

[20] Nia, H., Bozchalooi, I. S., Li, Y., Han, L., Hung, H.-H., Frank, E., Youcef-Toumi, K., Ortiz, C., and Grodzinsky, A., 2013, "High-Bandwidth AFM-Based Rheology Reveals That Cartilage Is Most Sensitive to High Loading Rates at Early Stages of Impairment," Biophys. J., 104(7), pp. 1529–1537.

[21] Wahlquist, J. A., DelRio, F. W., Randolph, M. A., Aziz, A. H., Heveran, C. M., Bryant, S. J., Neu, C. P., and Ferguson, V. L., 2017, "Indentation Mapping Revealed Poroelastic, but Not Viscoelastic, Properties Spanning Native Zonal Articular Cartilage," Acta Biomater., 64, pp. 41–49.

[22] Han, G., Hess, C., Eriten, M., and Henak, C. R., 2018, "Uncoupled Poroelastic and Intrinsic Viscoelastic Dissipation in Cartilage," J. Mech. Behav. Biomed. Mater., 84, pp. 28–34.

[23] Quinn, T. M., Allen, R. G., Schalet, B. J., Perumbuli, P., and Hunziker, E. B., 2001, "Matrix and Cell Injury Due to Sub-Impact Loading of Adult Bovine Articular Cartilage Explants: Effects of Strain Rate and Peak Stress," J. Orthop. Res., 19(2), pp. 242–249.

[24] Sadeghi, H., Lawless, B. M., Espino, D. M., and Shepherd, D. E. T., 2018, “Effect of Frequency on Crack Growth in Articular Cartilage,” J. Mech. Behav. Biomed. Mater., 77(May 2017), pp. 40–46.

[25] Kaplan, J. T., Neu, C. P., Drissi, H., Emery, N. C., and Pierce, D. M., 2017, “Cyclic Loading of Human Articular Cartilage: The Transition from Compaction to Fatigue,” J. Mech. Behav. Biomed. Mater., 65, pp. 734–742.

[26] Sadeghi, H., Shepherd, D. E. T., and Espino, D. M., 2015, “Effect of the Variation of Loading Frequency on Surface Failure of Bovine Articular Cartilage,” Osteoarthritis Cartilage, 23(12), pp. 2252–2258.

[27] Kaleem, B., Maier, F., Drissi, H., and Pierce, D. M., 2017, “Low-Energy Impact of Human Cartilage: Predictors for Microcracking the Network of Collagen,” Osteoarthritis Cartilage, 25(4), pp. 544–553.

[28] Su, A. W., Chen, Y., Dong, Y., Wailes, D. H., Wong, V. W., Chen, A. C., Cai, S., Bugbee, W. D., and Sah, R. L., 2018, “Biomechanics of Osteochondral Impact with Cushioning and Graft Insertion: Cartilage Damage Is Correlated with Delivered Energy,” J. Biomech., 73, pp. 127–136.

[29] Henak, C. R., Bartell, L. R., Cohen, I., and Bonassar, L. J., 2017, “Multiscale Strain as a Predictor of Impact-Induced Fissuring in Articular Cartilage,” J. Biomech. Eng., 139(3), p. 031004.

[30] Vazquez, K. J., Andreae, J. T., and Henak, C. R., 2019, “Cartilage-on-Cartilage Cyclic Loading Induces Mechanical and Structural Damage,” J. Mech. Behav. Biomed. Mater., 98, pp. 262–267.

[31] Bartell, L. R., Xu, M. C., Bonassar, L. J., and Cohen, I., 2018, “Local and Global Measurements Show That Damage Initiation in Articular Cartilage Is Inhibited by the Surface Layer and Has Significant Rate Dependence,” J. Biomech.

[32] Han, G., Eriten, M., and Henak, C. R., 2019, “Rate-Dependent Crack Nucleation in Cartilage under Microindentation,” J. Mech. Behav. Biomed. Mater., 96, pp. 186–192.

[33] Bircher, K., Zündel, M., Pensalfini, M., Ehret, A. E., and Mazza, E., 2019, “Tear Resistance of Soft Collagenous Tissues,” Nat. Commun., 10(1), p. 792.

[34] Yang, W., Sherman, V. R., Gludovatz, B., Schaible, E., Stewart, P., Ritchie, R. O., and Meyers, M. A., 2015, “On the Tear Resistance of Skin,” Nat. Commun., 6, p. 6649.

[35] Simha, N. K., Carlson, C. S., and Lewis, J. L., 2004, “Evaluation of Fracture Toughness of Cartilage by Micropenetration,” J. Mater. Sci. Mater. Med., 15(5), pp. 631–639.

[36] Griffin, D. J., Vicari, J., Buckley, M. R., Silverberg, J. L., Cohen, I., and Bonassar, L. J., 2014, "Effects of Enzymatic Treatments on the Depth-Dependent Viscoelastic Shear Properties of Articular Cartilage," J. Orthop. Res., 32(12), pp. 1652–1657.

[37] Nguyen, Q., Murphy, G., Roughley, P. J., and Mort, J. S., 1989, "Degradation of Proteoglycan Aggregate by a Cartilage Metalloproteinase. Evidence for the Involvement of Stromelysin in the Generation of Link Protein Heterogeneity in Situ.," Biochem. J., 259(1), pp. 61–67.

[38] Shergold, O. A., and Fleck, N. A., 2005, "Experimental Investigation Into the Deep Penetration of Soft Solids by Sharp and Blunt Punches, With Application to the Piercing of Skin," J. Biomech. Eng., 127(5), pp. 838–848.

[39] Shergold, O. A., and Fleck, N. A., 2004, "Mechanisms of Deep Penetration of Soft Solids, with Application to the Injection and Wounding of Skin," Proc. R. Soc. Lond. Ser. Math. Phys. Eng. Sci., 460(2050), pp. 3037–3058.

[40] Chin-Purcell, M. V., and Lewis, J. L., 1996, "Fracture of Articular Cartilage," J. Biomech. Eng., 118(4), pp. 545–556.

[41] Adams, D. J., Brosche, K. M., and Lewis, J. L., 1999, "Factors Affecting Fracture Parameters for Articular Cartilage," 45th Annu. Meet. Orthop. Res. Soc., pp. 1–4.

[42] Deneweth, J. M., Newman, K. E., Sylvia, S. M., McLean, S. G., and Arruda, E. M., 2013, "Heterogeneity of Tibial Plateau Cartilage in Response to a Physiological Compressive Strain Rate," J. Orthop. Res., 31(3), pp. 370–375.

[43] Liu, F., Kozanek, M., Hosseini, A., Van de Velde, S. K., Gill, T. J., Rubash, H. E., and Li, G., 2010, "In Vivo Tibiofemoral Cartilage Deformation during the Stance Phase of Gait," J. Biomech., 43(4), pp. 658–665.

Chapter 6 Conclusions

6.1. Conclusions and future work

The overall objectives of this dissertation were to examine fundamental mechanisms of broadband cartilage dissipation (≥ 5 degree phase shift) and to establish the links between rate-dependent cartilage failure and dissipation mechanisms. These objectives were accomplished by performing mechanical testing across multiple length- (μm to mm) and time- (quasi-static to traumatic impact) scales combined with finite element (FE) modeling and nano/microscale imaging techniques.

Underlying mechanisms of cartilage dissipation were studied by conducting dynamic testing at multiple length scales over physiological loading frequencies (5-100 Hz) (*Chapter 2*). Poroelastic (PE) and viscoelastic (VE) dissipation mechanisms were uncoupled using dependence of PE relaxation on characteristic lengths in the frequency of interest. The uncoupled dissipation mechanisms revealed that intrinsic VE dissipation was responsible for the basis of dissipation and PE dissipation additionally increased overall dissipation at relatively small characteristic lengths. In addition, this suggested that VE dissipation became dominant at a contact length of ≥30 - 45 μm in the frequency range of 5 - 100 Hz. A considerable decrease in energy dissipation after dehydration indicated that hydration was critical in both PE and intrinsic VE-related dissipation. These findings provide possible mechanisms underlying broadband cartilage dissipation. The experimentally-confirmed dependence of cartilage dissipation mechanisms on characteristic lengths provides design parameters for cartilage-like broadband dampers [1,2].

Macroscopic dissipative and mechanical responses as a function of cartilage integrity were investigated under high-frequency loading (up to 300 Hz) to explore previously unexamined traumatic scenarios at in vivo length scales (*Chapter 3*). Different degrees of cartilage integrity were obtained by depleting glycosaminoglycan (GAG) via trypsin treatment. Energy dissipation of cartilage increased with the solid matrix degeneration under high-frequency loading simulating traumatic impact and heel strike. Significant decreases in relaxation times after GAG depletion suggested that the increased dissipation under high-frequency loading originated from changed PE dissipation. These findings fill gaps in fundamental dissipative properties of cartilage and therefore provide a basis for understanding cartilage dissipation as a function of solid matrix integrity under traumatic injury and high-rate physiological loading.

Rate-dependent crack nucleation in cartilage was investigated with nano/microscopic images of crack surfaces and a poroviscoelastic (PVE) FE model (*Chapter 4*). A microscale sphero-conical indenter effectively generated localized cracks at two extreme loading rates; while the slow loading rate induced strain rates corresponding to human resting, the fast loading rate induced strain rates corresponding to walking, jumping, and running. Microindentation results combined with FE modeling indicated that VE relaxation with minor effects of PE relaxation governed rate-dependent crack nucleation in cartilage and tensile stresses at the end of the tip initiated cartilage failure. The rate-dependent morphological features of crack surfaces showed that the solid matrix around the tip underwent relatively large relaxation (realignment of collagen fibrils) at the slow loading rate in comparison to the fast loading rate, leading to delayed cartilage failure. These findings provide evidence of the link between rate-dependent cartilage failure and physical mechanisms. Therefore, they also imply that the PE and VE mechanisms play an important role in rate-dependent cartilage failure (*Chapter 4*) in addition to rate-dependent cartilage behavior in the sub-failure regime (*Chapters 2 and 3*).

Lastly, the missing links between rate-dependent crack nucleation and relaxation mechanisms were examined as a function of cartilage integrity (*Chapter 5*). Rate-dependent crack nucleation in intact and GAG-depleted cartilage was induced at multiple loading by a micro-indenter and as a result cracks were generated from pre- to post-relaxation timescales. The degree of PVE relaxation (collagen fibril rearrangement and fluid diffusion) prior to failure governed rate-dependent crack nucleation in intact and GAG-depleted cartilage. Solid matrix degeneration, triggered by GAG depletion, shortened relaxation time and augmented total work required for crack nucleation. The data suggested that GAG depletion improved the capacity of PVE relaxation at given loading rates and resulted in delayed crack nucleation. Total work required for crack nucleation in intact and GAG-depleted cartilage became higher from pre- to post-relaxation timescales. These outcomes designated that cartilage had sufficient time to experience PVE relaxation in a post-relaxation timescale and as a result crack nucleation was delayed. In addition, the dependence between the crack morphology and degree of relaxation underpinned that rate-dependent cartilage failure in intact and GAG-depleted cartilage was governed by PVE relaxation. Critical energy release rate of cartilage was estimated from consistent crack shapes under microindentation, demonstrating the potential of microindentation to serve as a method to measure the critical energy release rate of soft hydrated materials. This work confirmed the links between PVE relaxation and rate-dependent cartilage failure as a function of matrix depletion, consistent with the findings in *Chapter 4*. The links broaden our knowledge of load-induced cartilage damage at different stages of degeneration and provide design parameters for cartilage-like tough materials.

While this dissertation makes several contributions to knowledge about the role of cartilage dissipation mechanisms in the sub-failure and failure regimes, it also opens the door for a new and exciting research directions. The unquestionable difference between cartilage and synthetic materials such as rubber is that cartilage is a living tissue with cellular activities. Load-induced cell death is thought to be one of factors contributing to the initiation and progression of osteoarthritis (OA). Therefore, it would be a logical next step to establish whether cell (chondrocyte) responses are dependent on rate-dependent cartilage failure. Previous studies showed cell death was induced under various loading conditions, including sub-impact loading [3,4] and impact loading [5,6]. In particular, under macroscopic sub-impact loading, a relatively fast strain rate caused cell deactivation combined with matrix failure whereas a relatively slow strain rate only caused cell deactivation [3]. Nevertheless, due to the narrow length- and short time-scales of interest, the links between cellular responses and rate-dependent cartilage failure are not completely established. It is believed that the microindentation-based crack nucleation testing combined with microscopy can contribute to establishing the missing links. A geometrically well-defined micro-indenter will induce localized crack events at known locations. Fluorescent microscopy will provide cell viability as a function of time after crack nucleation. Preliminary data is shown in Figure 6-1. These experimental results are expected to provide possible links between relaxation-dependent crack nucleation and cell injuries, ultimately extending our understanding of the onset and progression of OA.

In addition, it is irrefutable that cartilage failure *in vivo* can be caused by various types of mechanical loading. For example, although cartilage exhibits impressive resistance to fatigue failure, it can break down after numerous cycles of loading [7,8]. Currently, matrix failure and cell death by fatigue loading are only partially understood. These gaps could be filled by applying localized cyclic loading at different frequencies and performing imaging analysis used and proposed here. Understanding underlying mechanisms of fatigue failure in cartilage can answer some pressing clinical and engineering problems (e. g., design parameters for fatigue-resistant soft hydrated material for biomedical applications). Ultimately, it is necessary to link these current and proposed outcomes *in vitro* to cartilage failure *in vivo* to make a groundbreaking contribution in people's lives. To get that stage, the complementary developments of mechanical testing and in-situ imaging techniques appears to be required. In particular, poor resolution of medical imaging (e.g., magnetic resonance imaging, which typically has a voxel size larger than 0.5 mm^3 [9]) is one critical factor currently blocking links between tissue-level mechanics and *in vivo* measurement.

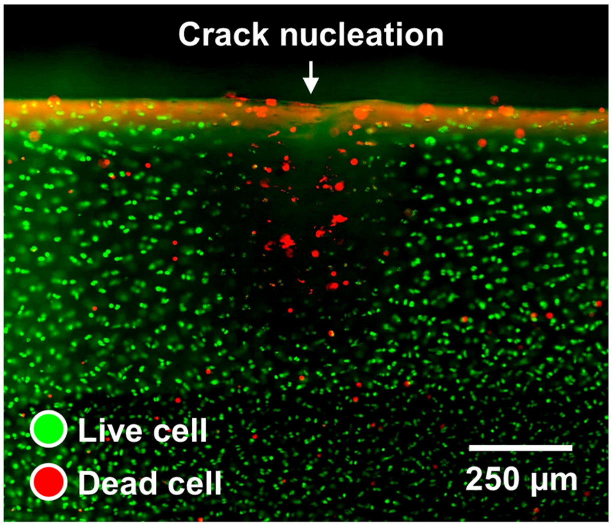

Figure 6-1: Live/dead cell viability image of crack surface induced by microindentation. Crack nucleation was induced at 1 mm/s and then cartilage near the crack was sliced for the cell viability imaging. The imaging of this preliminary data was conducted with an inverted microscope.

In conclusion, this dissertation investigated roles of cartilage dissipation mechanisms in the sub-failure and failure regimes. In the sub-failure regime, uncoupled dissipation mechanisms provide fundamental mechanisms underlying cartilage damping capacity sustained across broad range of frequencies (≥ 5 degree of phase shift). Macroscopic dissipation as a function of cartilage integrity fills the gaps in cartilage damping capacity at *in vivo* contact lengths under traumatic injury and high-rate physiological loading. In the failure regime, the links between rate-dependent crack nucleation and morphological features of crack surfaces provide strong evidence about the physical mechanisms governing rate-dependent cartilage failure. In addition, for the first time, the links between rate-dependent crack nucleation and relaxation mechanisms as a function of cartilage integrity were established. These links advance our knowledge about the initiation of load-induced tissue failure at different phases of degeneration and the underlying mechanisms of impressive cartilage resistance to failure.

6.2. References

[1] Liu, L., Usta, A. D., and Eriten, M., 2017, "A Broadband Damper Design Inspired by Cartilage-like Relaxation Mechanisms," J. Sound Vib., 406(Supplement C), pp. 1–14.

[2] Boz, U., and Eriten, M., 2018, "A Numerical Investigation of Damping in Fuzzy Oscillators with Poroelastic Coating Attached to a Host Structure," J. Sound Vib., 417, pp. 277–293.

[3] Quinn, T. M., Allen, R. G., Schalet, B. J., Perumbuli, P., and Hunziker, E. B., 2001, "Matrix and Cell Injury Due to Sub-Impact Loading of Adult Bovine Articular Cartilage Explants: Effects of Strain Rate and Peak Stress," J. Orthop. Res., 19(2), pp. 242–249.

[4] Bonnevie, E. D., Delco, M. L., Bartell, L. R., Jasty, N., Cohen, I., Fortier, L. A., and Bonassar, L. J., 2018, "Microscale Frictional Strains Determine Chondrocyte Fate in Loaded Cartilage," J. Biomech., 74, pp. 72–78.

[5] Jeffrey, J. E., Gregory, D. W., and Aspden, R. M., 1995, "Matrix Damage and Chondrocyte Viability Following a Single Impact Load on Articular-Cartilage," Arch. Biochem. Biophys., 322(1), pp. 87–96.

[6] Bartell, L. R., Fortier, L. A., Bonassar, L. J., and Cohen, I., 2015, "Measuring Microscale Strain Fields in Articular Cartilage during Rapid Impact Reveals Thresholds for Chondrocyte Death and a Protective Role for the Superficial Layer," J. Biomech., 48(12), pp. 3440–3446.

[7] Vazquez, K. J., Andreae, J. T., and Henak, C. R., 2019, "Cartilage-on-Cartilage Cyclic Loading Induces Mechanical and Structural Damage," J. Mech. Behav. Biomed. Mater., 98, pp. 262–267.

[8] Kaplan, J. T., Neu, C. P., Drissi, H., Emery, N. C., and Pierce, D. M., 2017, "Cyclic Loading of Human Articular Cartilage: The Transition from Compaction to Fatigue," J. Mech. Behav. Biomed. Mater., 65, pp. 734–742.

[9] Zevenbergen, L., Gsell, W., Cai, L., Chan, D. D., Famaey, N., Vander Sloten, J., Himmelreich, U., Neu, C. P., and Jonkers, I., 2018, "Cartilage-on-Cartilage Contact: Effect of Compressive Loading on Tissue Deformations and Structural Integrity of Bovine Articular Cartilage," Osteoarthritis Cartilage, 26(12), pp. 1699–1709.

Appendix A

(Supplementary material for Chapter 4)

A.1 Constitutive models used for cartilage

This section provides the constitutive models, used for a fiber-reinforced poroviscoelastic (PVE) model of cartilage, to clarify the definitions of the material parameters so that they can be universally applicable. All constitutive equations were used as implemented in FEBio version 2.5.2, so additional detail about the models can be found in FEBio Manuals [1].

A.1.1 Neo-Hookean material

A porous-permeable solid matrix of the non-fibrillar matrix was modeled with a Neo-Hookean material [2]. The hyperelastic strain-energy function, W, is expressed by

$$W = \frac{\mu}{2}(I - 3) - \mu \ln J + \frac{\lambda}{2}(\ln J)^2 \tag{A1}$$

where I is the first invariants of the right Cauchy-Green deformation tensor, J is the determinant of the deformation gradient tensor, and μ and λ are the Lamé parameters. μ and λ can be expressed with the more familiar Young's modulus, E, and Poisson's ratio, v ($\mu = \frac{E}{2(1+v)}$ and $\lambda = \frac{vE}{(1+v)(1-2v)}$).

A.1.2 Strain-dependent permeability

The strain-dependent permeability of cartilage was modeled with Holmes-Mow permeability [3], $k(J)$, and given by

$$k(J) = k_0 (\frac{J-\varphi_0}{1-\varphi_0})^{\alpha_{perm}} e^{\frac{1}{2}M(J^2-1)} \tag{A2}$$

where k_0 is the isotropic hydraulic permeability, M is the exponential strain-dependence coefficient, α_{perm} is the power-law exponent, and φ_0 is the solid volume fraction. In this study, k_0, M, α_{perm}, and φ_0 were set as 0.0027 mm^4/Ns [4], 2.2 [4], 2 [4], and 0.2 [4], respectively.

A.1.3 Nonlinear elastic fibers with isotropic distribution

The fibrillar cartilage matrix was modeled as nonlinear elastic with an isotropic distribution via the continuous fiber distribution with the exponential-power law. The fiber strain energy density, $\psi_n(I_n)$, is expressed by

$$\psi_n(I_n) = \frac{\xi}{\alpha_{fibril}\beta} (e^{(\alpha(I_n-1)^{\beta})} - 1) \tag{A3}$$

where I_n is the square of the fiber stretch, $\xi(> 0)$ is a measure of the fiber modulus, $\alpha(\geq 0)$ is the coefficient of exponential argument, and $\beta(\geq 2)$ is the power of exponential argument. When $\lim_{\alpha_{fibril}\to 0} \psi_n(I_n)$, $\psi_n(I_n)$ is simplified by [5]

$$\lim_{\alpha_{fibril}\to 0} \psi_n(I_n) = \frac{\xi}{\beta} (I_n - 1)^{\beta}. \tag{A4}$$

In this work, the simplified form was used. The power of exponential argument was set as β = 2.15 [6], and the fiber modulus was set as ξ = fitting parameter.

The isotropic distribution of the fiber was modeled with the spherical density distribution, $R(\text{n})$, given by

$$R(\mathrm{n}) = \frac{1}{4\pi} \tag{A5}$$

where n is the unit vector along the fiber orientation. Ultimately, the strain energy density of the continuous fiber distribution is defined by integrating the contributions from the fibers oriented along all directions.

A.1.4 Viscoelastic response of fibers

The viscoelastic response of fibers was modeled via the relaxation function with a Prony series, $G(t)$, given by [7]

$$G(t) = 1 + \sum_{i=1}^{N} \gamma_i \exp(\frac{-t}{\tau_i}) \tag{A6}$$

where γ_i is the viscoelastic coefficient and τ_i is the relaxation time. In this work, one relaxation time constant was used to minimize the number of parameters ($N = 1$). The relaxation time of fibrils was set as τ =1.8 seconds [8], and the viscoelastic coefficient was set as γ = fitting parameter.

A.1.5 Comparison with published cartilage constitutive models

In order to compare the entire constitutive model to previously published models, FE models of a $\frac{1}{8}$ symmetry dogbone sample were created. Uniaxial tension was simulated at three loading rates to 0.8% strain: 8×10^{-6} s^{-1} and 8×10^{-2} s^{-1}. Predictions from three additional constitutive models were compared to those from the constitutive model used in this study (described in sections A.1-A.4): biphasic, viscoelastic, and fiber-reinforced PVE models. The biphasic model used strain-dependent permeability (Eq. A2). Permeability constants were pulled directly from a previous publication ($k_0 = 0.0027$ mm^4/Ns, M = 2.2, $\alpha_{perm} = 2$) [4]. The solid matrix was modeled using a hyperelastic neo-Hookean model, with constants obtained by fitting the constitutive model to published to equilibrium stress-stretch data from stress relaxation tests (E = 0.6 MPa, and $\nu = 0.3$) [4]. The viscoelastic model used a neo-Hookean ground matrix and two viscoelastic time constants (Eq. A6); viscoelastic constants were obtained by refitting the published stress relaxation expression to the FEBio expression (E = 0.6 MPa, $\nu = 0.3$, $\gamma_i = 0.49$ and 0.51, and $\tau_i = 915$ s and 4.93 s) [9]. The fiber-reinforced PVE model included strain-dependent permeability (Eq. A2), three viscoelastic time constants (Eq. A6), and exponential fiber behavior by refitting stress-stretch behavior given in the paper to a model available in FEBio (Eq. A4) ($k_0 = 0.0008$ mm^4/Ns, M = 20, $\alpha_{perm} = 2$, E = 0.6 MPa, $\nu = 0.3$, $\gamma_i = 0.6$, 0.7, and 0.2 , $\tau_i = 10$ s, 100 s, and 1000 s, $\xi = 5.2$ MPa, and $\beta = 2$) [10]. The comparison between the models is shown in Figure A-8.

A.2 Supplemental figures

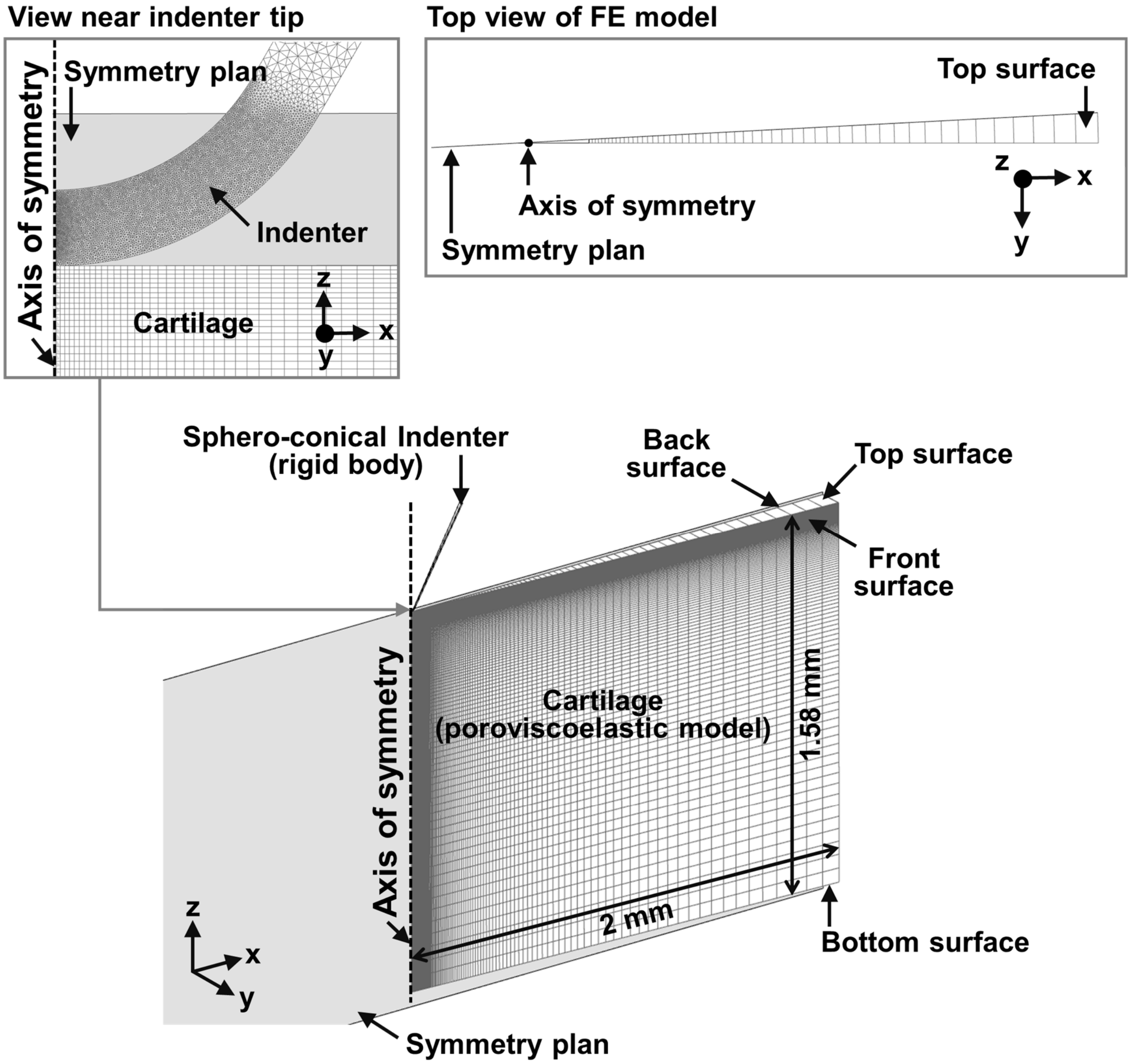

Figure A-1: Whole finite element (FE) model.

Boundary and contact conditions:

1) The axis of symmetry was fixed in the directions of x- and y-axes.
2) The bottom surface was fixed in all directions.
3) The front surface of the cartilage model was fixed in the direction of y-axis.

4) The back surface of the cartilage model and the symmetry plane was set as a tension-compression contact interface (zero displacement in the out-of-plane direction and unconstrained displacement in the in-plane direction).
5) The contact between the indenter and cartilage models was set as frictionless biphasic-on-rigid contact (facet-to-facet contact).

A 3D axisymmetric model was used because the FEBio software does not provide a 2D axisymmetric model. More information can be found in Section 2.9 of PreView User's Manual [11] and in the relevant reference included here [12].

Since the indenter was a rigid body, the mesh size did not affect the FE results (e.g., triangular shell elements: 106,196 elements versus 1,906 elements). The indenter model in Figure A-1 consists of 106,196 elements.

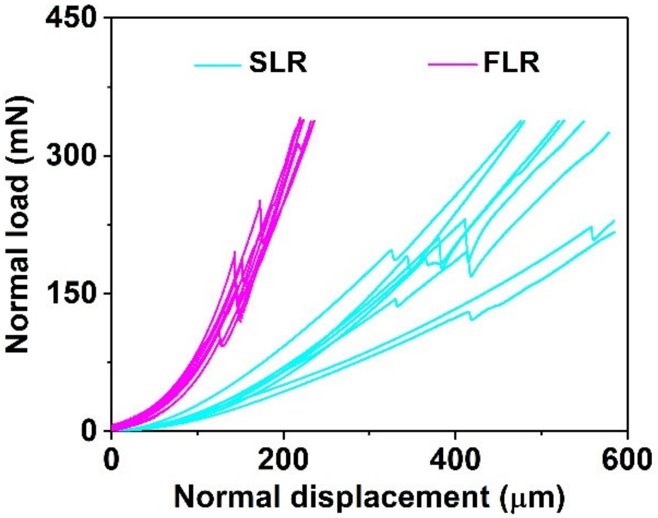

Figure A-2: Results of crack nucleation tests under microindentation.

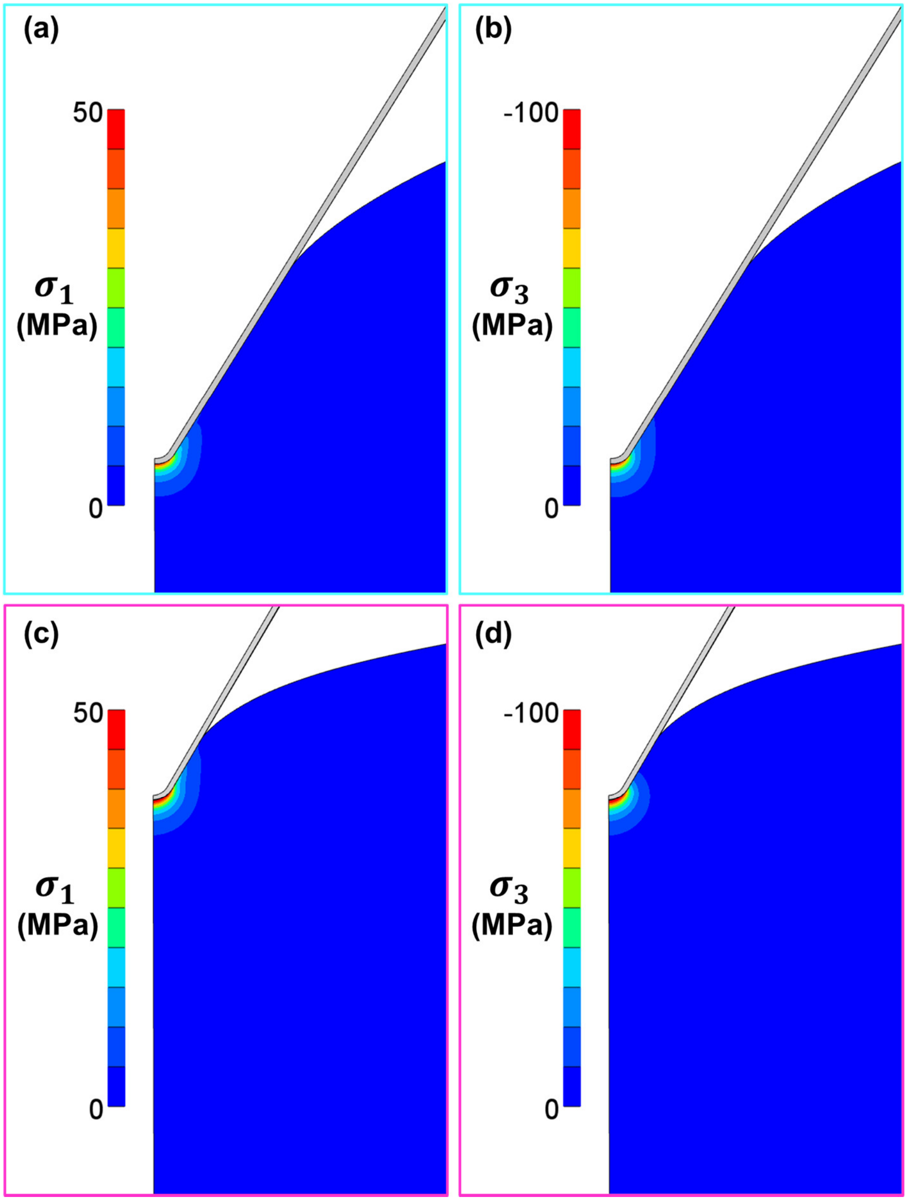

Figure A-3: FE-predicted principal stresses for (a and b) SLR and (c and d) FLR. The range of color scale was matched between the SLR and FLR because they had similar stress values.

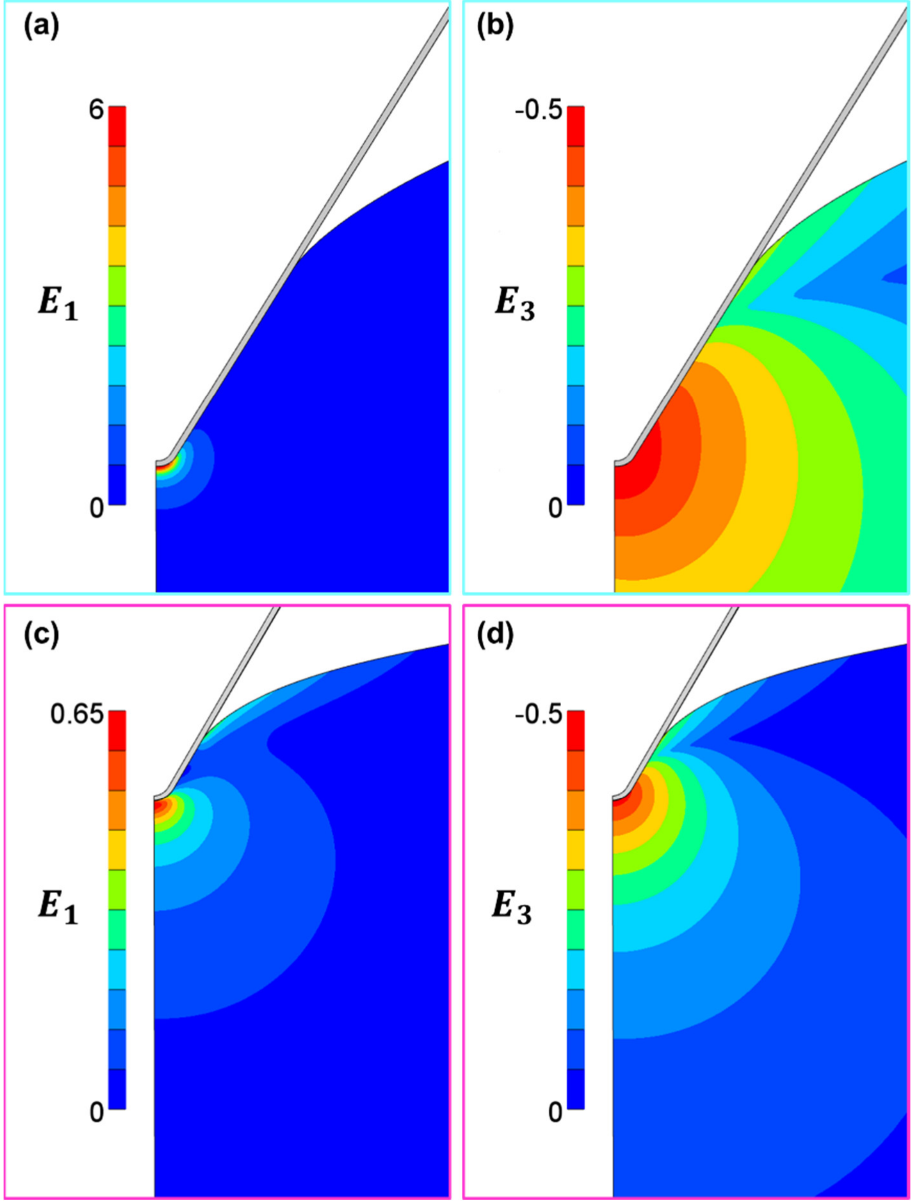

Figure A-4: FE-predicted principal strains for (a and b) SLR and (c and d) FLR. The range of color scale was not matched between the SLR and FLR because they had different values.

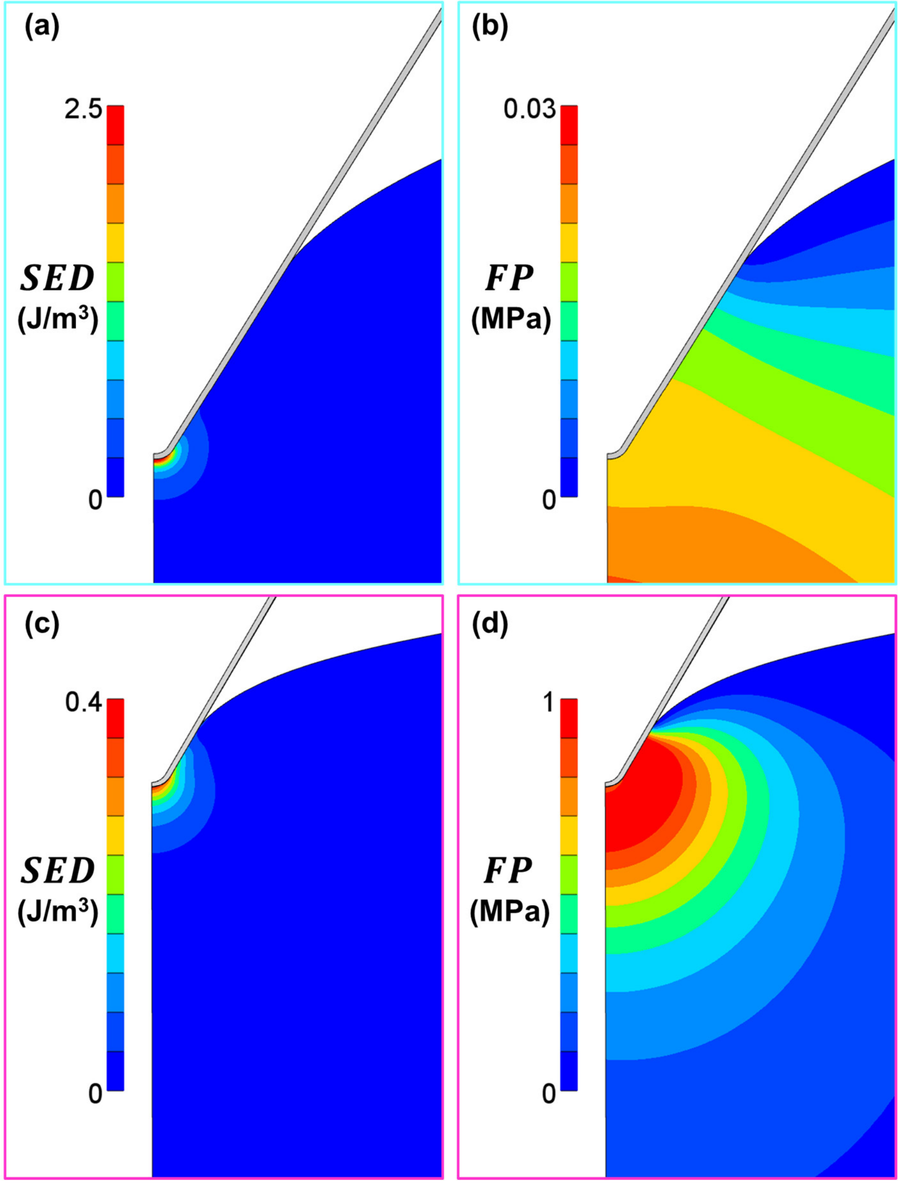

Figure A-5: FE-predicted (a and c) strain energy density, SED, and (b and d) fluid pressure, FP, for (a and b) SLR and (c and d) FLR. The range of color scale was not matched between the SLR and FLR because they had different values.

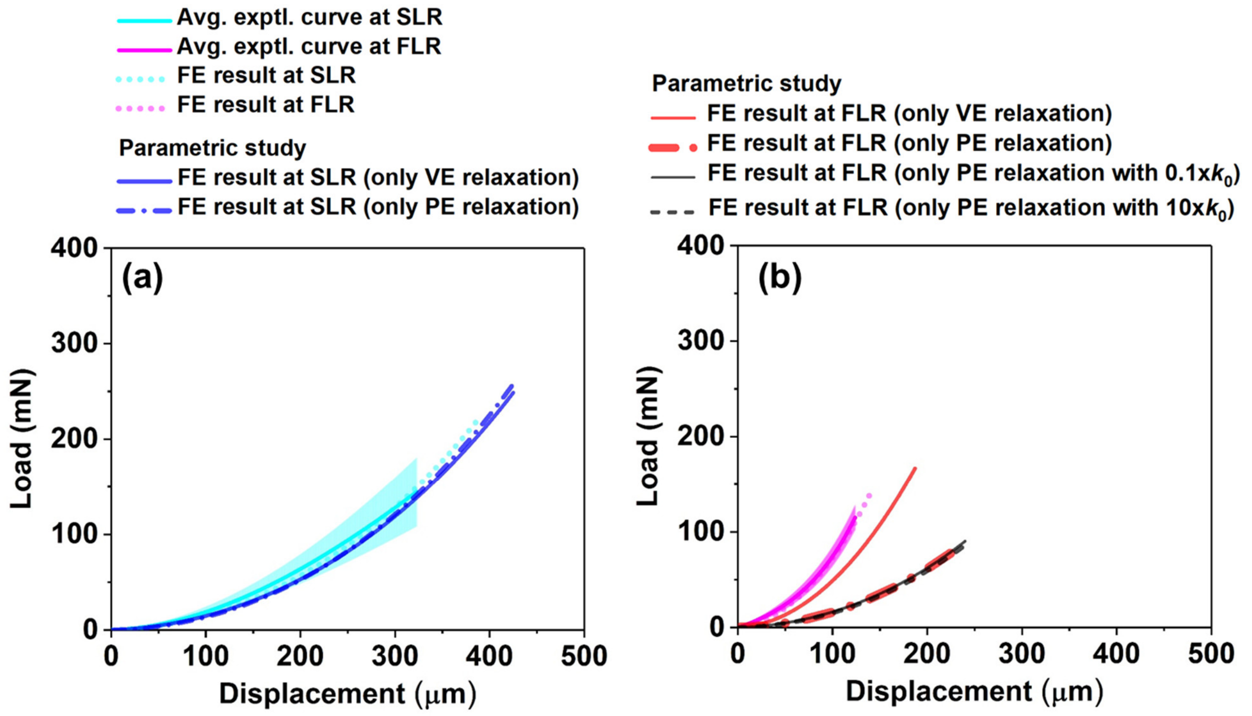

Figure A-6: Results of FE parameter studies on cartilage model: (a) slow load rate (SLR) and (b) fast loading rate (FLR). If specific values (i.e., 0.1×k_0 and 10×k_0 in (b)) are not mentioned in the legend, the material properties in the method section were used. (a) showed that the exclusion of the poroelastic (PE) and viscoelastic (VE) relaxations did not have a pronounced effect on the load-displacement curves at the SLR, indicating the relaxations sufficiently progressed at the SLR. (b) combined with (a) showed that only VE relaxation could reproduce most of the rate-dependent load response, but only PE relaxation could not. In addition, parametric studies with an extensive range of permeability (i.e., 0.1×k_0 and 10×k_0) led to the same conclusion. Thus, the conclusion was not sensitive to the selection of permeability from a previous study [4]. Permeability values for cartilage were usually reported as 10^{-3} - 10^{-4} mm^4/Ns [4,13,14].

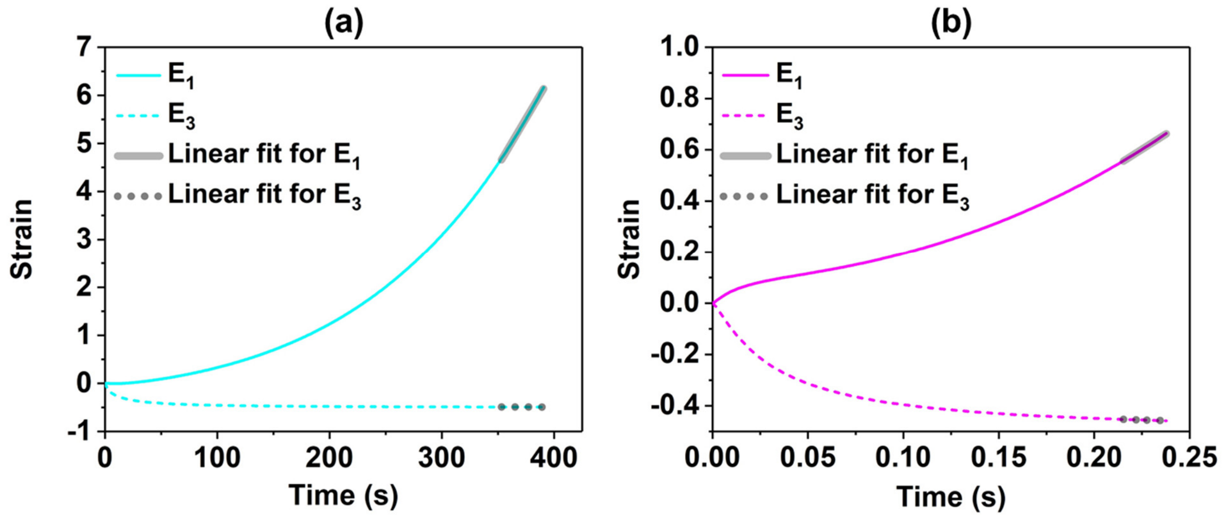

Figure A-7: FE-predicted strain versus time: (a) SLR and (b) FLR. Strain rates just prior to failure were estimated by fitting lines to the 10% ranges of the curves from the end (R^2 > 0.99 for all curves). The FE-predicted strain rates at the SLR were 0.04 s^{-1} for E_1 and -3.54 × 10^{-5} s^{-1} for E_3, and the FE-predicted strain rates at the FLR were 4.74 s^{-1} for E_1 and -0.23 s^{-1} for E_3. Strain rates during physiological activities can be estimated by combining loading frequencies and deformation of cartilage during gait [15–17]. The strain rates can be approximately estimated as 1-10 s^{-1} for walking, 2-50 s^{-1} for jumping, and 4-100 s^{-1} for running. The strain rates at the SLR could correspond to humans resting. The strain rates at the FLR could correspond to the lower bound of the strain rates generated during walking, jumping, and running.

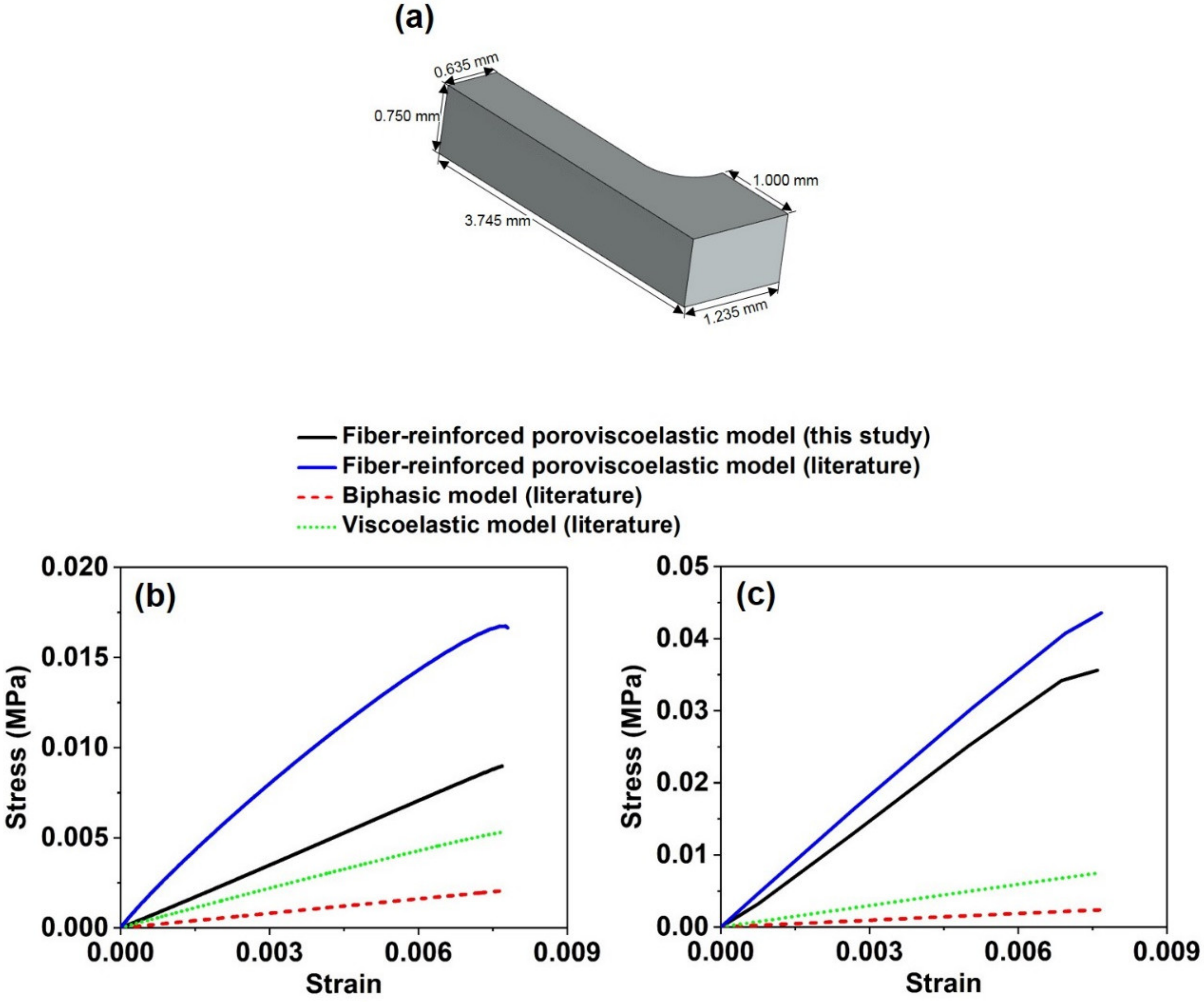

Figure A-8: Predicted Cauchy stress versus Lagrangian strain curves for uniaxial tension comparing cartilage constitutive models: (a) model geometry, (b) slow loading, and (c) fast loading. Predictions from our study were consistent with those from a previous study [10] using a fiber-reinforced PVE model; that study similarly found that only biphasic [4] or only viscoelastic models [9] were insufficient to capture the behavior of interest (e.g., rate-dependent load response). The detailed information on the models is given in Section A.1.5.

A.3 References

[1] Maas, S., Rawlins, D., Weiss, J., and Ateshian, G., "FEBio User's Manual Version 2.8" [Online]. Available: https://help.febio.org/FEBio/FEBio_um_2_8/index.html. [Accessed: 28-May-2019].

[2] Bonet, J., and Wood, R. D., 2008, *Nonlinear Continuum Mechanics for Finite Element Analysis*, Cambridge University Press, Cambridge, UK ; New York.

[3] Holmes, M. H., and Mow, V. C., 1990, "The Nonlinear Characteristics of Soft Gels and Hydrated Connective Tissus in Ultrafiltration," J. Biomech., 23(11), pp. 1145–1156.

[4] Ateshian, G. A., Warden, W. H., Kim, J. J., Grelsamer, R. P., and Mow, V. C., 1997, "Finite Deformation Biphasic Material Properties of Bovine Articular Cartilage from Confined Compression Experiments," J. Biomech., 30(11), pp. 1157–1164.

[5] Ateshian, G. A., Rajan, V., Chahine, N. O., Canal, D. E., and Hung, C. T., 2009, "Modeling the Matrix of Articular Cartilage Using a Continuous Fiber Angular Distribution Predicts Many Observed Phenomena," J. Biomech. Eng., 131(6), p. 061003.

[6] Jones, B., Hung, C. T., and Ateshian, G., 2016, "Biphasic Analysis of Cartilage Stresses in the Patellofemoral Joint," J. Knee Surg., 29(02), pp. 092–098.

[7] Puso, M. A., and Weiss, J. A., 1998, "Finite Element Implementation of Anisotropic Quasi-Linear Viscoelasticity Using a Discrete Spectrum Approximation.," J. Biomech. Eng., 120(1), pp. 62–70.

[8] Yang, L., van der Werf, K. O., Dijkstra, P. J., Feijen, J., and Bennink, M. L., 2012, "Micromechanical Analysis of Native and Cross-Linked Collagen Type I Fibrils Supports the Existence of Microfibrils," J. Mech. Behav. Biomed. Mater., 6, pp. 148–158.

[9] June, R. K., and Fyhrie, D. P., 2009, "Enzymatic Digestion of Articular Cartilage Results in Viscoelasticity Changes That Are Consistent with Polymer Dynamics Mechanisms," Biomed. Eng. OnLine, 8(1), p. 32.

[10] Li, L. P., Korhonen, R. K., Iivarinen, J., Jurvelin, J. S., and Herzog, W., 2008, "Fluid Pressure Driven Fibril Reinforcement in Creep and Relaxation Tests of Articular Cartilage," Med. Eng. Phys., 30(2), pp. 182–189.

[11] Maas, S., Ateshian, G., Weiss, J., and Rawlins, D., "PreView Manual Version 2.1" [Online]. Available: https://help.febio.org/PreView/PreView_2_1/index.html. [Accessed: 25-May-2019].

[12] "Axisymmetric Analysis of Biphasic Indentation" [Online]. Available: http://bio7.mech.columbia.edu/MRLforum/tutorial9.pdf. [Accessed: 28-May-2019].

[13] Athanasiou, K. A., Rosenwasser, M. P., Buckwalter, J. A., Malinin, T. I., and Mow, V. C., 1991, “Interspecies Comparisons of in Situ Intrinsic Mechanical Properties of Distal Femoral Cartilage,” J. Orthop. Res., 9(3), pp. 330–340.

[14] Moore, A. C., DeLucca, J. F., Elliott, D. M., and Burris, D. L., 2016, “Quantifying Cartilage Contact Modulus, Tension Modulus, and Permeability with Hertzian Biphasic Creep,” J. Tribol., 138(4), pp. 041405–041405.

[15] Deneweth, J. M., Newman, K. E., Sylvia, S. M., McLean, S. G., and Arruda, E. M., 2013, “Heterogeneity of Tibial Plateau Cartilage in Response to a Physiological Compressive Strain Rate,” J. Orthop. Res., 31(3), pp. 370–375.

[16] Liu, F., Kozanek, M., Hosseini, A., Van de Velde, S. K., Gill, T. J., Rubash, H. E., and Li, G., 2010, “In Vivo Tibiofemoral Cartilage Deformation during the Stance Phase of Gait,” J. Biomech., 43(4), pp. 658–665.

[17] Nia, H., Bozchalooi, I. S., Li, Y., Han, L., Hung, H.-H., Frank, E., Youcef-Toumi, K., Ortiz, C., and Grodzinsky, A., 2013, “High-Bandwidth AFM-Based Rheology Reveals That Cartilage Is Most Sensitive to High Loading Rates at Early Stages of Impairment,” Biophys. J., 104(7), pp. 1529–1537.

Appendix B

(Supplementary material for Chapter 5)

B.1 Estimation of shear modulus and contact radius

In preparation for calculating critical energy release rate of intact cartilage, shear modulus and contact radius were estimated by using experimental results of intact cartilage at 5 and 0.5 mm·s^{-1} and an axisymmetric finite element (FE) model of the indenter-cartilage system. Since cartilage was in a pre-relaxation timescale at 5 and 0.5 mm·s^{-1}, shear modulus and contact radius were estimated by considering cartilage as a nearly-incompressible, nonlinear elastic solid. All of the modeling and simulation were performed in Abaqus 2016 (Dassault Systemes SIMULIA, RI, USA).

The sphero-conical indenter model had dimensions identical to the experimental setup (tip radius: 100 µm and half-angle of cone: 45º). The dimensions of the cartilage model were 3 mm in radius and 1.6 mm in thickness; as the intact cartilage tested experimentally had 3 mm radius and 1.56 ± 0.11 mm average thickness. The bottom surface of the cartilage model was fixed in all directions. Contact between the indenter and cartilage models was set as frictionless. Surface to surface interaction was prescribed at the interface, and the penalty method was used to enforce the contact constraints. The indenter and cartilage models were considered as the master and salves surfaces, respectively. The cartilage model was discretized through biased meshing resulting in finer meshes toward the contact area (Figure B-1). Four quarter circles with radii of 0.25 mm, 0.5 mm, 0.75 mm and 1 mm were generated, and the minimum and maximum mesh sizes of 0.001 and 0.005 mm were assigned to the smallest and largest quarter circles, respectively. The mesh size outside the largest quarter circle was set to be 0.03 mm. The model was composed of linear quadrilateral (CAX4R- 21940 elements) and triangular (CAX3- 356 elements) elements. The number of elements was determined through mesh convergence analysis.

The indenter and cartilage were modeled as a rigid body and a hyperelastic Ogden material, respectively. The strain energy density of the Ogden material model is expressed by

$$U = \sum_{i=1}^{N} \frac{2\mu_i}{{\alpha_i}^2} ({\lambda_1}^{\alpha_i} + {\lambda_2}^{\alpha_i} + {\lambda_3}^{\alpha_i} - 3) \tag{B1}$$

where μ_i are the shear moduli, $\lambda_{1,2,\ and\ 3}$ are the deviatoric principal stretches, and α_i is the power law constant ($N = 1$ in this simulation). The power law constant was set as $\alpha_1 = 3$, and the shear modulus was set as μ_1 = fitting parameter. In addition, the small-strain bulk modulus, K, was given by

$$K = \frac{2\mu_1(1+v)}{3(1-2v)} \tag{B2}$$

where v is Poisson's ratio. The cartilage model was set as a nearly incompressible material by selecting $v = 0.478$. μ_1 was determined by fitting predicted load-displacement curves to average experimental load-displacement curves of intact cartilage at 5 and 0.5 mm·s^{-1} ($R^2 \geq 0.96$) (Figure B-2). Finally, Shear moduli, μ_1, of 11.52 MPa and 9.00 MPa were obtained for the curves at 5 and 0.5 mm·s^{-1}, respectively. In addition, contact radius as a function of displacement was acquired to determine the contact radii corresponding to critical displacements, R_c (Figure B-3). R_c was obtained by fitting a linear function to the FE-predicted curve ($R^2 > 0.99$) and recording predicted contact radii corresponding to experimental critical displacements.

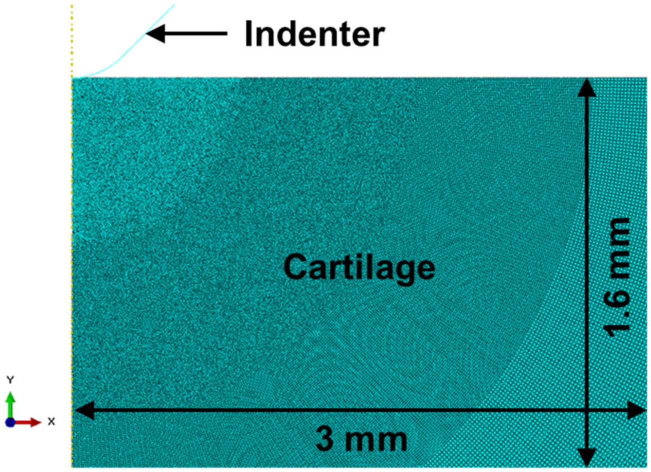

Figure B-1: FE model of indenter-cartilage system. The mesh size became finer toward the contact area between the indenter and cartilage models.

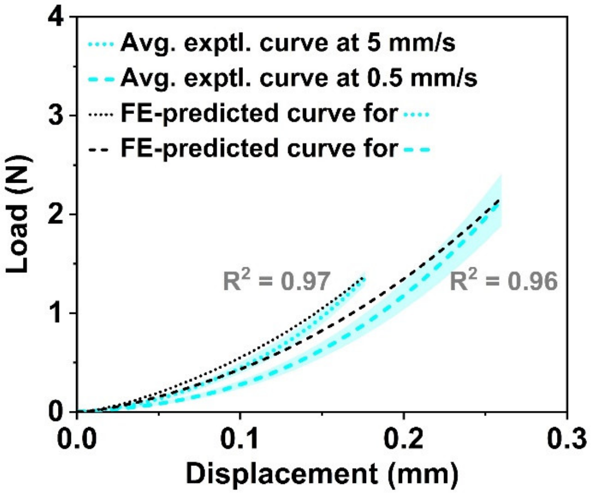

Figure B-2: Comparison between experimental and FE-predicted load-displacement curves. The average experimental curves were obtained from crack nucleation tests on intact cartilage at 5 and 0.5 mm·s^{-1} and were presented in Figure 5-2a.

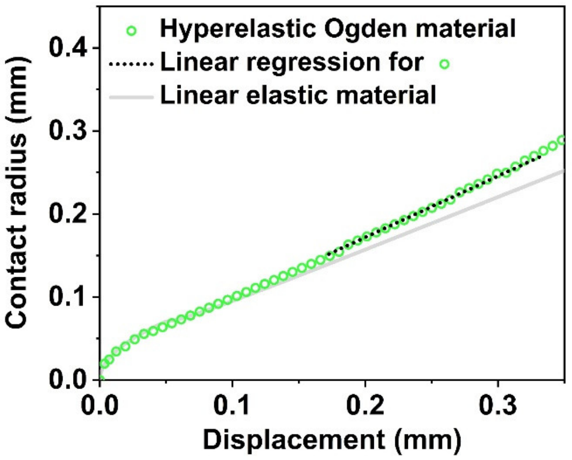

Figure B-3: Contact radius as function of displacement. The contact radius estimated from the Ogden material was slightly larger than that previously estimated from a linear elastic material [1]. A linear function was fitted to the FE-predicted curve in a range from minimum to maximum critical displacements (5 - 0.5 mm·s^{-1}) ($R^2 > 0.99$). The linear function was used to determine predicted contact radii corresponding to experimental critical displacements, $\boldsymbol{R_c}$.

B.2 Determination of critical energy release rate of intact cartilage

The consistent line-shaped cracks in intact cartilage, generated within a pre-relaxation timescale (5 and 0.5 mm·s^{-1}), allowed the determination of critical energy release rate by using a penetration model for a sharp punch proposed by Shergold and Fleck [2,3]. In this model, a rigid conical tip with a cylindrical shaft of radius, R, was indented into a semi-infinite solid. This solid was considered as an incompressible, hyperelastic, and isotropic material and described with the Ogden material model. Contact between the tip and solid was considered to be frictionless. The steady-state penetration of the tip by an axial increment, δl, was caused due to a load, P_s, while generating a plane strain crack with a length of $2a$ and a thickness of δl, and then opening the crack to accommodate the tip. The energy balance approach was used by equating the work done by the penetrating indenter tip, $P_s\delta l$, to the sum of the energy required to form a crack, δW_C, and the strain energy increase δS_E for crack surface to accommodate the penetrating indenter as follows:

$$P_s\delta l = \delta W_C + \delta S_E. \tag{B3}$$

When a crack with a length of $2a$ penetrates to a depth of δl, $\delta W_C = 2J_{IC}a\delta l$ for the critical energy release rate of the material in mode I fracture, J_{IC}. The strain energy δS_E was estimated via FE modeling and expressed in terms of a dimensionless function, $h(\frac{a}{R})$, for convenient FE analysis later. Then, Eq. B3 is given by

$$P_s\delta l = 2J_{IC}a\delta l + \mu R^2 h(\tfrac{a}{R})\delta l. \tag{B4}$$

The average penetration pressure, p_s, on the punch is obtained by dividing P_s by the projected contact area ($=\pi R^2$). As a result, Eq. B4 is expressed by

$$\frac{p_s}{\mu} = \frac{P_s}{\pi\mu R^2} = \frac{2}{\pi}\left(\frac{J_{IC}}{\mu R}\right)\left(\frac{a}{R}\right) + \frac{1}{\pi}h(\tfrac{a}{R}). \tag{B5}$$

When $\frac{p_s}{\mu}$ is plotted as a function of $\frac{a}{R}$ (Eq. B5), stable penetration occurs at the minimum value of $\frac{p_s}{\mu}$ ($=\frac{p_{s-min}}{\mu}$). Then, Shergold and Fleck [3] predicted the relation between $\frac{p_{s-min}}{\mu}$, $\frac{a}{R}$, $\frac{J_{IC}}{\mu R}$ and α through FE analysis. The relation between $\frac{a}{R}$ and $\frac{p_{s-min}}{\mu}$ for $\alpha = 3$ [3] is replotted in Figure B-4 to determine critical energy release rate of intact cartilage. In our study, R is equal to R_c which was obtained in Section B.1 using the identical material model.

Critical energy release rate of intact cartilage was determined using experimental and FE-predicted results. Experimentally-measured values of critical load and crack lengths for intact cartilage at 5 and 0.5 mm·s^{-1} provided the values of P_{s-min} and a, respectively; p_{s-min} is equal to $\frac{P_{s-min}}{\pi R_c^2}$. R and μ were estimated from the FE-predicted contact radius at critical displacements, R_c, and shear modulus, 11.52 MPa for 5 mm·s^{-1} and 9.00 MPa for 0.5 mm·s^{-1} (Section B.1), respectively. Consequently, the determined $\frac{a}{R_c}$ and $\frac{p_{s-min}}{\mu}$ formed clusters close to the backbone curve for the relaxation between $\frac{a}{R}$ and $\frac{p_{s-min}}{\mu}$ [3] (Figure B-4). The corresponding values of $\frac{J_{IC}}{\mu R}$ to $\frac{a}{R_c}$ were 0.74±0.28 for 5 mm·s^{-1} and 0.73±0.22 for 0.5 mm·s^{-1} [3]. Then, as μ and $R(= R_c)$ were already obtained, critical energy release rate of intact cartilage ($= J_{IC}$) could be determined as 1.51 ± 0.63 to 1.60 ± 0.55 kJ/m^2 (5 to 0.5 mm·s^{-1}).

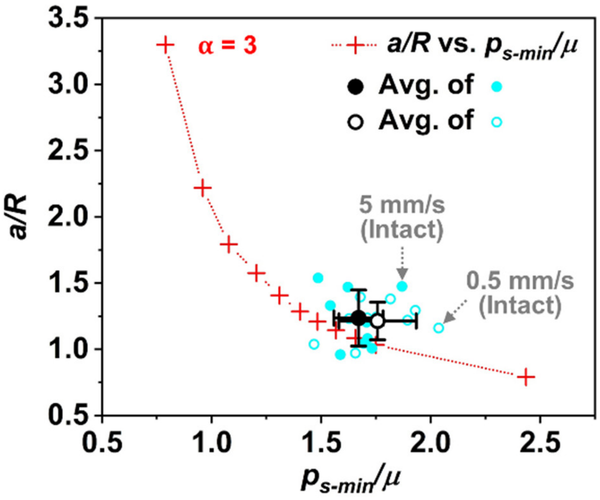

Figure B-4: Backbone curve for relation between $\frac{a}{R}$ and $\frac{p_{s-min}}{\mu}$ and projected data points. The backbone curve was taken from [3]. The projected data points were determined using the experimental and simulated results.

Note that, we refer to the first detectable load drop-off as the “major crack nucleation” event in the manuscript. However, the aforementioned analysis and critical energy release rate are valid for stable crack propagation into the cartilage. This is applicable to our tests where a sharp-tip indenter pierced into the tissue at a particular location. Minor crack nucleation during early stages of penetration could not be detected in those tests due to noise floor in load cell. Besides, the length of those minor cracks is expected to be on the order of crack-tip size (<100 um) thanks to rigid kinematic constraint indenter tip imposes. Therefore, identifying those minor cracks from optical images is also quite challenging. As can be seen in Figure 5-5, all the detectable cracks have lengths greater than 400 um, which suggests propagation of those minor cracks into larger detectable ones, and subsequent increase in measured indentation forces hints at stable crack growth. Experimental techniques with higher force and displacement resolutions are needed to distinguish the minor crack nucleation events from actual crack propagation referred to as “major crack nucleation” here.

B.3 References

[1] Briscoe, B. J., Sebastian, K. S., and Adams, M. J., 1994, “The Effect of Indenter Geometry on the Elastic Response to Indentation,” J. Phys. Appl. Phys., 27(6), p. 1156.

[2] Shergold, O. A., and Fleck, N. A., 2005, “Experimental Investigation Into the Deep Penetration of Soft Solids by Sharp and Blunt Punches, With Application to the Piercing of Skin,” J. Biomech. Eng., 127(5), pp. 838–848.

[3] Shergold, O. A., and Fleck, N. A., 2004, “Mechanisms of Deep Penetration of Soft Solids, with Application to the Injection and Wounding of Skin,” Proc. R. Soc. Lond. Ser. Math. Phys. Eng. Sci., 460(2050), pp. 3037–3058.